Hadronic Energy Distributions in Deep-Inelastic Electron-Proton Scattering

Michael Byrne Crombie

A thesis submitted in conformity with the requirements
for the Degree of Doctor of Philosophy in the
University of Toronto

Department of Physics
University of Toronto

Hadronic Energy Distributions in Deep-Inelastic Electron-Proton Scattering

Michael Byrne Crombie

Doctor of Philosophy

Department of Physics

University of Toronto

1994

Abstract

An outline of QCD, the theory of strong interactions, is given and several QCD Monte Carlo models are described in detail. Energy distributions of the hadronic system produced in neutral current electron-proton deep-inelastic scattering at a centre of mass energy of 296 GeV are presented. Comparisons of the results with the models show that QCD radiation has a strong influence on the characteristics of the hadronic final state. The data is reasonably well produced by the Lund model based on a matrix element calculation in first order of the strong coupling, followed by appropriate parton showers. The colour dipole model also gives a reasonable representation of the data. Neither the first order matrix elements alone nor the Lund parton shower model, without the matrix element calculation, reproduce the data. The HERWIG parton shower model is also deficient.

The data was taken with the ZEUS detector at the HERA accelerator in Hamburg, Germany. A general description of the detector design and principles of operation is provided. A three level trigger system is required to handle the high luminosity delivered by HERA. The first two levels involve the local processing of component data. The third level makes a decision based on the global information from an event. It accepts events at 100 Hz, or 20 MBytes/sec, at the design luminosity and reduces this to around 5 Hz. The architecture and implementation of the third level trigger system is discussed.

Acknowledgements

Without a doubt, the first person I would like to thank is my supervisor, Robert S. Orr at the University of Toronto. He offered me a wonderful opportunity and provided constant enthusiasm, acumen, and humour. I also would like to thank John F. Martin of the University of Toronto who presented the Canadian students in Hamburg with a fine example of fair leadership and dedication to one's profession.

In an experiment as large as ZEUS, one inevitably encounters a large and diverse group of individuals in the course of work on the detector and analysis. I am particularly indebted to the members of the third level trigger group: Bob, David, Dinu, Sampa, Gerd, Frank, Frédéric, Cortney, and Richard. I would also like to thank all of the people who appear on the ZEUS author list in the appendix to this thesis, especially Chris Youngman and Wolfgang Vogel with whom I worked quite closely. A special thanks is due to my fellow students: Frédéric Bénaud, Burkhard Burow, Frank Chlebana, and John Mayer.

I owe considerable thanks to both Nick Brook and Malcolm Derrick for their support and guidance on physics matters. I am also beholden to Gunnar Ingelman for explaining many aspects of the models studied in this thesis.

I should also express my appreciation to the Canadian taxpayers, who, under the auspices of the Natural Sciences and Engineering Research Council and the University of Toronto, provided financial support.

I am very grateful to my parents and family, without whose constant support and encouragement I should not have completed or even attempted this undertaking. I really appreciate it.

Dedico questa tesi a mia moglie, Daniela, per tutto cio'che mi ha dato.

Contributions to the ZEUS Experiment

I have been an active member of the ZEUS collaboration since September of 1988 and was resident at DESY from May of 1989 to June of 1993. Throughout this period I have been involved in every phase of the third level trigger system from the first hardware architecture studies to the writing and verification of trigger algorithms. This work began with design feasibility studies. I wrote a Monte Carlo program that simulated the bandwidth of different system architectures and did extensive testing of all proposed system hardware to ensure that it met specifications. In cases where it did not, it was necessary to find alternative solutions. This involved evaluating hardware, performing our own modifications, and working with manufacturers to fix problems or enhance product performance. I was also involved in the design of the system control software and wrote the event builder and central VAX link data transfer software. I installed the prototype and final trigger systems at DESY and debugged both the hardware and control software. I was fully responsible for the hardware during my four year stay at DESY and presented status reports on the third level trigger at collaboration trigger meetings. This work is detailed in Chapter 4.

I also wrote the third level trigger calorimeter analysis software. During the first two runs in the summer and fall of 1992, I was responsible for coding and checking two trigger algorithms that were used to reject events. These are described in the latter part of Chapter 3. In addition, I performed online expert shifts for the experiment during the first cosmic ray runs and electron-proton running. This position required having a general knowledge of the entire data acquisition and trigger system of the experiment. These duties entailed being on call 24 hours a day for most of 1992.

My first physics analysis was for the Physics at HERA workshop in 1991. I was one of two authors of a study on the feasibility of measuring the strong coupling at HERA using jet ratios. This was published by DESY in volume one of the workshop proceedings. The physics analysis presented in Chapters 5 and 6 of this thesis was performed on the ZEUS data that was collected in 1992. It constitutes the first ZEUS study of the hadronic final state and the first comprehensive comparison of data and Monte Carlo models in the low x region accessible at HERA. The analysis has been published in Zeitschrift für Physik C59 (1993) 231.

Contents

List of Figures

Chapter 1

Introduction

The fundamental undertaking of particle physics is to explore deeper and deeper into matter in an attempt to uncover its constituents and the laws governing their behaviour. For those not in the field, it may seem that some experiments go about this task in a rather oblique manner. The approach taken by the experiments at the HERA electron-proton collider, however, is quite direct: a beam of electrons is collided with a beam of protons. The electrons can scatter off of the constituents of the proton just as alpha particles collided with the nuclei of gold atoms in Rutherford's classic experiment. The HERA beam energies result in a center-of-mass energy that is an order of magnitude higher than has been available from fixed-target lepton-proton collision experiments.

The properties of the final state hadronic system are determined by the theory of the strong interactions, quantum chromodynamics (QCD). In this thesis, energy distributions of the hadronic final state obtained by the ZEUS detector are presented and discussed. They are also compared with the predictions of several QCD Monte Carlo models. Monte Carlo models that simulate the basic underlying partonic processes have become essential tools in interpreting multi-body final states resulting from high energy interactions.

The models studied differ primarily in their treatment of QCD coherence effects. Although coherence is a well established property of all quantum mechanical systems, coherent phenomena have their origins in the basic structure of the theory. It is both remarkable and fortunate that quantum mechanical interference effects among partons are discernible after the hadronization of partons to hadrons.

The general outline of this thesis is as follows. Chapter 2 provides a short description of the current picture particle physics has drawn of matter. The focus is on the strong interaction and how an understanding of it was elucidated by electron-proton physics. This theory provides the basis for the models used to simulate electron-proton collisions.

Chapter 3 describes the experimental setup used to perform the measurements. Novel features of the ZEUS detector and the components relevant to the analysis presented in this thesis are emphasized. However, a brief description of the entire detector and accelerator complex is given.

A detailed treatment of the ZEUS third level trigger system hardware architecture is given in Chapter 4, as this was the author's principal contribution to the experimental apparatus. The evolution of the system design is discussed as well as the system performance to date.

Chapter 5 orients the reader to the kinematics of electron-proton scattering at HERA and explains the event selection criteria. Measured distributions of the kinematical variables are shown and remarked upon.

In Chapter 6, distributions showing the general shape of events in the ZEUS detector are provided. Energy distributions of the final state hadronic system are presented as a function of some of the kinematical variables and are compared with the predictions of several Monte Carlo models. The chapter concludes with a general summary of the results and a discussion of the models.

Chapter 2

The Strong Interaction

2.1 The Standard Model of Particle Physics

Experimental particle physics is concerned with the most elementary constituents of matter. This entails searching for, and studying, the properties of these particles as well as the nature of their interactions. The present knowledge is embodied within the theoretical structure of the Standard Model [1], [2].

This model is based upon a class of quantum field theories known as gauge theories. Particles are described by matter fields, $\Psi(x_\mu)$, for which a free particle Lagrangian density can be given. The symbol $\Psi(x_\mu)$ is a column vector denoting an array of different fields, which are functions of the space-time vector, x_μ. By definition, a gauge field theory Lagrangian is invariant under local gauge transformations of the form

$$\Psi(x) \rightarrow \Psi'(x) = U(x)\Psi(x), \tag{2.1}$$

where $U(x)$ is a matrix whose elements are also a function of x_μ. The matrices, U, form a representation of a symmetry group of transformations.

The ramifications of invariance under the symmetry operation (2.1) are profound: interacting gauge fields that compensate for the local changes in the matter fields must be introduced to the free particle Lagrangian. The gauge fields correspond to bosons since they are required to transform as vectors. Therefore, given the symmetry group, gauge invariance yields the structure of the particle interactions. The symmetry is deduced from observation.

The strength of an interaction is characterized by a coupling which is directly proportional to the square of the emission or absorption amplitude of the appropriate boson. In quantum field theory, an amplitude for an interaction is represented by a power series in this coupling. Of vital importance for any such theory is that finite amplitudes can be calculated to any order in the coupling. If a theory possesses this property and it has a finite number of parameters, then it is said to be *renormalizable*. Some early field theories of particle interactions were nonrenormalizable. The pertinency of gauge theories was strengthened by the proof that all such theories are

Interaction	Coupling Symbol	Relative Strength
strong	α_s	1
electromagnetic	α	10^{-2}
weak	α_W	10^{-6}
gravitational		10^{-39}

Table 2.1: Relative strengths of interactions at a distance of about 10^{-18} cm.

renormalizable [3].

There are two classes of elementary particles: quarks and leptons. By the exchange of gauge bosons, they may interact through the electromagnetic, the weak, and the strong interactions. The relative strengths of the interactions at a distance of about 10^{-18} cm are shown in Table 2.1 All massive particles interact gravitationally, but gravity is neglected henceforth as it has no measurable effects on a subatomic scale. In Table 2.2 the quarks and leptons are listed. There are six different *flavours* of both leptons and quarks. These are classified into three generations as delineated by the columns in the table. With the exception of the neutrinos, which have small, if not zero, rest masses, the masses increase from left to right. For each particle in Table 2.2, there is a corresponding antiparticle. The properties of an antiparticle are obtained by reversing the sign of the additive internal quantum numbers, i.e those that are not connected to space-time, of the corresponding particle. Antiparticles are denoted by a bar, e.g. $\overline{q}$.

The electromagnetic interaction is mediated by photons which are required to be massless by gauge invariance. The Lagrangian is invariant under phase transformations, i.e. transformations of the form $e^{iq\alpha(x)}$, where q is the parameter that characterizes the amplitude for the emission or absorption of a photon. Its value is the electric charge of the particle under consideration. Each particle generation has a lepton of electric charge -1, a quark of charge +2/3, and a quark of charge -1/3. The neutrinos have no electric charge. Throughout, the absolute value of the electron charge, e, defines the unit charge.

Phase transformations generate the Abelian group of 1 x 1 unitary matrices denoted by $U(1)$. The interacting field theory that is invariant under $U(1)$ is called quantum electrodynamics or QED. The exchanged photons are virtual because emission by a charged particle requires that the photon obtain a nonzero mass in order to conserve energy. Virtual photons can exist only for a time interval given by the Heisenberg Uncertainty Principle. They will be indicated by the symbol γ^*. There are two consequences of the Abelian nature of the group $U(1)$; the photons do not

Quarks		
u (up)	c (charm)	t (top)
d (down)	s (strange)	b (bottom)
Leptons		
e (electron)	μ (muon)	τ (tau)
ν_e (e-neutrino)	ν_μ (μ-neutrino)	ν_τ (τ-neutrino)

Table 2.2: Standard Model quarks and leptons. There is no direct evidence for the t quark, the heaviest of the quarks.

interact with each other and the electromagnetic coupling decreases as the distance between two electrically charged particles increases.

All particles interact through the weak interaction. There are three massive weak bosons: the W^+, W^-, and Z^0, where the superscripts denote the electric charge. The W mass is about 80 GeV and the Z mass is about 90 GeV. Emission of a charged weak boson results in a flavour changing transition, e.g. $u \rightarrow dW^+$.

The electromagnetic and weak interactions are unified under a single theory of electroweak interactions. In the framework of the Standard Model, both have the same intrinsic coupling so that the amplitudes for the emission and absorption of the weak bosons and photons are approximately the same. However, the probability to *exchange* a weak boson is suppressed since they are massive. At momentum transfers much greater than the masses of the weak bosons, the two interactions are predicted to be of similar strength. The electroweak Lagrangian is invariant under *SU(2)* x *U(1)*, where *SU(2)* is the subgroup of unitary 2 x 2 matrices with unit determinant.

The strong interactions occur between hadrons, which are composite particles made up of quarks. The notion of a quark was originally introduced in 1964 to explain the symmetries in the classification of the known hadrons according to their masses and quantum numbers [4]. This Quark Model was not a field theory and provided no explanation of quark interactions. Quantum numbers were assigned to the quarks and a new quantum number with three possible values, now called colours, was hypothesized [5]. Colour was originally intended to avoid violating Fermi statistics in the case of hadrons that were supposed to have three identical quarks in the same state. It also could explain a missing factor of three in the total hadronic e^+e^- cross-section since the total cross-section should then be proportional to the number of colours. Nevertheless, the fact was that no quark had ever been observed and, thus, they were considered to be mathematical devices.

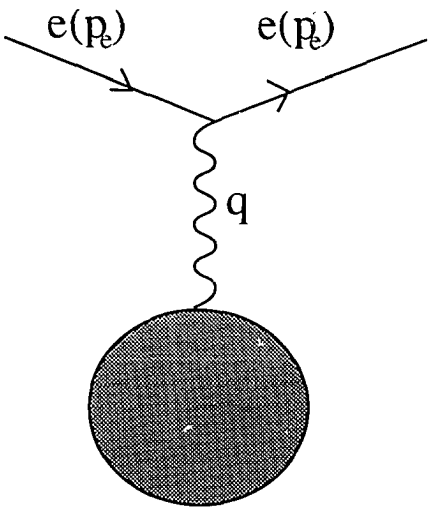

Figure 2.1: Electron scattering off a charge distribution.

In the early 1960's all attempts to construct field theories of the strong interactions had failed [6]. The reason was that the elementary fields were taken to be hadron fields, namely, the pion and the nucleon This approach was problematic because the proliferation in the number of observed hadrons made it clear that the pion and nucleons could not be elementary particles. Moreover, the coupling in this theory was too large to permit the application of perturbation theory. If hadrons were composed of more elementary particles, the way to investigate their dynamics was to probe them with point-like leptons.

2.2 Electrons as Probes: Elastic Scattering and Form Factors

Leptons are effective for studying hadron structure because they are structureless at present distance scales and they do not interact strongly. The kinematics of electron scattering off a general charge distribution is shown in Figure 2.1. The four-momentum transfer is denoted by $q = p_e - p_e'$, where $p_e = (E, \vec{p}_e)$ is the electron four-momentum. Since four-momentum is conserved at the electron-boson vertex, q^2 is spacelike, i.e. $q^2 < 0$. The positive definite variable, Q, defined by $Q^2 \equiv -q^2$ generally is introduced. For Q^2 much less than the masses of the weak bosons, the electron will interact electromagnetically with the charge almost exclusively through the exchange of a virtual photon.

Consider first elastic scattering of a relativistic electron off a point-like particle of charge e_i. If the target is static and spinless, the cross-section is given by the Mott formula:

$$\left(\frac{d\sigma}{d\Omega}\right)_{Mott} = \frac{4\alpha^2 e_i^2 E^2}{Q^4}\cos^2\frac{\theta}{2}. \tag{2.2}$$

There is only one independent variable for elastic scattering, e.g. the angle of the scattered electron, θ, or Q^2. If the charge distribution is diffuse, the ratio of the angular distribution of scattered electrons to $(d\sigma/d\Omega)_{Mott}$ gives a form factor, $F(q)$:

$$\frac{d\sigma}{d\Omega} = \left(\frac{d\sigma}{d\Omega}\right)_{Mott} |F(q)|^2. \tag{2.3}$$

The form factor can be shown to be the Fourier transform of the charge distribution, ρ [2]. Therefore, it can give a measure of the target dimensions, viz.,

$$\begin{aligned} F(q) &= \int d^3r\rho(r)\exp(i\vec{q}\cdot\vec{r}) \\ &= \int d^3r\rho(r)\left[1 + i\vec{q}\cdot\vec{r} - \frac{(\vec{q}\cdot\vec{r})^2}{2}\ldots\right] \\ &= 1 - \frac{1}{6}|q|^2 < r^2 > \quad + \ldots, \end{aligned}$$

if $|\vec{q}|$ is not too large. If the target also has spin, a second form factor is needed as the magnetic moment may not be a point moment.

In 1956, cross-section measurements from fixed target electron-proton scattering experiments performed with 188 MeV electrons showed that the proton was not a point particle and had a root mean square charge radius of about 0.74 x 10^{-13} cm [7]. At these low electron energies, the de Broglie wavelength of the exchanged photons, given by $\lambda = 1/Q$, is also on the order of 10^{-13} cm. Therefore, if there was further structure, it could not be discerned.

2.2.1 Inelastic Scattering and Structure Functions

In fixed-target elastic electron-proton scattering with negligible proton recoil energy, the electron loses no energy to the proton and the final state always consists of an electron and a proton. As the incident electron energy is increased to about 1 GeV, inelastic scattering is observed [9]. The hadronic final state no longer consists of the proton but is multi-particle and has an invariant mass, W, greater than the mass of the proton, m_p. This is shown in Figure 2.2, in which the double differential cross-section is plotted as a function of W. The peaks correspond to

pion-proton resonances. The Q^2 value is still fairly low, around 1 GeV^2, so that structural features of the resonances cannot be studied.

A second variable is required to describe the kinematics of inelastic scattering. The variable ν, defined by

$$\nu \equiv \frac{P \cdot q}{m_p}, \tag{2.4}$$

where P is the four-momentum of the proton, is convenient for fixed target experiments as it is the energy lost by the electron in the rest frame of the target proton. Alternatively, a dimensionless variable, y, given by

$$y = \frac{P \cdot q}{P \cdot p_e} \tag{2.5}$$

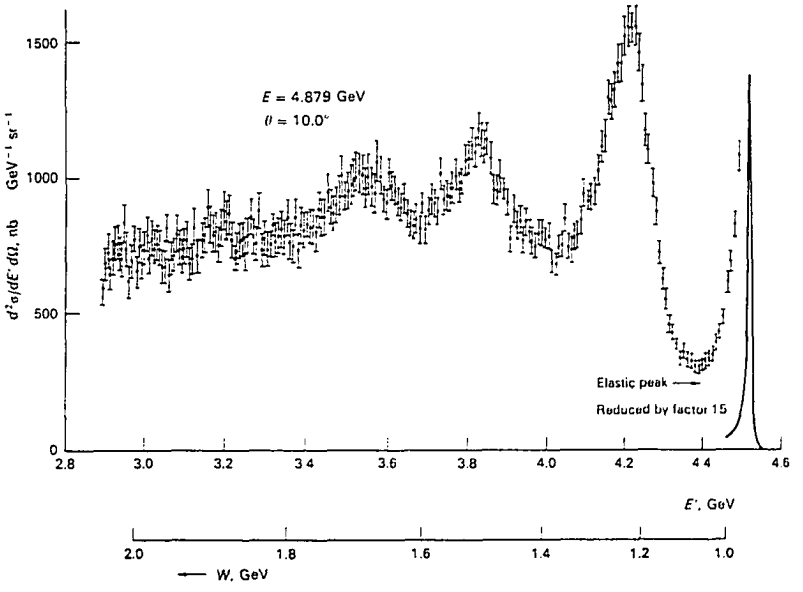

Figure 2.2: Cross-section for electron-proton inelastic scattering. E and E' are the energies of the incident and scattered electron, respectively. Figure from [9].

can be employed.

The most general cross-section for inelastic electron-proton scattering mediated by a virtual photon has two independent functions, W_1 and W_2, of the two independent Lorentz invariant variables, Q^2 and ν. The cross-section is given by

$$\frac{d\sigma}{dQ^2 d\nu} = \frac{4\alpha^2}{Q^4}\frac{E'}{Em_p}\{W_2(\nu, Q^2)\cos^2\frac{\theta}{2} + 2W_1(\nu, Q^2)\sin^2\frac{\theta}{2}\}. \tag{2.6}$$

The functions $W_i(\nu, Q^2)$ are referred to as structure functions. It was predicted in the fall of 1968 [11] that in the limit $Q^2 \to \infty, \nu \to \infty$, but Q^2/ν finite

$$W_1(\nu, Q^2) \to F_1(x) \tag{2.7}$$

$$\frac{\nu}{m_p}W_2(\nu, Q^2) \to F_2(x), \tag{2.8}$$

where the dimensionless variable x is defined by†

$$x \equiv \frac{Q^2}{2m_p\nu} = \frac{Q^2}{2P\cdot q}. \tag{2.9}$$

The prediction can be understood as follows. If (2.7) and (2.8) are substituted into (2.6), and the functions F_i are still considered to be functions of two independent variables, then the cross-section can be written as

$$\frac{d^2\sigma}{dQ^2 dx} = \frac{4\alpha^2}{Q^4}\{(1-y)\frac{F_2(x, Q^2)}{x} + y^2F_1(x, Q^2)\}. \tag{2.10}$$

A comparison of the dimensions of each side of the equation shows that the structure functions, F_i, are dimensionless numbers, just as the form factor in Equation (2.3) is dimensionless. Hence, any quantities entering with dimension must have their dimensionality cancelled by some number of the same dimension. This number sets the *scale* of the interaction. In the case of the form factors, the scale is close to the proton mass since they give a measure of the size of the proton. However, as $Q^2 \to \infty$, the photons have an infinitesimal wavelength and there can be no dimension to set the scale as the photons probe infinitesimally small distances. The only way to cancel the dimensionality of Q^2 is with the variable ν, as in Equation (2.9). Therefore, the structure functions must be functions of x alone. This behaviour is known as *scaling*.

This prediction was confirmed by the first deep-inelastic scattering experiments [10]. They measured the cross-section for electron scattering from a hydrogen target at two fixed electron

†. The variable x is often referred to as Bjorken-x, after J.D. Bjorken who first introduced it.

scattering angles. The incident beam energies varied from 7 - 17 GeV and the scattering angles were such that Q^2 was in the range 1.6 - 7.4 GeV^2. At these values of four-momentum transfer, electromagnetic structure of the proton can be investigated. It was observed that νW_2 was independent of Q^2 and was only a function of x. Because scaling was observed at such low momentum transfers, it was called "precocious scaling".

2.2.2 The QPM

The theoretical framework originally devised to interpret the deep-inelastic scattering results was the Quark-Parton Model (QPM) [12], [13]. It postulates that the proton consists of point-like charged particles called *partons*. This furnishes the explanation for scaling since point particles have no dimensions and the scattering of an electron from an individual parton is elastic. In addition, it is assumed that the time scale of the interaction is much shorter than that which characterizes the strong interactions so that forces which lead to parton confinement can be neglected during the parton-electron interaction. This is the incoherent impulse assumption which is valid provided $Q, \nu \gg m_p$. It is tantamount to stating that the partons behave as free particles during the collision and can be visualized in a reference frame in which the target proton has a large three-momentum so that relativistic time dilation slows down the rate at which partons interact with one another†.

In this frame, all masses can be neglected and the partons' momentum is collinear with that of the proton. The mediating photon couples to a parton with four-momentum $p_i = \xi P$, so the parton four-momentum becomes $p_f = p_i + q$. The following relation then holds:

$$0 = p_f^2 = (p_i + q)^2 = p_i^2 + 2p_i \cdot q + q^2 = \xi 2P \cdot q - Q^2.$$

A comparison with Equation (2.9) shows that the scaling variable x corresponds to the momentum fraction of the parton struck by the photon, i.e. $x = \xi$. This means that a virtual photon with a given value of the variable x will only couple to a parton that has the momentum fraction x. Therefore, the cross-section, or equivalently $F(x)$ as seen from Equation (2.10), gives a measure of the momentum distribution of the parton constituents.

It was realized in 1968 [14] that the partons' spin could be obtained from a measurement of the ratio $(2xF_1(x)/F_2(x))$. Consider the cross-section for electron scattering from spin-1/2 pointlike particles of charge e_i and mass xm_p given by

†. A formal derivation of the QPM that does not make use of the *infinite momentum frame* is given in reference [13].

$$\frac{d\sigma}{dQ^2} = \frac{4\alpha^2 e_i^2}{Q^4}\left(\frac{E'}{E}\right)^2\left(\cos^2\frac{\theta}{2} + \frac{Q^2}{2x^2 m_p^2}\sin^2\frac{\theta}{2}\right). \tag{2.11}$$

If the partons are spin-1/2 and the scattering is incoherent, the coefficients of the angular factors in (2.11) and Equation (2.6) for the general electron-proton cross-section can be compared. This gives

$$2xF_1(x) = F_2(x). \tag{2.12}$$

Similarly, a comparison of the Mott cross-section for spinless particles with (2.6) implies that $F_1(x) = 0$, if the partons are spin-0. It was observed in electron-proton and neutrino-nucleon scattering experiments [15] that the relation (2.12) holds, thus indicating that the charged partons have spin-1/2.

The incoherence assumption allows the total cross-section for electron-proton scattering to be written as a sum of the cross-sections for electron-parton scattering. From equations (2.11) and (2.6), and using the relation (2.8), F_2 can be written as

$$\frac{F_2(x)}{x} = \sum_i^{n_f} e_i^2 \left(f_i(x) + \bar{f}_i(x)\right), \tag{2.13}$$

where f_i is the probability of finding a parton i with momentum fraction x and the sum is over all flavours of partons. That is, $F_2(x)/x$ is the mean square of the charge of the partons with four-momentum xP.

The sum over the momenta fractions x_i of all the partons must give unity from conservation of momentum. From Equation (2.13), the total momentum fraction carried by the charged partons can be obtained by integrating F_2 over x. In the early 1970's electron and neutrino scattering experiments demonstrated that the electroweakly interacting constituents of the nucleons only carried about 50% of the nucleon momentum [15]. This indicated the presence of uncharged partons. Although the picture of three valence quarks and a sea of quark-antiquark pairs could not account for the total momentum of the nucleons, this was not a contradiction within the QPM.

2.3 Quantum Chromodynamics

The early deep-inelastic experiments established that the observed partons had spin-1/2 and therefore corresponded to the quarks of the Quark Model. They also inspired the intuitive QPM. However, neither the Quark Model nor the QPM constitutes a theory of the strong interactions and, in particular, they are not concerned with the dynamics of the interaction. The principle

difficulty with formulating such a theory was that it was not understood why the strong interactions between the quarks did not mask the point-like behaviour. It had been proven that scaling would only occur in theories in which the coupling vanishes at short distances [16] and that no theories with Abelian gauge interactions possessed this property [17]. Therefore, scaling in deep-inelastic scattering would not occur if the strong interaction was described by an Abelian field theory like QED in which the interactions between two charged particles increases at short space-time distances.

The dilemma was resolved in 1973 with the discovery that at small space-time distances non Abelian gauge theories asymptotically approach free field theories [18]. The proposed symmetry group was SU(3) and it was conjectured that the symmetry is exact. The principal physical reason was the evidence, outlined at the end of Section 2.1, for colour as a quantum number, with three possible values, combined with the fact that no coloured hadronic states had ever been observed. The resulting theory of the strong interactions is called quantum chromodynamics (QCD).

QCD assigns to each flavour of quark three possible colour charges: R (red), G (green), and B (blue). For a given flavour, a three-component column vector, Ψ, can be formed, where each component is a different colour field. The symmetry group of QCD is $U(3)$, the group of unitary 3 x 3 matrices. An arbitrary group element is given by $U = e^{i\theta} e^{i\lambda_a \alpha_a}$, where the λ_a are the eight generators and α are the parameters of the subgroup of unitary matrices, $SU(3)$, with unit determinant. Since invariance under phase transformations has been discussed in the context of QED, QCD is concerned only with the group $SU(3)$, i.e. $e^{i\lambda_a \alpha_a}$.

Construction of the QCD Lagrangian, $\mathcal{L}_{QCD}$, proceeds with the requirement of invariance under transformations of the form

$$\Psi(x) \rightarrow U\Psi(x) \equiv exp\left(\frac{i}{2}\sum_a \lambda_a \alpha_a(x)\right)\Psi(x). \qquad (2.14)$$

The preservation of invariance of $\mathcal{L}_{QCD}$ under (2.14) implies the existence of eight vector gauge fields, G^a_μ, that are called gluon fields. The full gauge invariant Lagrangian is given by

$$\mathcal{L}_{QCD} = \overline{\Psi}(i\gamma^\mu \partial_\mu - m)\Psi - \frac{g}{2}\sum_{a=1}^{8}(\overline{\Psi}\gamma^\mu \lambda_a \Psi) G^a_\mu - \frac{1}{4}\sum_{a=1}^{8} G^a{}_{\mu\nu} G^{\mu\nu}{}_a, \qquad (2.15)$$

where m is the mass of the quark flavour under consideration. The gluon field strength tensor is

$$G^a_{\mu\nu} = \partial_\mu G^a_\nu - \partial_\nu G^a_\mu - g f_{abc} G^b_\mu G^c_\nu, \qquad (2.16)$$

where f_{abc} are the group structure constants and g the coupling.

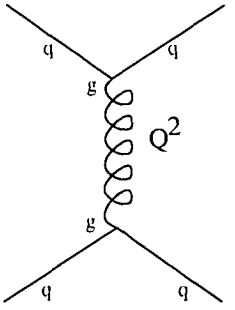

Figure 2.3: One gluon exchange quark-quark scattering.

In quantum field theory, it can be shown that the terms in the Lagrangian correspond to propagators and vertices of Feynman diagrams [8]. The propagators follow from the terms that are quadratic in the fields; interaction vertices of n lines are associated with the terms that contain n fields. Equations (2.15) and (2.16) show that the gluons are massless as there is no mass in the term corresponding to the gluon propagator. Furthermore, there are terms that are cubic and quartic in the gluon field that correspond to three and four gluon vertices. That is, the gluons not only serve to exchange colour but are coloured themselves and have self-interactions. This is a consequence of the fact that the symmetry group, *SU(3)*, is non-Abelian, i.e. the generators do not commute. In the Abelian gauge theory of QED there are no such self-interactions among photons.

The coupling, g, that appears in the expression for $\mathcal{L}$ characterizes the strength of the colour interaction. Consider, for example, the quark-quark scattering illustrated by the Feynman diagram in Figure 2.3. The negative square of the four-momentum transfer is denoted by Q^2. At each vertex is a factor g, so that the amplitude for the interaction is proportional to g^2. A strong coupling is defined by $\alpha_s \equiv \frac{g^2}{4\pi}$, which is proportional to the probability of gluon emission or absorption.

Assuming the validity of perturbation theory, to the next order there are further contributions to this basic graph, two examples of which are shown in Figure 2.4. The momentum of each line is indicated on the diagram on the right-hand side of Figure 2.4. Although four-momentum is conserved at each vertex, there is no restriction on the momentum, k, that appears on the loop and it should be summed over all possible values. This involves an integral of the form $\int \frac{d^4k}{(q+k)^2k^2}$, where the terms in the denominator are from the propagators. This integral diverges logarithmically at large k. If the application of perturbation theory is to be valid, some procedure

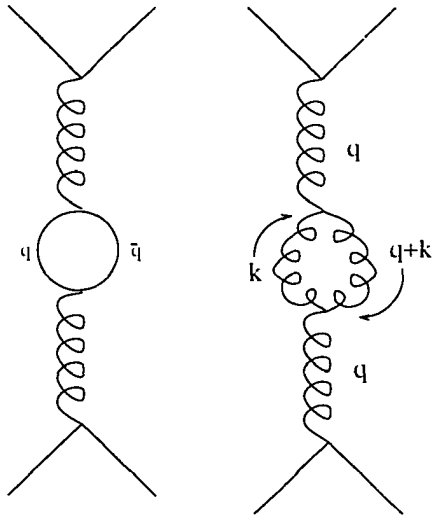

Figure 2.4: Higher order contributions to the one gluon exchange.

must be applied that renders finite the calculations of observable quantities.

The first step is *regularization*, a method to isolate the divergent terms in a well-defined manner. The most intuitive technique is to introduce a cut-off on the upper limit of the loop integrals. For non-Abelian gauge theories, however, *dimensional regularization* is employed [8]. The loop integrals are solved over $4-2\varepsilon$ dimensions because divergences are manifest as poles in $1/\varepsilon$.

The first part of dimensional regularization is to generalize the Lagrangian to $4-2\varepsilon$ dimensions. In order that all the terms have the correct dimension, the coupling g must be multiplied by μ^{ε}, where μ is an arbitrary mass scale. The loop integrals give two terms: one with the above mentioned pole and the other finite, of the form $\ln Q^2/\mu^2$.

The next step is renormalization. One approach is to introduce a new parameter, g_1, defined symbolically as $g_1 \sim g - 1/\varepsilon$. That is, the singular term is subtracted from the unrenormalized coupling†. The original, or *bare*, coupling, g, is regarded as being infinite. It has no physical significance since it corresponds to the coupling that would be measured if there were no higher order interactions. The actual measured value, however, includes contributions from an infinite number of diagrams. The coupling g_1 is the 1-loop approximation to the measured value. In a

†. This method of renormalization is known as *minimal subtraction*.

renormalizable theory, the procedure can be continued to higher orders. (A necessary condition for renormalizability of a theory is that the number of such divergent graphs is finite, which is the case for QCD.)

The finite term can also be absorbed into the coupling. This introduces a specific Q^2 dependence and the coupling is referred to as the *running coupling*. To eliminate the dependence on the regularization procedure, i.e. on the arbitrary parameter μ, $g(\mu)$ is subtracted from $g(\mu_1)$, where μ_1 is a reference momentum. The result for QCD is

$$\alpha_s(Q^2) = \frac{\alpha_s(\mu_1^2)}{1 + \frac{\alpha_s(\mu_1^2)}{12\pi}(33 - 2n_f)\ln(Q^2/\mu_1^2)}, \tag{2.17}$$

where n_f is the number of quark flavours with mass less than Q.

Equation (2.17) illustrates that as Q^2 becomes large, the coupling approaches zero. This property is known as *asymptotic freedom*. On the other hand, at some low $Q^2 = \Lambda^2$, the denominator is zero. Rewriting (2.17) in terms of Λ gives

$$\alpha_s(Q^2) = \frac{12\pi}{(33 - 2n_f)\ln(Q^2/\Lambda^2)}. \tag{2.18}$$

The scale Λ marks the boundary between perturbative and non-perturbative QCD. For values of Q^2 much larger than Λ, the coupling is small enough that perturbative expansions in α_s can be made.

The fact that the coupling grows with decreasing Q^2 lead to the belief that it could account for the confinement of quarks. Nevertheless, confinement has not yet been analytically proven as a consequence of asymptotic freedom. The difficulty is that perturbation theory cannot be applied at small values of Q^2, i.e. at large distances. One approach is lattice field theory. This indicates that the potential for a heavy quark-antiquark system rises linearly at large distances which would be a sufficient condition for confinement [19].

2.3.1 Gluon Contribution: Parton Dynamics

In contrast to the QPM, the gluons play a dynamical role in QCD, i.e. quarks can radiate gluons and gluons can split into $q\bar{q}$ pairs. There are two processes to first order in α_s: QCD Compton scattering, shown in Figure 2.5, and boson-gluon fusion, shown in Figure 2.6. The inclusion of these diagrams has two immediate experimental consequences for electron-proton

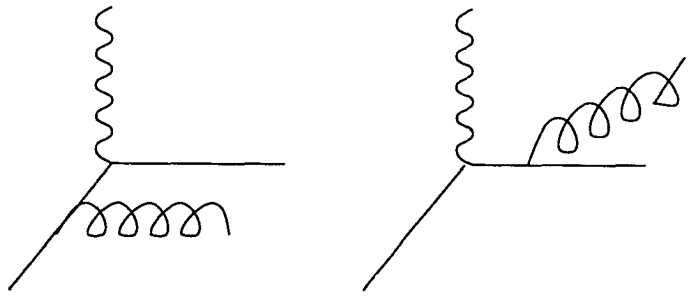

Figure 2.5: Contributing diagrams to the QCD Compton process.

scattering. First, the structure functions do not scale and, second, the outgoing quark is not collinear with the virtual photon in electron-proton scattering. The latter point is a consequence of gluon emission from the struck quark and is substantiated in Chapter 6. The first evidence for gluon emission came from the observation of three jet events in e^+e^- collisions in 1979 [20].

To understand the scaling violation, consider the QCD Compton process as an example. In the γ^*-parton center-of-mass frame, the cross-section for gluon emission is given by [21]

$$\frac{d\hat{\sigma}}{dp_T^2} \propto \frac{1}{p_T^2}\frac{\alpha_s}{2\pi}P_{q\to qg}(z)\,, \tag{2.19}$$

where p_T is the transverse momentum of the outgoing quark with respect to the photon. The *splitting function,*

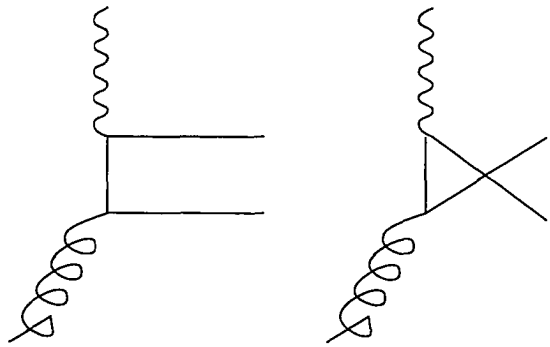

Figure 2.6: Contributing diagrams to the boson-gluon fusion process.

$$P_{q \to qg}(z) = \frac{4}{3}\left(\frac{1+z^2}{1-z}\right), \tag{2.20}$$

is the probability of a quark with momentum yP emitting a gluon and having its momentum reduced by a factor z to xP. Equation (2.19) must be integrated to add the QCD Compton process to the QPM cross-section.

The maximum transverse momentum is given by

$$(p_T^2)_{max} = Q^2 \frac{1-z}{4z} = \frac{Q^2}{4}\frac{y-x}{x}. \tag{2.21}$$

Therefore, in the large x limit, $(p_T^2)_{max} \sim Q^2$. However, for low x, the kinematic limit on p_T^2 can be much larger than Q^2. This becomes quite clear in the analysis of the deep-inelastic scattering data in Chapter 6.

Assuming large Q^2, the integration of Equation (2.19) gives a term $\ln(Q^2/\mu^2)$,† where μ^2 regularizes the $p_T \to 0$ divergence. This is known as a *collinear* or *mass* divergence. Most of the emitted gluons will be collinear with the parent quark because of this singularity.

There is a second singularity in the gluon emission cross-section as $z \to 1$ in Equation (2.20). This corresponds to the emission of very low energy, or *soft*, gluons. This singularity is cancelled by virtual corrections to the basic QPM process. Such corrections are also singular as $z \to 1$ and are related to the emission and absorption of gluons.

The dilemma now is that the "perturbative correction" from the integration of Equation (2.19) contains an $\alpha_s(Q^2)\ln Q^2$ term which does not vanish as $Q^2 \to \infty$. This is similar to the problem encountered in calculating the running coupling. It is solved by redefining the quark densities, $f_i(x, Q^2)$, in such a manner that the Q^2 dependency is assigned to the quark densities. The structure functions thereby become functions of x and Q^2. The $\ln Q^2$ term is a direct consequence of high transverse momentum gluon emission.

The physical interpretation of this result is that a photon with a given Q^2 can resolve a quark and a gluon if the transverse separation between them is greater than $1/Q$. Since the gluon emission cross-section increases with decreasing transverse momentum, there are more partons that have a small transverse separation than a large separation. The number of resolved partons therefore increases with Q^2. The first deep-inelastic scattering experiments were at a relatively low Q^2 making it unlikely that such virtual quark-gluon states would exist long enough to separate

†. It is assumed that α_s is constant and small for simplicity and to illustrate that the Q^2 dependence does not come from the coupling alone; it should really be $\alpha_s = \alpha_s(p_T^2)$.

by $1/Q$. Qualitatively, this has the effect that the structure functions will increase with increasing Q^2 at low x since there is an increasing probability that the photon will strike a low x parton, and conversely, for high x the structure functions should decrease with increasing Q^2. This is illustrated in Figure 2.7. It can also be seen that at moderate x, around 0.25, and low Q^2 the structure functions do indeed scale. This was the region explored by the early deep-inelastic scattering experiments.

The boson-gluon fusion subprocess also contributes to the cross-section and has a $\ln Q^2$ term. It has a splitting function given by

$$P_{g \to q\bar{q}}(z) = \frac{1}{2}(z^2 + (1-z)^2), \tag{2.22}$$

where z is the fraction of the gluon's momentum carried by the quark.

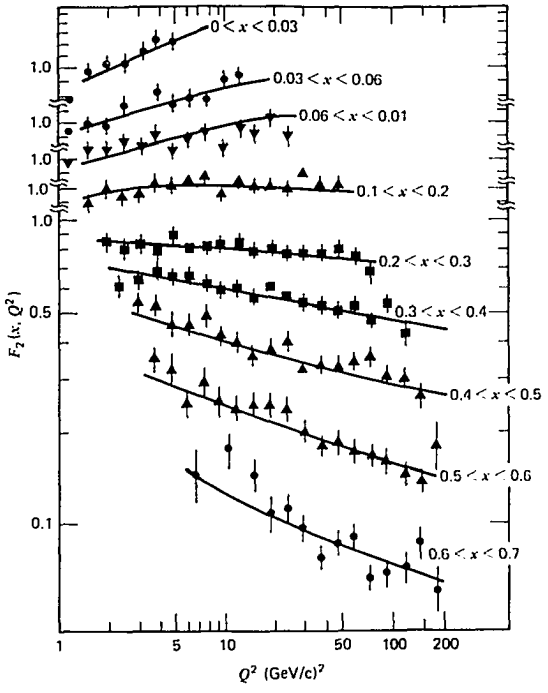

Figure 2.7: Structure function behaviour as a function of Q^2. The data is from the CDHS counter experiment at CERN [22].

The preceding discussion focused exclusively on the first order diagrams. A proper treatment requires that all higher order corrections be included, but this is difficult. However, for x greater than about 10^{-2}, the dominant contribution to the cross-section arises from terms of the form $(\alpha_s \ln Q^2)^n$, which can be analytically summed. This is known as the *leading logarithm approximation*. Each logarithm is associated with a collinear singularity. The evolution of $f_i(x,Q^2)$ with Q^2 is given in this approximation by the Altarelli-Parisi equation [23]

$$\frac{df_i(x,Q^2)}{d\ln Q^2} = \frac{\alpha_s}{2\pi}\int_x^1 \frac{dy}{y}\left(f_i(y,Q^2)\,P_{q\to qg}\left(\frac{x}{y}\right) + g(y,Q^2)\,P_{g\to q\bar{q}}\left(\frac{x}{y}\right)\right), \tag{2.23}$$

where the gluon density, $g(x,Q^2)$, has been introduced. Its evolution equation is given by

$$\frac{dg(x,Q^2)}{d\ln Q^2} = \frac{\alpha_s}{2\pi}\int_x^1 \frac{dy}{y}\left(\sum_i f_i(y,Q^2)\,P_{q\to gq}\left(\frac{x}{y}\right) + g(y,Q^2)\,P_{g\to gg}\left(\frac{x}{y}\right)\right), \tag{2.24}$$

with splitting functions

$$P_{q\to gq}(z) = \frac{4}{3}\frac{1+(1-z)^2}{z} \tag{2.25}$$

and

$$P_{g\to gg}(z) = 6\left(\frac{1-z}{z} + \frac{z}{1-z} + z(1-z)\right). \tag{2.26}$$

These equations formulate how the probability that a parton with momentum fraction x came from a parent parton with fraction y varies with Q^2. As x becomes small, these equations predict rapidly growing distributions and must break down as $x \to 0$.

Although the QPM is no longer a viable model, comparisons with QCD predictions illustrate nicely the effects of gluons. The term QPM henceforth will be taken to mean that a struck quark is chosen according to the QCD evolved structure functions, but that it does not radiate. In the language of perturbation theory, this will be referred to as an α_s^0 process.

2.4 QCD Models

So far, the focus has been on cross-section measurements, i.e. F_2, to give information on proton structure. A measurement of the scattered electron's energy and angle suffices for this purpose; it is not necessary to observe the hadronic final state. Nevertheless, the details of the production of final state hadrons is dominated by both perturbative and non-perturbative QCD effects since the source of hadron production is gluon radiation. It is essential to have models which accurately simulate the real data and allow the non-perturbative effects to be unfolded in

order to physically interpret the experimental observations and test the perturbative regime.

In the case of e^+e^- annihilation experiments, such models give a description of the final hadronic state that can reproduce even fine details of the data [24]. The deep-inelastic process is more complex for several reasons. The incoming proton can give rise to initial state QCD radiation, the kinematics of the primary interaction depend on more than one variable, and finally, the character of the proton remnant is not well understood. Even so, several of the models discussed below give a satisfactory representation of lower energy deep-inelastic scattering data. The new range of kinematics opened up by the HERA collider allows a more detailed study, particularly of the dependence on the kinematic variables.

Results from the lower energy deep-inelastic scattering experiments have shown that perturbative QCD corrections to the QPM are required to describe the hadronic final state [25], [26], [27]. The recent observation of two jet production in deep-inelastic scattering by ZEUS [28] shows clearly that higher order processes giving rise to multi-partonic final states are important at HERA energies and so must be included in the simulation.

2.4.1 First Order Matrix Elements

The proper way to include higher order QCD contributions is to calculate the exact matrix elements order by order in α_s. However, only partial second order results exist for deep-inelastic scattering [29]. In addition to the leading order reaction, $\gamma^* + q \rightarrow q$, the QCD Compton and boson-gluon fusion processes contribute to first order. The exact matrix elements [30] can be used to simulate these processes.

In order to calculate cross-sections for these reactions, it is necessary to avoid singularities that correspond to the emission of low energy or collinear gluons. Examples of these appear in Equations (2.19) and (2.20) which describe the QCD Compton process. There are singularities as $z \rightarrow 1$ and as $p_T^2 \rightarrow 0$. In a theoretical calculation, they are partly cancelled by including diagrams with virtual gluons and partly absorbed in the parton density functions.

A Monte Carlo generator must use a cut-off. Since the invariant mass of two massless partons i and j is given by $m_{ij}^2 = E_i E_j (1 - \cos\theta_{ij})$, it is a convenient variable to use to avoid soft and collinear divergences. The cut, $m_{ij}^2 = y_{cut} W^2$, is applied to all pairs of partons in the final state, including the proton remnant. The parameter y_{cut} must be set as low as possible to minimize the exclusion of emission phase space, i.e. if it was set too high, only energetic gluons with a high transverse momentum with respect to the quark would be simulated. On the other hand, it cannot

be too low because perturbation theory loses its validity close to the divergences. It is necessary to treat the effects of soft and collinear partons in the non-perturbative simulation phase.

The matrix elements are combined with the electroweak scattering cross-section in the Monte Carlo program LEPTO† [31]. The generator integrates over the matrix elements in order to obtain the probabilities for qg or $q\bar{q}$ events. The probability for an α_s^0 process is then given by $P_q = 1 - P_{qg} - P_{q\bar{q}}$. The value of y_{cut} used in the simulations was the default value of 0.0025. The predictions of this model can reproduce the general features of the current fixed target deep-inelastic scattering experiments, but detailed studies show that soft gluon radiation effects need to be added to the model [26], [27], [32]. This simulation is denoted by ME.

2.4.2 Parton Showers

The drawback with the first order matrix elements is that at most two partons are produced in the partonic final state. In higher orders, one generally expects several partons. Models based on the leading logarithm approximation can be employed. Unlike the matrix element approach, these models do not automatically take into account all interference effects among the partons and usually have modifications for such *coherence* effects. One model that simulates multi-parton states is the parton shower (PS) model.

In this picture, the proton is imagined as consisting of a set of partons, close to mass-shell, each of which can initiate a cascade of virtual partons. If a quark is scattered out of the proton, the cascade to which it belonged cannot recombine. Thus, the struck quark can emit partons before the boson vertex. This process is shown in Figure 2.8. As the quark is radiating this *initial state shower* it becomes more off-shell or virtual. After the interaction, the quark may again be off mass-shell and returns to the mass-shell by radiating the *final state shower*. The amount and hardness of the radiation are functions of the maximum virtuality of the struck quark just before, and just after, the interaction with the virtual photon.

2.4.2.1 Lund Approach

The Lund parton shower model for deep-inelastic scattering [33] is available in the program LEPTO. The procedure begins with an arbitrary separation of radiation into an initial state shower and a final state shower. This approximation is not covariant and it is implicit that interference

†. LEPTO version 6.1 was used for the simulations shown in this thesis.

effects between the two showers are neglected. It is valid in the case that there are few hard or wide angle emissions. This could be the case for high x partons that have not lost much energy through initial state radiation.

The development of each shower is given in the leading logarithm approximation. Suppose that an initial state cascade is initiated by the branching $p_5 \rightarrow p_3 + p_4$, as described by the Altarelli-Parisi splitting kernels and where p_5 is close to, but not on, mass shell. Since one is interested in generating real partons, let p_4 be real. The kinematics then require that p_3 must be spacelike, i.e. emission of timelike partons will make subsequent internal parton momenta spacelike. Studies of the dominant collinear singularities [21], [34] show that the maximum number of leading logarithm contributions to the cross-section occur in the phase space region in which the virtual masses of the space-like partons form a monotonically increasing sequence, with the largest values closest to the hard scattering, i.e.

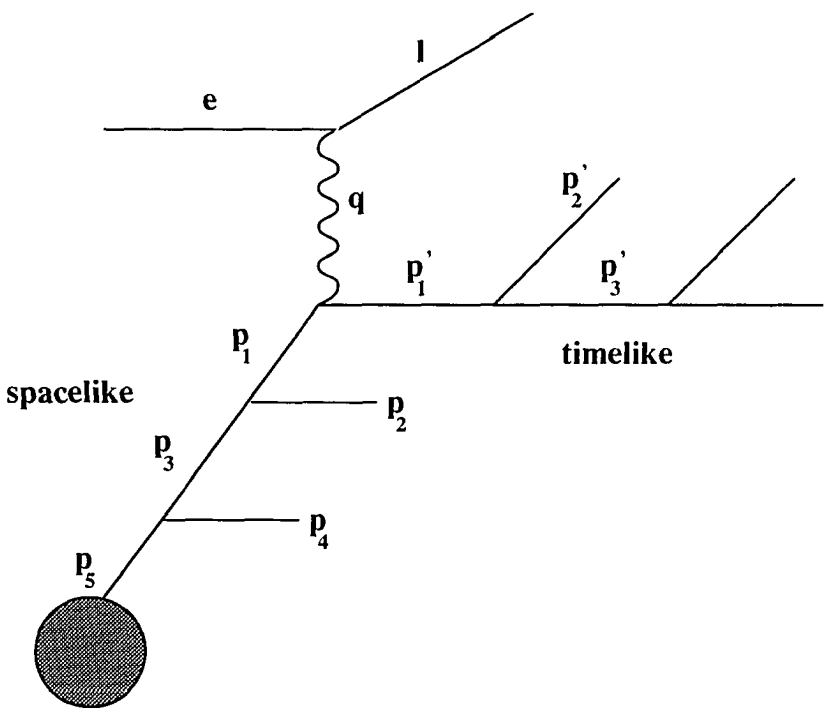

Figure 2.8: QCD picture of neutral-current deep-inelastic scattering with initial and final state radiation.

$$|Q_0^2| = |p_n^2| < \ldots < |p_3^2| < |p_1^2| = |Q_{max}^2|. \qquad (2.27)$$

This is convenient since the condition (2.27) is necessary in order to describe the shower through an iterative Monte Carlo procedure. The physical interpretation of this result is that more structure is observable as the hard scattering scale increases and that interference effects reduce emission outside of the phase space region given in (2.27).

Infrared singularities are not taken into account. These correspond to the emission of soft gluons, where soft means that the gluon energy is small compared to the scale of the hard process. However, the initial state kinematics, with ordered virtualities, implies that the opening angles of the branches tend to increase toward the boson vertex. (This is true unless the gluons become very soft, i.e. $z \rightarrow 1$.) Since this reduces considerably the number of kinematically possible configurations, there may be a reduced possibility that soft gluon interference effects are important.

For reasons of efficiency, the actual simulation of the initial state shower is usually performed with a backwards evolution scheme [35] from the hard interaction to the shower initiating parton. In forward evolution, a parton a is selected at Q_0^2 according to $f_a(Q_0^2, x_0)$ and evolved to increasingly higher virtualities. A priori, it is not known whether this particular cascade will result in a parton with an x and Q^2 that will lead to the correct cross-section. This is inefficient as it leads to a rejection of many events. Since the structure functions correspond to an inclusive summation over all initial state parton showers, one essentially needs to perform this sum in order to obtain the correct Q^2 evolution of the structure functions. The backwards evolution scheme avoids this by using the knowledge of the Q^2-evolved structure functions. The hard scattering is selected according to the proper cross-section and the shower is evolved backwards using the structure functions at all scales to ensure that the initial parton momentum fraction matches onto the proton structure function.

In order to carry out this procedure, recall that the Altarelli-Parisi equations express the fact that during a small increase in Q^2 there is a probability for parton a, which momentum fraction $y > x$, to be resolved into a parton b with fraction x and a parton c with fraction $y - x$. That is, df_i in Equation (2.23) is the decrease in the probability of finding parton i. This is reversed in the backwards evolution: with a decrease in Q^2 there is a probability that partons b and c can no longer be resolved. Using (2.23), this probability is given by [35]

$$dP_b = \frac{df_b(Q^2, x)}{f_b(Q^2, x)} = |d\ln Q^2| \frac{\alpha_s(Q^2)}{2\pi} \sum_a \int \frac{dy}{y} \frac{f_a(Q^2, y)}{fb(Q^2, x)} P_{a \rightarrow bc}(\frac{x}{y}). \qquad (2.28)$$

The probability, S_b, that parton b can still be resolved as Q^2 changes from some Q^2_{max} to $Q^2 < Q^2_{max}$ is given by the sum of the probabilities dP_b subtracted from unity. The result is

$$S_b(x, Q^2_{max}, Q^2) = exp\left\{-\int_{Q^2}^{Q^2_{max}} d(\ln Q'^2)\frac{\alpha_s(Q'^2)}{2\pi}\sum_a \int dz P_{a\to bc}(z)\frac{xf_a(x,Q'^2)}{xf_b(x,Q'^2)}\right\}, \quad (2.29)$$

where S is known as the Sudakov form factor. Because of the unitarity condition, i.e. that S_b is one minus the sum of real branching probabilities, the Sudakov form factor sums the virtual corrections in the leading logarithmic approximation.

An important feature is the presence of the structure functions. This arises because the probability to find a parton b that has branched from parton a depends on the probability to find parton a. It ensures that the backwards evolution scheme gives the correct evolution of the structure functions without the need for rejecting events. As a simple example, consider lepton scattering off of a heavy quark. The denominator, f_b in Equation (2.29), equals zero below the production threshold, thereby guaranteeing that there will be no heavy flavours below this threshold.

The first step in tracing the shower backwards is to choose the virtuality of the parton b in the branching $a \to bc$ from dS_b/dQ^2. The given branching, i.e. the parton a, is chosen from the z integrals in (2.29) which give the relative probabilities for the allowed branchings. Finally, the probability in the splitting variable, z, is given by the z integrand. This procedure is iterated down to the shower initiator which typically has a cut-off virtuality, Q^2_0, of about 1 GeV^2.

Once the incoming parton has interacted with the current, it acquires a timelike virtuality and returns to mass shell through parton radiation. The idea is the same as that used in the simulation of the spacelike showers. Now, the Sudakov form factor expresses the probability that parton a does not branch between some initial mass squared, m^2, and a minimum m^2_0, and is given by

$$S_a(m^2) = exp\left\{-\int_{m_0^2}^{m^2}\frac{dm'^2}{m'^2}\int_{z_2(m')}^{z_1(m')} dz\frac{\alpha_s(Q^2)}{2\pi}P_{a\to bc}(z)\right\}. \quad (2.30)$$

In the case of timelike showers [36], the kinematics implies an ordering in the virtualities. The leading collinear singularities and virtual graphs are correctly incorporated. The proper inclusion of the leading infrared, or soft, singularities requires a simple modification of the branching algorithm: the opening angles of the branches must decrease monotonically with decreasing masses [37]. Outside of the angular ordered region soft gluon coherence causes destructive interference resulting in a reduction of gluon emission.

2.4.2.2 Virtuality Scale

The choice of scale for the maximum virtuality in the initial and final state showers is an extremely important one for any parton shower model. The virtuality scale governs the amount of gluon radiation from the struck parton before and after it interacts. It also determines the transverse momentum carried by the struck quark, since it recoils after each gluon emission. In contrast to e^+e^- annihilation, there is no unique scale in deep-inelastic scattering. It could be any function of Q^2 or W^2. Since the invariant mass of the hadronic final state is given in terms of Q^2 and x by

$$W^2 = Q^2 \frac{1-x}{x} + m_p^2, \tag{2.31}$$

W^2 is on the same order of magnitude as Q^2 at large x, but is much larger at small values of x.

The phase space limit is given by $W^2/4$. This can be seen from Equation (2.21) which gives the maximum p_T for a quark with momentum yP to have its momentum reduced to xP through gluon emission. (This variable y is not the kinematical variable defined by Equation (2.5).) The phase space limit is given if y is equal to unity. A comparison of (2.21) and (2.31) shows that $(p_T^2)_{max}$ is $W^2/4$. Therefore, W^2 should be used as the scale to get the full emission phase space, but this means that $\langle p_T^2 \rangle$ will scale as W^2. This is reasonable for large x, since y must be greater than x and is consequently almost always close to unity. However, it is unlikely that quarks with a small momentum fraction x are the result of highly energetic gluon emission by quarks with a large momentum fraction. Therefore, for small values of x the choice of W^2 could overestimate the amount of radiation and Q^2 is perhaps a better choice.

These two extreme choices of the virtuality scale are available in LEPTO. Their predictions, denoted by PS(Q^2) and PS(W^2), are investigated in this thesis. The predictions of the PS(W^2) model are in general agreement with data from the E665 and EMC fixed target experiments that together cover a W^2 range of 20 to 1000 GeV^2 and a Q^2 range of 4 to 1000 GeV^2 [26], [38]. Since most of the data is at low Q^2, the PS(Q^2) model is similar to the QPM and is not in agreement with the data [32]. At the larger range of Q^2 accessible at HERA, it is plausible the model could give more accurate predictions. Although there are not convincing theoretical arguments for either choice of scale, they span the range of possibilities predicted by this model.

An intermediate scale can be chosen based on the limiting behaviour of the matrix elements at low and high x [31]. In the first order matrix elements, $\langle p_T^2 \rangle$ is approximately $Q^2(1-x)$ as

$x \to 1$, and is approximately $Q^2 \ln(1/x)$ as $x \to 0$. This leads to a scale choice given by $Q^2(1-x)\max(1, \ln\frac{1}{x})$. The LEPTO parton shower model with this scale is denoted by PS(Q^2(1-x)).

2.4.2.3 Parton Showers - The Herwig Approach

An alternative Monte Carlo program that incorporates the parton shower approach is HERWIG† [39]. It provides a more sophisticated treatment of coherence effects, than does LEPTO, based on a theoretical analysis of the leading collinear and infrared contributions in a general hard process [40], [41]. The remarkable result of this work is that the initial state radiation can be described as a branching process that is suitable for Monte Carlo simulation even with the inclusion of the leading infrared contributions. This is a consequence of the fact that the interference is fully destructive to leading order outside of a suitably defined emission phase space region.

The leading infrared singularities in the spacelike cascade can be taken into account by confining the emission phase space to the region

$$E_{i+1}\theta_{pq_{i+1}} < E_i\theta_{pq_i}, \tag{2.32}$$

where E_i is the energy of the ith spacelike parton and θ_{pq_i} is the angle between the incoming parton p, labelled p_5 in Figure 2.8, and the ith time-like parton q_i. The index i increases as one moves away from the hard scattering. The reason this is more complicated than the angular ordering of the timelike emissions is related to fact that the virtuality of the radiating spacelike parton increases as its energy decreases, whereas in the timelike case, the virtuality of the parton decreases as its energy decreases. At high x, E_{i+1} is small and therefore the energy, E_i, of its parent cannot be much larger. The ordering (2.32) reduces to angular ordering in this case. At low x, E_{i+1} can be small and E_i can be much larger. Therefore, the ordering (2.32) is expected to be important in the low x region.

By using an evolution variable proportional to the product in equation (2.32), the destructive interference can be incorporated into a Monte Carlo generator using the same techniques discussed above. The evolution variable for initial state showers is given by

$$Q_i = E_i\sqrt{\xi_i}, \qquad \xi_i = (p \cdot q_i)/(E\omega_i), \tag{2.33}$$

where E is the energy of the parton p and ω_i that of q_i. The ordering is now

†. Herwig version 5.6 was used for the simulations presented in this thesis.

$$Q_{i+1} < Q_i, \tag{2.34}$$

which reduces to (2.32) for small angles. The evolution variable for the final state showers [42] is

$$Q_i = E_i\sqrt{\xi_{ij}}\ , \qquad \xi_{ij} = (p_j \cdot p_k)/(E_j E_k), \tag{2.35}$$

for the branching $i \rightarrow jk$. As with LEPTO, angular ordering is imposed. The maximum virtuality scale in HERWIG is approximately Q^2. The choice of scale is not available as an option for the program user, but this does not mean that it is more constrained than in LEPTO.

There are a number of other coherence effects treated in HERWIG. Interference between the initial and final state showers is simulated in the following approximation. Each parton shower takes place inside a cone of angular size set by the angle between that parton's initial momentum vector and that of its colour connected partner. For example, the initial state shower cannot emit a parton at an angle greater than the scattered parton. Furthermore, within each shower the radiation is not emitted symmetrically in the azimuth, but is preferentially emitted in the direction of the initiator of the other shower. There are further azimuthal correlations due to, e.g., gluon spin polarization, but these are not important for the purposes of this thesis.

HERWIG is able to give satisfactory overall agreement with fixed target experimental data [32]. Since both HERWIG and the PS(Q^2) model essentially the same maximum virtuality scale, this may seem like a contradiction. However, it is difficult to distinguish between perturbative and non-perturbative effects at these energies. For instance, HERWIG produces a perturbatively produced gluon in only about 25% of the events at current fixed target energies.

2.4.3 Matrix Elements and Parton Showers

Two approaches to modelling the partonic final state, each with its own advantages and limitations, have just been outlined. The first order matrix elements are exact, but give at most two partons. The parton showers give an arbitrary number of partons, but are simulated in the leading logarithm approximation, so that the treatment of hard partons at large angles is not correct. LEPTO allows the possibility of adding parton showers to the first order matrix elements [31]. This model is denoted by ME+PS. It gives the exact first order hard emissions of the boson-gluon fusion and QCD Compton processes and, in addition, limits the choice of virtuality scale for the parton showers.

A hard emission is generated using the matrix elements and extra, but softer, emissions are

then added using parton showers. In the case that the matrix elements give no first order process, i.e. no radiation harder than the cut-off $y_{cut}W^2$, the parton shower has to be constrained to simulate only soft emissions to avoid double counting of hard emissions. The cut-off is used, therefore, as the maximum virtuality for the initial and final state parton showers. The showers are then simulated as described in Section 2.4.2.1.

If a first order event is generated, the two final state partons are allowed to radiate as a system. It is impossible to determine unambiguously all the propagator virtualities because matrix element calculations are represented as the square of a sum of different Feynman diagrams. In the QCD Compton process, for example, it cannot be stated whether the gluon was emitted before or after the boson vertex. In LEPTO, the maximum virtuality of the final state showers is taken to be the invariant mass of the two hard outgoing partons.

Consider the QCD Compton process with the gluon emitted after the boson vertex. The invariant mass squared of the quark-gluon system is equal to the virtuality of the quark propagator just after the boson vertex and, therefore, is the correct maximum virtuality. This is not the correct choice if the gluon was emitted before the boson vertex, but it is reasonable if the two partons radiate as a system [43]. In the boson-gluon fusion process, the invariant mass of the outgoing quark-antiquark pair is used as the maximum virtuality.

The correct maximum virtuality for the initial state parton shower is the virtuality of the quark propagator just before the boson vertex. The largest of the possible virtualities is used for the initial state shower. Although the parton shower scale is not specified uniquely by the above prescription, it is constrained.

Since the matrix element calculation is unreliable in the infrared and collinear singular regions, it is desirable to raise the y_{cut} value if possible. The addition of parton showers allows this as they give a correct leading treatment of the collinear and infrared singularities in the timelike showers and of the collinear singularities in the spacelike showers. The value used in the simulations presented in this thesis was 0.01, although the default is 0.015.

The ME+PS model has only recently been made available. Initial tests of the model show that it gives reasonable agreement with fixed target experimental data [32].

2.4.4 Colour Antennae

A different approach to the formulation of the results of perturbative QCD is illustrated best with

the example of $q\bar{q}$ pair production in e^+e^- annihilation. To order α_s, either the q or the $\bar{q}$ can emit a gluon. The exact, first order cross-section for gluon emission is given by [44]

$$\frac{1}{\sigma}\frac{d\sigma}{dx_q dx_{\bar{q}}} = \frac{2\alpha_s}{3\pi}\frac{x_q^2 + x_{\bar{q}}^2}{(1-x_q)(1-x_{\bar{q}})}, \tag{2.36}$$

where $x_i = 2E_i/\sqrt{s}$ and $\sqrt{s}$ is the centre-of-mass energy of the system. The $q\bar{q}$ system is essentially a colour dipole, or a *colour antenna*, which can radiate. Figure 2.9(a) shows two colour connected quarks, with colour charges r and $\bar{r}$, in their center-of-mass frame. Gluon radiation from the dipole is given by Equation (2.36) and is shown in Figure 2.9(b). Unlike electromagnetic radiation, the gluon carries colour charge, as is illustrated by the emission of an $r\bar{b}$ gluon.

The system now comprises two colour dipoles. It can be shown that the emission of a second, softer gluon can be treated as radiation from two independent dipoles [45]: one formed by the quark and the gluon and the other by the gluon and the antiquark. In this approximation, the term corresponding to the dipole between the quark and the antiquark is neglected. It has a relative magnitude $1/N_c^2 = 1/9$, where N_c is the number of colours. This result is generalized in the colour dipole model [44] [46] so that the emission of a third, softer gluon is given by three independent dipoles and so forth.

In addition to the $q\bar{q}$-dipole, there are also qg- and gg-dipoles. The matrix elements for the processes $q^* \rightarrow qgg$ and $g^* \rightarrow ggg$ are used to calculate the cross-sections. Consider gluon emission from the qg-dipole resulting in a gg- and qg-dipole. If the two final state gluons have the

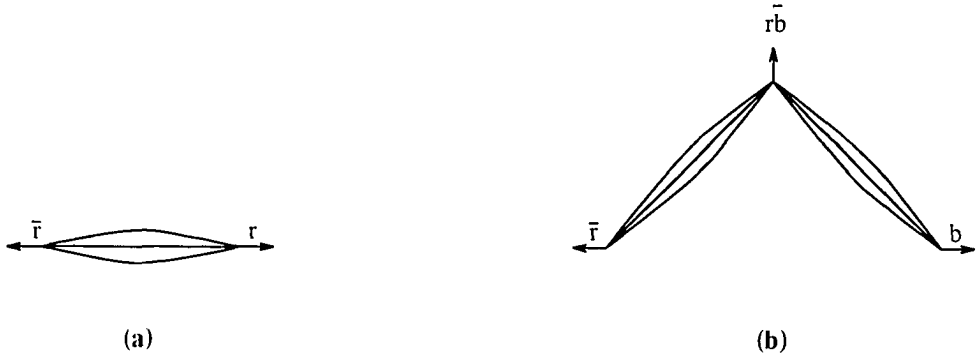

Figure 2.9: (a) $q\bar{q}$ colour dipole. (b) Radiation of rb gluon from the dipole; the system now comprises two dipoles.

same colours, it is not known which of the two gluons belongs to the qg-dipole. This ambiguity corresponds to an interference term in the cross-section. These are neglected since they are of order $1/N_c$. The cross-sections for the qg- and gg-dipoles in this approximation are given by [44], [47]

$$\frac{1}{\sigma}\frac{d\sigma}{dx_q dx_g} = \frac{3\alpha_s}{4\pi}\frac{x_g^3 + x_q^2}{(1-x_q)(1-x_g)}, \tag{2.37}$$

$$\frac{1}{\sigma}\frac{d\sigma}{dx_g dx_g} = \frac{3\alpha_s}{4\pi}\frac{x_g^3 + x_g^3}{(1-x_g)(1-x_g)}. \tag{2.38}$$

The colour dipole model automatically takes into account soft gluon coherence, including the dependence of the interference on the azimuthal angle. For emission of harder gluons, the above cross-sections are equivalent to the leading logarithm approximation. Although interference effects cannot be ignored for hard gluon radiation, the hope is that since the model automatically treats soft gluon interference correctly, it will provide a good approximation also in the regime of hard gluon radiation.

In electron-proton scattering, the struck quark and the proton remnant are considered to form a colour dipole. When this dipole radiates a gluon, it splits into two radiating dipoles: one between the gluon and the struck quark and the other between the gluon and the remnant. Repeated gluonic emissions lead to a chain of such dipoles. The radiating dipoles are not completely independent. The emissions are ordered as $p^2_{\perp 1} > p^2_{\perp 2} > p^2_{\perp 3} > \ldots p^2_{\perp n}$, where the momenta are calculated in the dipole center-of-mass system and $p^2_{\perp} \sim (1-x_i)(1-x_j)$. This is necessary because of the low $p_{\perp}$ divergences in the dipole cross-sections. A Sudakov form factor gives the probability of emitting a gluon between some $p^2_{\perp max}$ and $p_{\perp}$.

Unlike the e^+e^- case, one end of the dipole system in deep-inelastic scattering is not point-like as the proton remnant is an extended object. The proton is considered to be a one dimensional chain of colour dipoles in the hadronic centre-of-mass system. After the interaction, the struck endpoint will be moving in one direction and the extended remaining system will be moving in the opposite direction. Emission of wavelengths smaller than the transverse size of the antenna is suppressed, i.e. only a region of the dipole with transverse extension $\lambda/2$ gives constructive interference for emission of a wavelength λ, where $\lambda \propto 1/p_{\perp}$. The transverse size of the remnant is a parameter in the CDM that must be determined by experiment. It was determined from EMC data to be in the range 0.6 - 1.0 GeV^{-1} [48]. This is in accord with the intuitive expectation that it should be on the order of the proton size.

As a result of the suppression of short wavelength emissions, the maximum $p_\perp^2$ in the hadronic centre-of-mass system for an emitted gluon varies as $W^{4/3}$ [48]. This is less than the kinematical limit, W^2, that is possible with the PS(W^2) model. The colour dipole model is coded in the program ARIADNE† [49], which in turn is interfaced to that part of LEPTO that generates the hard scattering. This simulation will be denoted by CDM.

A missing component in the dipole model is the inclusion of the boson-gluon fusion process in which both a quark and an antiquark can form dipoles with the remnant. The provision has been made in ARIADNE to include this process as given by the first order matrix elements. LEPTO is used to generate the hard process according to first order in α_s. In the case of a QCD Compton process, the gluon is removed and regenerated by dipole radiation. In the case of a boson-gluon fusion event, two independent dipoles are formed with the remnant. This will be referred to as CDM+BGF.

2.5 From Partons to Hadrons

The methods of perturbative QCD cannot be applied to the hadronization process, i.e. the confinement of the partons into colourless bound states, because the coupling $\alpha_s(Q_0^2)$ becomes too large to allow a perturbative expansion. At present, phenomenological models are implemented in Monte Carlo programs.

Immediately after the hard interaction, the struck parton is off its mass shell. It behaves as a free colour charge as it returns to mass shell through radiation. Hadronization only begins with partons that are close to mass shell and, thus, should be independent of the hard interaction. This implies that hadronization is universal i.e. a model that works for e^+e^- annihilation can be applied to electron-proton collisions. The so-called string and cluster models are used in the Monte Carlo programs that are studied in Chapter 6. Both models are already constrained by e^+e^- and fixed target deep-inelastic scattering data, but the string model seems to give a better overall description of the data [50].

2.5.1 String Hadronization

The Lund string model [51] is based on the assumption that the energy stored in the colour field between a colour charge and an anticharge increases linearly with the separation between the

†. ARIADNE version 3.1 was used for the simulations presented in this thesis.

charges. One way of visualizing this is as a colour flux tube of uniform energy density. A proper mathematical description of the energy flow is provided by the dynamics of a relativistic string with no transverse degrees of freedom.

Consider the example of quark-scattering from within a proton. As the quark and remnant diquark move apart, the potential energy stored in the string increases. The string may subsequently break into two colour singlet pieces through the production of a $q\bar{q}$ pair from the vacuum when the energy is greater than the mass of a $q\bar{q}$ pair. If the invariant mass of the string pieces is large enough, they will break up further until only on-mass-shell hadrons remain.

The tunneling probability for production of a $q\bar{q}$ pair is proportional to

$$exp\left(\frac{-\pi m^2}{\kappa}\right)exp\left(\frac{-\pi p_T^2}{\kappa}\right), \tag{2.39}$$

where p_T is the transverse momentum with respect to the string axis, m is the mass of the produced quark flavour, and κ is the string energy per unit length. Since the string has no transverse excitations, the $q\bar{q}$ pair balance the p_T. The produced hadrons thereby acquire p_T from their constituents. Equation (2.39) also implies the suppression of heavy quark production. If a gluon was emitted, it would be represented by a *kink* on the string carrying energy and momentum equal to that of the gluon. The average transverse momentum is governed by the parameter σ_q, per $\langle p_T^2 \rangle = 2\sigma_q^2$.

The energy-momentum four-vector of each hadron is given by a fragmentation function, $f(z)$, which is a probability distribution. Let the string axis be the z-axis. Then the variable z is the ratio of the hadron $E + p_z$ to the total system $E + p_z$. The Lund fragmentation function is

$$f(z) \sim z^{-1}(1-z)^a \exp(-bm_T^2/z), \tag{2.40}$$

where a and b are parameters. As an example, if the parameter a is decreased, $f(z)$ will increase in value and the particle momentum distribution will be shifted to higher values.

This string model is implemented in the program JETSET [52]. Both the LEPTO and ARIADNE programs work within the framework of this model.

2.5.2 Cluster Hadronization

Cluster hadronization [53] is based on the notion of preconfinement of colour. This means that the generated partons tend to be clustered, in both coordinate and momentum space, into colour-singlets at the end of a parton shower branching process [54]. The model assumes that these are the

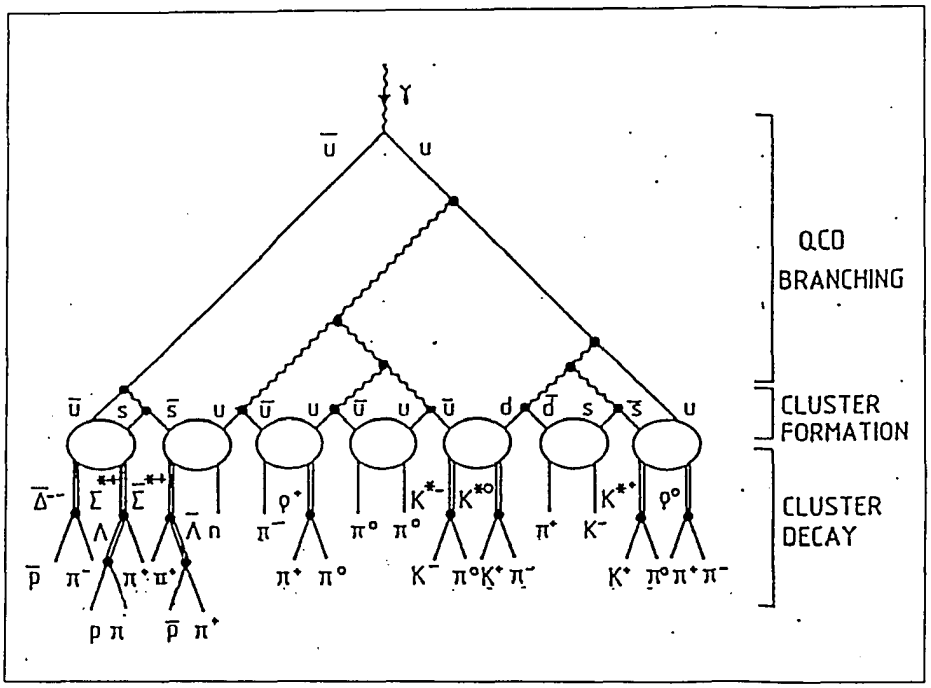

Figure 2.10: Schematic illustration of cluster fragmentation model used in HERWIG.

units that give rise to the hadrons.

Starting from the partonic configuration that was produced by the parton shower, any gluons are split into $q\bar{q}$ pairs and then all the quarks are combined into colourless clusters. This is shown schematically in Figure 2.10. These are characterized by a mass and flavour content. The cluster mass depends on the perturbative cutoff Q_0; for a value of 1 GeV, masses are typically on the order of a few GeV. The clusters are considered to be superpositions of resonances that are decayed into a pair of known hadrons. The decay is isotropic in the rest frame of the cluster. Any heavier clusters are first allowed to decay into two lighter clusters. The hadron momentum distribution is given by the parton showers and the phase space for the cluster decays. The hadronization in HERWIG is based on the cluster model.

2.6 Radiative Corrections

The electron-proton cross-section and the properties of the hadronic final state depend on the scattering variables x and Q^2. These variables are determined not only from the scattered electron

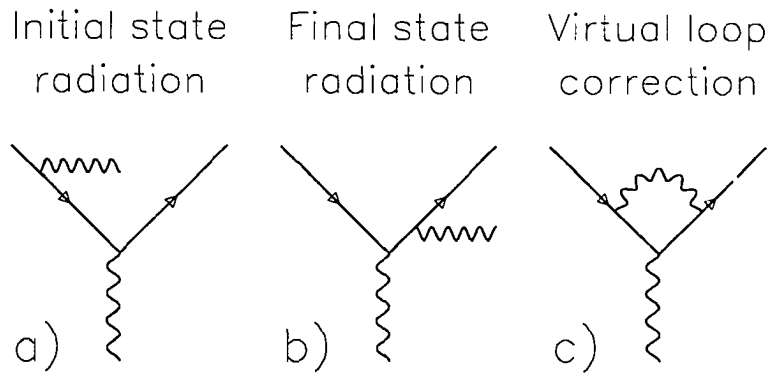

Figure 2.11: Feynman diagrams for some radiative corrections.

angle and energy but also from the initial electron and proton energies. The electrons, in particular, can lose energy through photon radiation before scattering off the proton. It is necessary to correct for such *radiative effects* in order not to misinterpret the scattering results. Radiative corrections include such processes as initial and final state photon radiation, virtual corrections, two-photon exchange, and photon and Z exchange. Some examples are shown in Figure 2.11.

First order electroweak radiative cross-sections are calculated in the program HERACLES [55] which is interfaced [56] to LEPTO as well as to ARIADNE. This program chain allows QCD showers and hadronization to be studied in radiative events. The ME, ME+PS, and CDM+BGF models and HERWIG were investigated without electroweak radiative corrections.

2.7 Proton Remnant

There is no clear theoretical prescription for dealing with the proton remnant and this leads to major differences between the predictions of the different models. In the LEPTO versions of the LUND string model, quark counting is used for the remnant treatment [57]. For scattering off a valence quark, the remnant is taken to be the resulting diquark. For a sea quark scatter, the remnant is split into either a baryon and a quark or a meson and a diquark. In the boson-gluon fusion process, the three valence quarks in the remnant are divided into a quark and a diquark.

Two approaches are available in HERWIG. One choice uses a soft underlying event based on

a phenomenological description of minimum bias events from the UA5 experiment [58]. This method splits the remnant into many soft clusters. The other technique allows the remnant to split into two clusters. Table 2.3 provides a summary of the different models.

Model Symbol	Model	Generator	Fragmentation	Radiative Corrections
ME	first order matrix elements	LEPTO	string	no
PS(W^2)	parton showers	LEPTO	string	yes
PS(Q^2)	parton showers	LEPTO	string	yes
PS(Q^2(1-x))	parton showers	LEPTO	string	yes
HERWIG	parton showers	HERWIG	cluster	no
HERWIG+SUE	parton showers with soft underlying event for the remnant	HERWIG	cluster	no
ME+PS	first order matrix elements with parton showers	LEPTO	string	no
CDM	colour dipole model	ARIADNE	string	yes
CDM+BGF	colour dipole model with first order matrix elements for boson-gluon fusion process	ARIADNE	string	no

Table 2.3: Summary of QCD models.

Chapter 3

The Experimental Setup

The data analyzed for this thesis was taken during the first running period of the HERA accelerator in the summer and fall of 1992, when neither HERA nor ZEUS was in full operation. *Data* will henceforth be used as a collective noun. The HERA operating conditions were not altered significantly during this time period. The ZEUS detector changed slightly; new components were read out and the trigger was modified. The data from the additional components was not used in the analysis presented in this thesis and all trigger changes were carefully checked. None of the modifications had any systematic effect on the data sample. The approach taken in this chapter is to describe the accelerator and detector setup that was used during the accumulation of over 90% of the data and, where relevant, to make mention of the final design capabilities. The trigger will also be detailed.

3.1 The HERA Accelerator

HERA (Hadron-Elektron Ring Anlage) is an electron-proton collider in operation at the Deutsches Elektronen Synchrotron (DESY) in Hamburg. It is the first such collider ever constructed. HERA consists of two independent accelerators, each 6.3 kilometers in circumference, that accelerate and store counter-rotating beams of electrons and protons. Collisions can occur at three of four interaction regions where the two beam vacuum pipes intersect. The layout of HERA is shown in Figure 3.1. At present, there are two experiments in operation: ZEUS, located at the South Hall, and H1, situated in the North Hall.

Particles are accelerated in HERA by passing through radiofrequency (RF) cavities. Bending dipoles are employed to constrain the particles to their orbits within the vacuum pipes. During acceleration, the magnetic field, B, of the dipoles must increase with the particle momentum according to

$$p = 0.3B\rho, \tag{3.1}$$

where ρ is the bending radius in meters, B is measured in Tesla, and p is the momentum of a particle of unit charge in GeV. Expression (3.1) shows that the magnetic field would have to vary over a large range if the particles were to be accelerated from rest to a high momentum. The RF

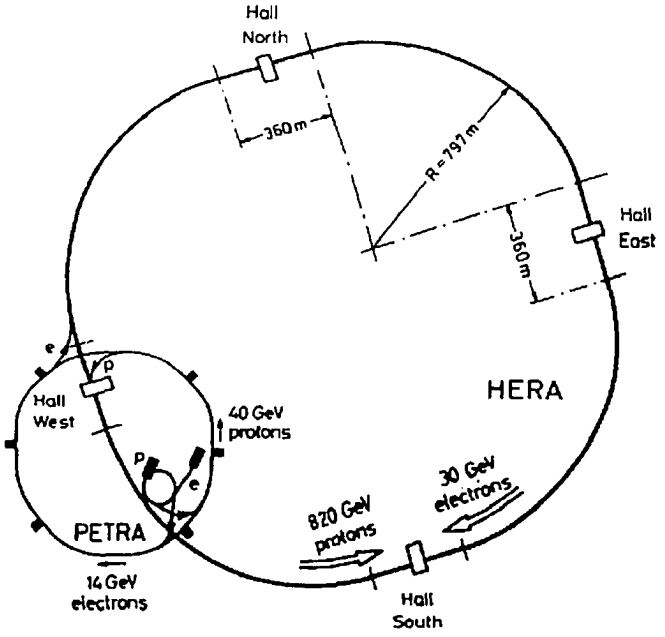

Figure 3.1: Layout of HERA.

would also be required to change over a large range since the particles have to be in phase with the RF wave in order to be continuously accelerated. This difficulty is overcome by using a preaccelerator complex.

Another reason for preaccelerators is related to the stability of the particle beams. Consider non-relativistic particles in a circular accelerator that are in phase with the rising edge of the accelerating RF wave. A particle that is moving slightly faster than the rest of the particles will be accelerated less the next time it passes through the cavity. Similarly, a slow particle will undergo greater acceleration. The result is that these particles will tend to form a stable bunch and they are said to be on a *phase stable point*. An RF *bucket* is a region in position and velocity phase space that is phase stable.

The opposite effect occurs for particles that are in phase with the falling edge of the wave and they are quickly lost. In the case of relativistic particles, which are all travelling at the same speed, higher momentum particles have a larger bending radius and therefore have a larger orbital period.

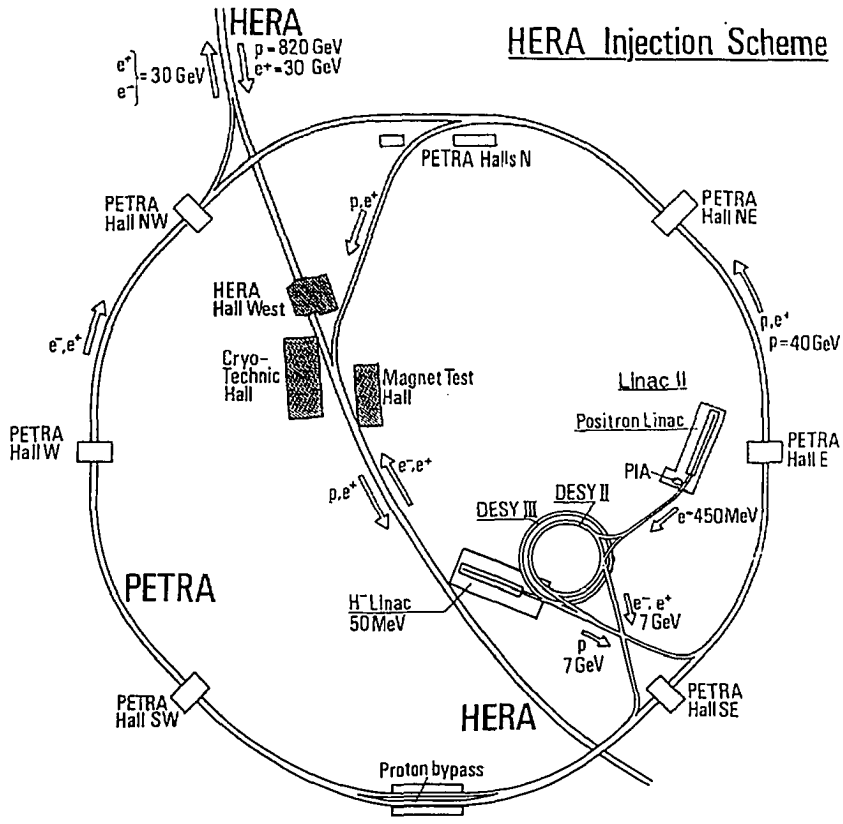

Figure 3.2: Layout of HERA preaccelerators.

The phase stable point is now on the falling edge of the RF wave. A series of preaccelerators, each optimized for a given energy range, allows the avoidance of a transition in the phase stable point during particle acceleration.

The HERA preaccelerators are shown in Figure 3.2. The electrons are obtained from a hot cathode. They are then accelerated by a 400 MeV electron/positron linear accelerator (LINAC II), accumulated in the storage ring PIA, accelerated to 7 GeV in the synchrotron DESY II, and transferred to PETRA II. When PETRA II has been filled, the electrons are accelerated to 14 GeV and injected into HERA where they are accelerated to the collision energy. The design value of the HERA electron beam is 30 GeV.

more accurate predictions. Although there are not convincing theoretical arguments for either choice of scale, they span the range of possibilities predicted by this model.

An intermediate scale can be chosen based on the limiting behaviour of the matrix elements at low and high x [31]. In the first order matrix elements, $\langle p_T^2 \rangle$ is approximately $Q^2(1-x)$ as

The protons are acquired by passing a 50 MeV beam of H- ions through an aluminum foil in the synchrotron DESY III. After being accelerated to 7.5 GeV, they are injected into PETRA II where they are accelerated to 40 GeV before injection into HERA. The protons are then accelerated to the design energy of 820 GeV. Superconducting magnets are required to keep protons of this energy on their orbit.

An important parameter of any collider is the number of collisions per unit time. This is characterized by the *luminosity*, $\mathcal{L}$. It is defined by

$$R = \mathcal{L} \cdot \sigma, \tag{3.2}$$

where R is the rate of occurrence of a process with a cross-section σ. HERA has been designed to provide a luminosity of 1.5×10^{31} cm^{-2}sec^{-1}, a value based on the requirement that there be an acceptable rate of electroweak interactions at momentum transfers greater than the characteristic mass of the weak interaction. Rough numbers are a hundred events per year at a Q^2 value greater than 150 GeV^2. This necessitates 210 bunches, each carried in one of 220 RF buckets. Such a spacing corresponds to 96 ns between adjacent bunches.

The data analysed in this thesis was taken when HERA operated with nine colliding electron and proton bunches spaced by 96 ns. The electron beam had an energy of 26.7 GeV and a total current of about 2 mA; the protons were at the design energy with a total current of about 1 mA. The luminosity was typically 3×10^{28} cm^{-2}sec^{-1}. In addition, one proton and one electron bunch, known as *pilot bunches*, were left unpaired to give estimates of beam related backgrounds. The proton bunch length was about 40 cm. The electron bunch length was only about 2 cm, due to a higher RF -cavity frequency, and can assumed to be pointlike.

Details on the design of HERA are in [59]. Status reports appear in most particle accelerator conference proceedings [60].

3.2 The ZEUS Interaction Region

The ZEUS detector and interaction region are shown in Figure 3.3. The ZEUS coordinate system is right-handed, with the incoming proton beam defining the direction of the positive **z** axis and the nominal interaction point defining **z**=0. All coordinates are labelled in boldface. The reference for the ZEUS detector is [61].

In addition to providing a common vacuum pipe for the colliding beams, the interaction region is designed to protect the detector from electron and proton beam induced backgrounds and

above. The evolution variable for initial state showers is given by

$$Q_i = E_i\sqrt{\xi_i}, \qquad \xi_i = (p \cdot q_i)/(E\omega_i), \tag{2.33}$$

where E is the energy of the parton p and ω_i that of q_i. The ordering is now

†. Herwig version 5.6 was used for the simulations presented in this thesis.

damaging synchrotron radiation. In order to achieve a zero beam crossing angle, it is necessary to bend the electron beam with quadrupoles by 10 mrad over 17.4 m near the interaction point. This bending is a strong source of synchrotron radiation. A series of tungsten absorbers and movable collimators has been installed to reduce the radiation since the photons contribute to the noise in the central tracking detector by converting to e^+e^- pairs.

The ZEUS beam pipe begins at +5.35 m with the forward collimator C3. A forward beam pipe piece connects C3 with the collimator C4, located at +2.3 m. This is followed by a central beampipe segment of length 3.5 m. The middle section of this segment near the interaction point (of length 1480 mm) is made of two thin concentric aluminum pipes surrounding a layer of corrugated aluminum. The innermost pipe has a wall thickness of 0.4 mm and the outermost pipe has a thickness of 0.25 mm. Cooling of this section is provided by blowing nitrogen through the corrugations. The third section of beam pipe is bounded by a beam position monitor and a collimator, C5, located at -3.2 m. The last section of the ZEUS beam pipe extends from C5 to -5.2 m and contains an adaptor piece to connect to the HERA vacuum chamber. With the exception of the thin central part, all sections are water cooled.

Just before the collimator C5, at -3.15 m, there are two pairs of scintillation counters: one above and one below the beam pipe. The counters are separated by 5 mm of lead. These C5 counters measure the timing and longitudinal spread of both the proton and electron bunches. The timing resolution is about 0.5 ns. The signals are derived from the beam halos which comprise off-orbit particles and the products of beam particle collisions with gas molecules and the beampipe. The C5 signals can also be used for rejection of backgrounds from proton interactions in the C5 collimator.

Protection from the proton beam halo and upstream proton beam-gas interactions is provided by the veto wall detector, located at -7.3 m. It consists of an 87 cm thick iron wall with a 95 cm x 95 cm hole for the beam pipe and magnets. The iron is sandwiched between two scintillator hodoscopes which can be used to veto beam-gas interactions.

3.3 The ZEUS Magnet System

The magnet system, [62] and [63], provides the magnetic field used for measuring the momenta of charged particles. The main component is a superconducting solenoid which surrounds the interaction region. (It encircles the components labelled CTD and VXD in Figure 3.3.) The solenoid is 2.46 m long with inner and outer diameters of 1.85 m and 1.91 m,

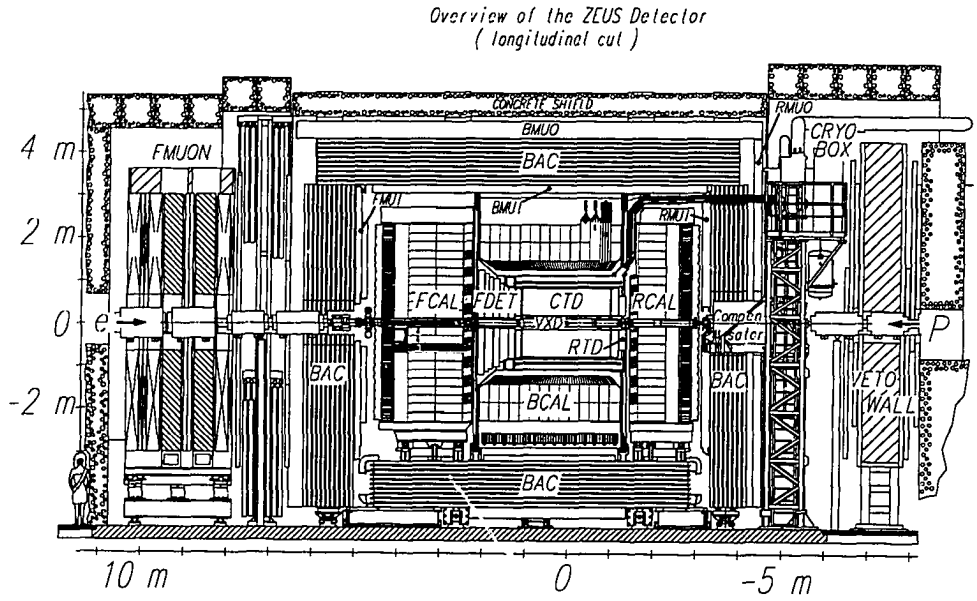

Figure 3.3: Cross-section of the ZEUS detector parallel to the beam axis.

respectively. The cable has a superconducting insert of niobium-titanium and copper filaments that were extruded with aluminum. It was designed to keep the radiation length thickness of the coil below 0.9 radiation lengths. The solenoid is installed in a cryostat which provides cooling with liquid and gaseous helium. It can produce an axial magnetic field of 1.8 T with a current of 5 kA. During the run period, the current was 3950 A which produced a field of 1.43 T.

An iron yoke surrounds the main body of the detector and serves to return the flux of the solenoid. Normal conducting coils surround the yoke and are used to magnetize the iron with a toroidal field of 1.6 T. This field allows a muon momentum measurement by the muon chambers that are on either side of the yoke.

The solenoidal field was measured with a precision better than 0.2% in the central region. The

measured values were within 1% of the values predicted by the program package TOSCA [64].

3.4 The ZEUS Detector

The ZEUS detector is a composition of many complex subdetectors, or components. Not all of these were fully operational or instrumented during the run period. A general description of the entire detector is given, but there is a considerable emphasis on the two components used in the analysis of Chapter 6: the calorimeter and the central tracking detector. Elements of the readout and trigger systems are also described, as well as the software used for detector simulation and data reconstruction.

3.4.1 Particle Energy Losses in Matter

Particle detectors exploit the energy loss mechanisms of particles passing through matter [65], [66]. Consider first matter that is not very dense, e.g. a gas. For charged particles heavier than electrons, the most important losses are due to Coulomb interactions with atomic electrons. These interactions produce electron-ion pairs, but have a negligible effect on the trajectory of the incident particle. The electrons have a range of only a few microns, but can liberate several secondary electrons. These can subsequently be collected to provide a detector signal.

The energy loss per unit length of an ionizing particle is given by the Bethe-Bloch equation:

$$-\frac{dE}{dx} = 2\pi N_A r_e^2 m_e c^2 \rho \frac{Z}{A}\frac{z^2}{\beta^2}\left[ln\left(\frac{2m_e\gamma^2}{I^2}\beta^2 c^2 W_{max}\right) - 2\beta^2\right], \tag{3.3}$$

where

m_e is the electron mass, $m_e = 0.5110$ MeV,

N_A is Avogadro's Number, $N_A = 6.022\times10^{23}$ mol,

r_e is the classical electron radius, $r_e = e^2/(m_e c^2) = 2.817\times10^{-13}$ cm,

ρ is the density of the absorbing material,

Z and A are the atomic number and atomic weight of the absorbing material,

z is the charge of the incident particle (in units of e),

$\beta = \frac{v}{c}$ of the incident particle, $\gamma = 1/\sqrt{1-\beta^2}$,

I is the mean ionization potential, and

W_{max} is the maximum energy transfer allowed in a single collision.

Due to the $1/\beta^2$ factor, the energy loss decreases with increasing speed until the value of β is about 0.96, after which dE/dx starts to increase slowly and then eventually levels off. In the region of minimum ionization, dE/dx has a value of approximately -2 MeV/g cm^2, which is almost the same for all particles of the same charge. A minimum ionizing particle, or a *mip*, will lose about 2 keV/cm in air and about 40 MeV/cm in uranium. Typically, particles with energy greater than about 1 GeV are minimum ionizing. The energy loss does not depend upon the mass of the incident particle for energies below the minimum ionizing value. Different particles of the same momentum can be distinguished, therefore, by a measurement of dE/dx.

The strong interaction becomes important in dense materials for both neutral and charged hadrons. A beam of hadrons with initial intensity $I(0)$ passing through a target material will be exponentially attenuated due to strong interactions according to

$$I(x) = I(0)\,exp\,(-x/\lambda)\,. \tag{3.4}$$

The absorption, or interaction, length, λ, of a target with density ρ and atomic weight A is given by

$$\lambda = \frac{A}{N_A \rho \sigma_{abs}}. \tag{3.5}$$

The absorption cross-section, σ_{abs}, is approximately independent of momentum above 20 GeV [65]. For neutrons and protons, σ_{abs} is roughly proportional to $A^{0.7}$, thus giving

$$\lambda \approx 35\frac{A^{1/3}}{\rho}. \tag{3.6}$$

The exponential dependence upon the density of the target can be seen from equations (3.4) and (3.6). For example, λ for uranium is about 10 cm, whereas for air it is about 700 cm. These interactions can be neglected, therefore, when considering the passage of hadrons through gaseous detectors.

Electrons and positrons also lose energy by ionization in the same way as heavier particles. Their small mass means that there can be significant deviations from their original trajectories, so that the Bethe-Bloch equation must be modified slightly. This effect, however, is not important for gasses. More significantly, electrons and positrons can radiate Bremsstrahlung by scattering in the electric field of nuclei. The cross-section for emission of a photon of energy k by a particle of charge z, mass M, and velocity v is

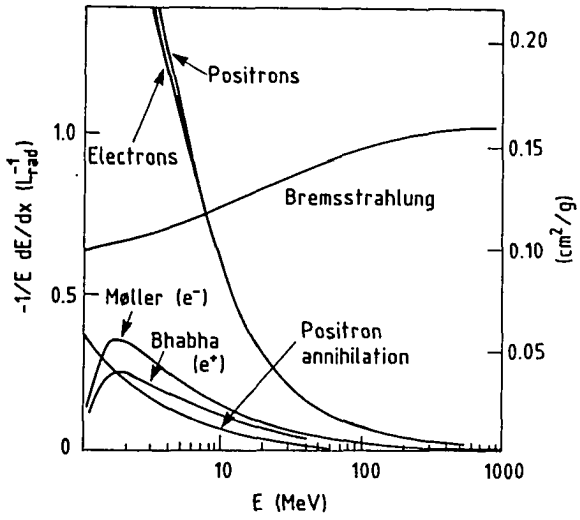

Figure 3.4: Fractional energy loss per radiation length (left ordinate) and per g/cm^2 (right ordinate) in lead as a function of electron or positron energy. The critical energy for lead is approximately 10 MeV. (Figure from [67].)

$$\frac{d\sigma}{dk} \cong 5\alpha z^4 Z^2 \left(\frac{m_e c}{Mv}\right)^2 \frac{r_e^2}{k} ln \frac{Mv^2\gamma^2}{k}. \tag{3.7}$$

Since this cross-section depends inversely on the square of the mass of the incident particle, energy loss due to radiation is far more significant for electrons and positrons than for heavier particles. The mass of the next lightest particle, the muon, is about 200 times that of the electron. Furthermore, the Z dependence means that Bremsstrahlung losses are much more important for heavy elements.

The energy at which losses due to radiation equal losses due to ionization is called the critical energy, ε_c. Its value in MeV can be approximated by

$$\varepsilon_c \approx \frac{800}{Z}, \tag{3.8}$$

which is on the order of 9 MeV for uranium and 100 MeV for air. Since the ionization loss varies logarithmically with energy, whereas the radiation loss varies almost linearly with energy, electrons will lose most of their energy through radiation above ε_c. This is shown in Figure 3.4 in

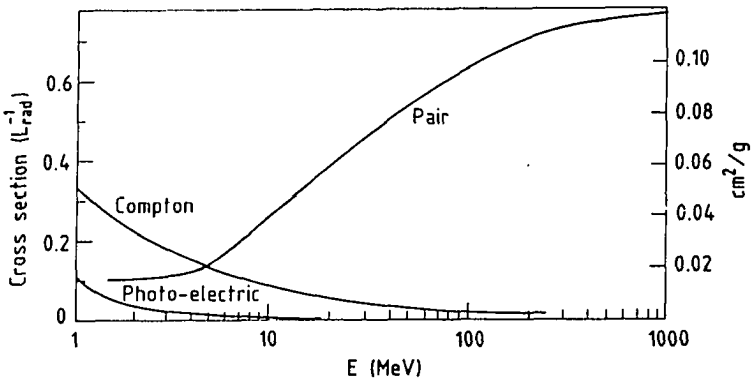

Figure 3.5: Photon cross-section in lead as a function of photon energy. (Figure from [68].)

which the fractional energy loss in lead is plotted as a function of electron or positron energy.

For photons, the three most significant interactions are the photoelectric effect, Compton scattering, and pair production. The relative contributions of these processes as a function of the photon energy are shown in Figure 3.5. For low energy photons, E < 500 keV, the photoelectric effect dominates. The cross-section has a strong Z dependence; for photons with an energy of a few MeV, it goes as Z to the fifth power. For energies above 50 MeV, photons generally undergo pair production into an electron-positron pair. Compton scattering from atomic electrons is important for intermediate energies.

3.4.2 Tracking

For certain types of physics data analysis, information on particle trajectories is necessary. It is acquired from tracking detectors whose function is based upon the collection of ionization electrons produced in gases by passing charged particles. The spatial locations of tracking detector interactions are assigned by algorithms to trajectories in a procedure known as *tracking*. The

ZEUS tracking detectors, which belong to a class of detectors known as drift chambers, are the closest components to the interaction point.

The basic principles are the same for all drift chambers. A constant electric field, known as a drift field, is set up between anode and cathode field wires. This field controls the velocity and direction of electron drift. In a simplified one dimensional example, a single anode wire bounded on each side by cathode wires defines a drift cell. Ionization electrons liberated in the cell are collected on the anode wire. For this reason, anode wires are referred to as *sense wires*. Shaper wires can also be used to improve the uniformity of the field between anode wires. Given the drift velocity and a reference time, spatial information is obtained by measuring the drift time of the electrons. A measurement of $\frac{dE}{dx}$ is possible if the pulse height of the signal is also recorded. This allows particle identification if the momentum is calculated by measuring the curvature in a magnetic field.

Of the tracking detectors described below, only information from the central tracking detector and the vertex detector was used for the data analysis presented in this thesis.

3.4.2.1 The Vertex Detector

The main purpose of the vertex detector (VXD) [69] is the detection of short lived particles and, as such, it is the closest component to the interaction region. It is a cylindrical drift chamber of active length 1.6 m. The inner cylinder is 1.2 mm thick and has a radius of 9.9 cm. The outer cylinder has a radius of 15.9 cm and a thickness of 0.72 mm. The cylinders and end flanges are made of carbon-fiber to reduce multiple scattering.

The chamber has a total of 120 drift cells formed by 12 layers of sense wires 3 mm apart. The maximum drift space is 3.6 mm which corresponds to a maximum drift time of about 700 ns with dimethyl-ether as the working gas. The spatial resolution is roughly 35 μm in the central drift space region. The precision of the measurement of the distance of closest approach to the interaction vertex is increased by a factor of three when the VXD information is combined with that of the central tracking detector.

3.4.2.2 The Central Tracking Detector

The central tracking detector (CTD) [70] is a cylindrical drift chamber that surrounds the beam pipe. It is active between inner and outer radii of 19.0 cm and 78.5 cm, respectively, and over a length of 202 cm. It can be used to reconstruct tracks in the polar angular range

$15^{\circ} < \theta < 164^{\circ}$ and also provides $\frac{dE}{dx}$ information.

The endplates are 20 mm thick aluminum with 3 mm diameter holes for the wires. They are supported by inner and outer cylinders which also serve to form a closed gas volume. The inner cylinder is constructed of 2 aluminum skins, 0.7 mm thick, with a 9 mm gap filled with structural foam. The outer cylinder is made of 6 mm thick aluminum. This construction minimizes the cylinders' thickness while providing enough structural support for the wire load. The inner surfaces of the cylinders are coated with Cu/kapton/foam which serves as an electrostatic shield.

The wires are organized into nine concentric radial *superlayers* each with eight layers of sense wires. The wire layout in a 45° sector normal to the beampipe is shown in Figure 3.6. In the figure, the sense wires are indicated by the solid dots. Shaper wires, held at 0 V, separate the sense wires and also provide shielding between the superlayers. The electric drift field is provided by planes of nineteen cathode wires. The sense wires have a 30 μm diameter and are fabricated from gold-plated tungsten which was chosen for its signal propagation properties. The cathode and shaper wires are made of copper-beryllium with diameters varying from 70-300 μm. All the wires are strung through individual feedthroughs made of a copper-brass composite that is surrounded by an insulator. There are a total of 24,192 wires, of which 4608 are sense wires.

If a signal is recorded by a sense wire, there is no way of knowing on which side of the wire the ionizing particle has passed. This *left-right ambiguity* can be resolved by orienting the planes of wires at 45° to a radial line from the chamber axis, as can be seen in the figure. This has the advantage that a particle emerging from the interaction region will cross a plane of sense wires, thereby allowing left-right ambiguities to be resolved within a single superlayer. Furthermore, tracks that are out-of-time by one crossing are discontinuous and can be rejected. These features permit reconstruction of close tracks caused by the passage of a jet of particles.

Since the chamber is operated in a magnetic field, the liberated electrons do not drift along the electric field lines. The CTD has been designed so that the angle between the electron trajectories with and without the magnetic field is 45°. This is known as the Lorentz angle. Because the sense wire planes are also rotated by 45°, liberated electrons drift with trajectories tangent to the chamber azimuth at the cell centre. This eliminates inactive regions in the drift cells.

Superlayers 1, 3, 5, 7, and 9 have their wires strung parallel to the chamber axis. The interleaved superlayers, 2, 4, 6, and 8, have their wires at stereo angles of approximately $\pm 5^{\circ}$, which enables an accurate reconstruction of the z-coordinate of tracks. The stereo angle is chosen to give roughly equal angular resolution in the polar and azimuthal angles. The resolution in

radians for a track at a 45° polar angle is about $0.0005 + 0.002/p$, where the terms are to be added in quadrature and p is the particle momentum in GeV.

Each of the sense wires is connected at one end to a preamplifier which drives a cable leading to a 100 MHz FADC system. All of the sense wires in the first axial superlayer and four of the wires in the second and third axial superlayers are read out at both ends. The signals are used as

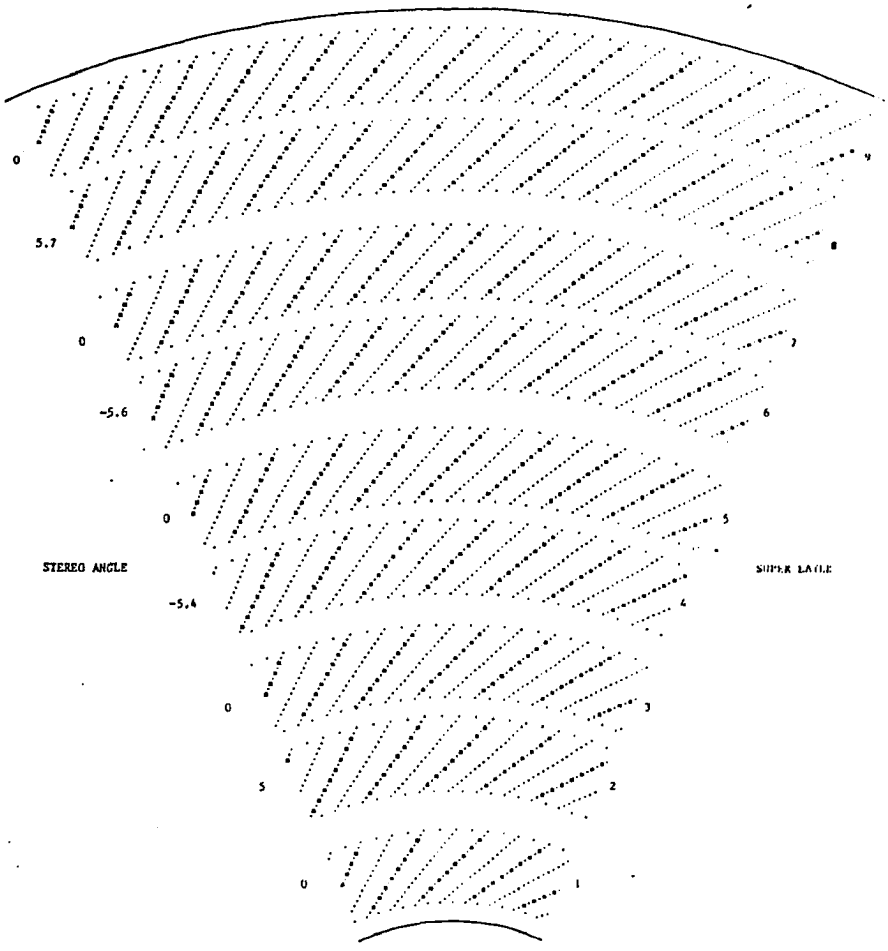

Figure 3.6: CTD wire layout in a 45^{0} sector orthogonal to the z-axis. The sense wires are indicated by solid dots.

input to a z-by-timing readout system, which will be discussed in more detail below.

During the run period, the gas was a mixture of argon (88.22%), carbon dioxide (9.22%), and ethane (1.69%) that was bubbled through ethanol (0.88%). Argon has the advantage of a high specific ionization and low cost. However, it de-excites through the emission of 11.5 eV photons which can ionize the cathode, thereby causing permanent discharge. The carbon dioxide and ethane *quench* the discharges through the absorption of the photons. The energy is dissipated as heat or through dissociation. Polymerization of the dissociation products on the chamber wires is prevented by the ethanol. The drift field was 1.2 kV/cm. These conditions resulted in a Lorentz angle of 39.1° and a nominal drift velocity of 48.7 μm/ns [71]. Furthermore, only the three inner axial layers were instrumented with the z-by-timing readout. The hit resolutions were measured to be σ_z = 4.5 cm and $\sigma_{r\phi}$ = 940 μm.

3.4.2.3 Forward and Rear Tracking Detectors

The forward tracking detector (FTD) will allow tracking in the forward region $7.5^\circ < \theta < 28^\circ$. It is made of three planar drift chambers, separated by 210 mm gaps, that are positioned perpendicular to the beam. Each chamber has three layers of drift cells with wire orientations of 0°, +120°, and -120° with respect to the x-axis. The rear tracking detector (RTD) comprises only one chamber which covers the angular range $160^\circ < \theta < 170^\circ$.

Interleaved between the FTD chambers is the transition radiation detector (TRD). A charged particle emits transition radiation when it crosses the interface between media with different dielectric properties. Since the total energy emitted is linearly proportional to the γ value of the particle, the TRD can enhance electron identification. It is made of radiator planes, comprising 70 mm of polypropylene, followed by tracking planes which detect the transition radiation. There are two radiators in each gap between the FTD chambers.

3.4.3 Calorimetry

Tracking detectors cannot be used as energy measuring devices for neutral particles or very high energy charged particles. Instead, calorimeters are employed. The purpose of these detectors is to generate a measurable signal that is proportional to an incident particle's energy. This can be realized only if the calorimeter absorbs all of the particle's energy and if the fraction of the energy loss that yields the signal is independent of the initial energy.

Since the rate of ionization energy loss in an absorber material increases with Z and the

nuclear absorption cross-section increases with A, calorimeters are constructed out of dense absorbers to avoid excessive size. A calorimeter is called *homogeneous* if the function of signal generation is simultaneously performed by the absorber. A common example is a lead-glass calorimeter. Alternatively, a separate active material can be used in a construction comprising alternating layers of absorber and active material. This type of calorimeter is referred to as a *sampling* calorimeter as the active material "samples" the signal after each absorber layer. Typically, iron, lead, or uranium is used as an absorber in conjunction with plastic scintillator or liquid argon as the active material. The ZEUS calorimeter, which is made of layers of uranium and plastic scintillator, is of the sampling type.

When a particle enters a calorimeter, interactions with the absorber create secondary particles, thereby giving rise to a *shower*. One of two types of shower can be initiated depending on the primary particle: electromagnetic or hadronic. Generally, hadronic showers will also contain an electromagnetic component.

3.4.3.1 Electromagnetic Showers

Consider an energetic electron (or positron) that impinges upon a calorimeter. Figure 3.4 shows that electrons of energy greater than 100 MeV lose their energy almost entirely through Bremsstrahlung. The most probable interaction for these high energy Bremsstrahlung photons is the pair production of electrons and positrons, as illustrated in Figure 3.5. These, in turn, will radiate more photons. In this manner, a single energetic electron or photon can give rise to an electromagnetic shower. The shower will continue to develop until the particle energies reach ε_c. Ionization and excitation become the dominant energy loss mechanisms for electrons below this energy, while photons lose their energy through Compton scattering. At still lower energies, positron annihilation and the photoelectric effect dominate.

The longitudinal dimension of electromagnetic showers can be characterized in a material independent way by the radiation length, X_0, of the material if the incident particle energies are greater than 1 GeV. A radiation length is defined as the mean distance over which a particle has its energy reduced by a factor 1/e (~63%) by radiation. An approximate expression is given by

$$X_0 \approx 180A/Z^2\,(g/cm^2)\,, \tag{3.9}$$

which is accurate to better than 20%. For uranium, X_0 is about 0.3 cm. Approximately 98% of the shower energy from an incident particle of energy E_0 is contained on average within $17.5 + \ln E_0$

radiation lengths, where E_0 is measured in GeV. This is about 18-23 X_0 for energies in the range 2 - 300 GeV. The energy deposition rate reaches a maximum at about $4 + \ln E_0$ radiation lengths.

Up to the shower maximum, 90% of the shower is laterally contained within a circle of radius 1 X_0 [65]. After this point, the transverse development of electromagnetic showers is primarily due to multiple Coulomb scattering. It is characterized by the Moliere radius, ρ_M, that is given by the relation

$$\rho_M \approx 7A/Z\,(g/cm^2)\,. \tag{3.10}$$

Roughly 95% of the shower is contained laterally within a circle of radius $2\rho_M$, which is approximately 2 cm for uranium.

ZEUS has chosen an organic scintillator to transform the shower energy into a measurable signal. A scintillator is a material that produces a flash of light after the passage of a charged particle. Their utility lies in their linear sensitivity to incident energies. If scintillators are coupled to photomultipliers, the scintillations can be converted into an electrical signal.

In an aromatic scintillator, ionization energy excites the free valence electrons of the molecules. Most of the total light output comes from a two stage de-excitation. The first stage, referred to as internal degradation, is the non-radiative decay to the lowest excited state. It is very fast, on the order of picoseconds. The second stage occurs within a few nanoseconds and is the decay to one of the excited vibrational ground states. The scintillator is transparent to its own radiation because the emitted photons are not energetic enough to excite ground state molecules to the first excited state.

3.4.3.2 Hadronic Showers

The development of showers initiated by hadrons is more complex than that of electromagnetic showers [72]. Charged hadrons lose energy through ionization, but all hadrons can interact inelastically with the nuclei of the absorber material. If the incoming hadron energy is above approximately 50 MeV, a nuclear interaction will induce a spallation process [73]. In the first of two stages of spallation, the incoming particle collides with individual nucleons and usually escapes with part of its original kinetic energy. The struck nucleons, in turn, may collide with other nucleons, thus creating an intranuclear cascade. Some of the collisions may result in the creation of resonant states that decay through the production of mesons. Nucleons or mesons with energies greater than about 10 MeV can overcome the nuclear binding energy and escape from the

nucleus. Otherwise, they share their energy with a few other nucleons. The ratio of protons to neutrons produced is approximately equal to their relative fraction in the nucleus. The second stage involves the de-excitation of the resulting intermediate nucleus. This proceeds through the evaporation of secondary hadrons. These are mainly neutrons because charged particles have to overcome the Coulomb barrier of the excited nucleus. Once the excitation energy is less than the nucleon binding energy, photons are emitted. Heavy intermediate nuclei can also de-excite through fission, which is followed by nucleon evaporation from the excited fission fragments.

The relatively high energy secondary hadrons released in the first stage of the spallation reaction can initiate further spallations, thus giving rise to an hadronic shower. Two further processes can occur if ^{238}U is the absorber material. The evaporation neutrons can induce secondary fissions in ^{238}U nuclei. This is because they have a mean kinetic energy of 2 MeV and the fission threshold is 1.2 MeV. The second process is neutron capture by ^{238}U, leading to delayed gamma ray emission. The hadrons produced in the second spallation stage have energies of a few MeV. As such, the charged secondaries do not usually reach the active layers and remain undetected. Moreover, many of the hadrons eventually decay to neutrinos and muons which can escape from the detector.

An electromagnetic component to the hadronic shower is produced by mesons that interact electromagnetically before experiencing nuclear interactions. These are primarily neutral pions which decay according to $\pi^{\circ} \rightarrow \gamma\gamma$. The fraction of the incident hadron energy that contributes to the electromagnetic component, f_{em}, fluctuates in a non-Gaussian manner from event to event as it depends strongly on the detailed interactions occurring early in the shower. The mean fraction, $\langle f_{em} \rangle$, increases logarithmically with the incident particle energy up to several hundred GeV.

The hadronic shower dimensions are characterized by the nuclear interaction length, λ, given by Equation (3.5). Approximately 95% of the shower energy is contained within a cylinder with a length of $0.2\ln E_0 + 2.5E_0^{0.13} + 0.7$ interaction lengths [74] and radius of 1λ. A comparison of equations (3.5) and (3.9) shows that λ is much larger than X_0 for high Z materials, a fact which can be exploited for particle identification. In the case of uranium, which has a λ/X_0 ratio greater than thirty, 80 cm are required to contain a 300 GeV charged pion but only 10 cm to contain an electron of the same energy.

3.4.3.3 Energy Resolution and Compensation

In a conventional calorimeter such as lead-liquid argon or lead-scintillator, the signal

distribution from a beam of monoenergetic charged pions will have a larger root mean square and a lower mean than the signal from a beam of electrons of equal energy. The lower mean is attributable principally to the nuclear binding energy losses during the spallation reactions. For instance, for a 5 GeV proton, Monte Carlo calculations indicate that, on average, these losses account for 40% of the energy dissipated in non-electromagnetic form in a high Z material like uranium [75]. The fluctuations about this mean contribute to the signal width and may be as large as 35%. The losses due to nuclear binding energy mean that the response to the non-electromagnetic component, h, of an hadronic shower is generally less than the response to the electromagnetic component, e. Therefore, fluctuations in f_{em} will further degrade the resolution.

There are two additional consequences of the fact that e/h does not equal unity. First, the energy resolution, defined as $\frac{\sigma(E)}{E}$, does not improve as $E^{1/2}$ but approaches a constant. This was observed by the CDHS collaboration, which found no improvement in energy resolution beyond 100 GeV [76]. Second, the calorimeter signal is not proportional to the incident hadron energy because f_{em} is energy dependent; it increases with the logarithm of the incident energy. For the CDHS calorimeter, which has an e/h ratio of about 1.3 at 100 GeV, the calorimeter signal per GeV would be about 10% higher than that measured at 10 GeV.

The optimum solution is to construct a *compensating* calorimeter, i.e. one which has an e/h ratio of unity. This is achievable by selectively augmenting the calorimeter response to the non-electromagnetic component. It is, however, necessary to utilize a mechanism that is correlated to the binding energy losses if the resolution is to be improved. Since the total amount of kinetic energy carried by neutrons in a given event is related to the binding energy loss, increasing the calorimeter response to neutrons will increase the value of h in a manner that improves the overall resolution.

One of the most important energy loss mechanisms for low energy neutrons in a hydrogenous active material is elastic collisions with free protons. Consider a calorimeter made of 3 mm uranium and 3 mm scintillator plates. A 2 MeV neutron will lose about 60% of its energy through scattering with protons in the scintillator, whereas a minimum ionizing particle will lose only approximately 10% of its energy through ionization. The recoil protons from the neutron scattering are densely ionizing and have a range that is generally less than the thickness of a scintillator plate. They, therefore, lose almost all of their energy in the active material. This implies that the e/h ratio can be tuned by adjusting the relative thickness of active and absorber materials. If 6 mm scintillator plates were used instead of 3 mm plates, the minimum ionizing

particle signal would double. The neutron energy loss obviously cannot double, but would increase to about 70%. Therefore, by decreasing the thickness of the scintillator plates, the relative contribution of the neutrons to the hadron signal can be enhanced. The enhancement is not as high as the above example would suggest, as the signal from the recoil protons can saturate.

A second way of tuning the value of *e/h* is possible if uranium is used as the absorber since low energy neutrons can induce fission in ^{238}U. A 2 MeV neutron that induces ^{238}U fission creates, on average, 7.4 MeV in gamma rays and 2.5 neutrons of about the same energy. The photons will create electron-positron pairs while the neutrons can induce further fissions†. The fission neutrons subsequently can contribute to the total signal through elastic proton scattering in the scintillator. Utilizing this phenomenon also requires consideration of the scintillator plate thickness as neutron scattering in hydrogenous material can slow them down below the fission threshold of ^{238}U.

Both of these techniques increase the response to the hadronic shower component. The use of a high Z absorber in combination with a low Z active layer also serves to decrease the response to electromagnetic showers. This is because low energy photons will preferentially lose their energy in the absorber due to the photoelectric effect.

3.4.3.4 The Calorimeter

The calorimeter (CAL) is constructed of stainless steel clad plates of depleted uranium†† (DU) interleaved with scintillator tiles. It has three main mechanical parts as shown in Figure 3.3: the forward calorimeter (FCAL) extending from $\theta = 2.2^{\circ}$ to 39.9°, the barrel calorimeter (BCAL) covering from $\theta = 36.7^{\circ}$ to 129.1°, and the rear calorimeter (RCAL) covering from $\theta = 128.1^{\circ}$ to 176.5°. The solid angle coverage is 99.7%. Each part is constructed of modules. The FCAL and RCAL each have 24 modules which are typically 4.6 m high and 20 cm wide, with a depth of 70 cm in the RCAL and 152 cm in the FCAL. A characteristic FCAL module is shown in Figure 3.7. There are 32 BCAL modules each of length 3.2 m. They have the form of a trapezoidal section between 24 and 45 cm, as shown in Figure 3.8

The scintillator tiles form a total of 5918 cells, each of which is read out on two sides. The readout arrangement can be seen in Figures 3.7 and 3.9. Longitudinally, the inner 25 X_0, or 1λ,

---

†. This method gave rise to the term *compensation* as the fission energy released compensates for the binding energy.

††. Depleted uranium has the composition: 98.1% U^{238}, 1.7% Nb, 0.2% U^{235}.

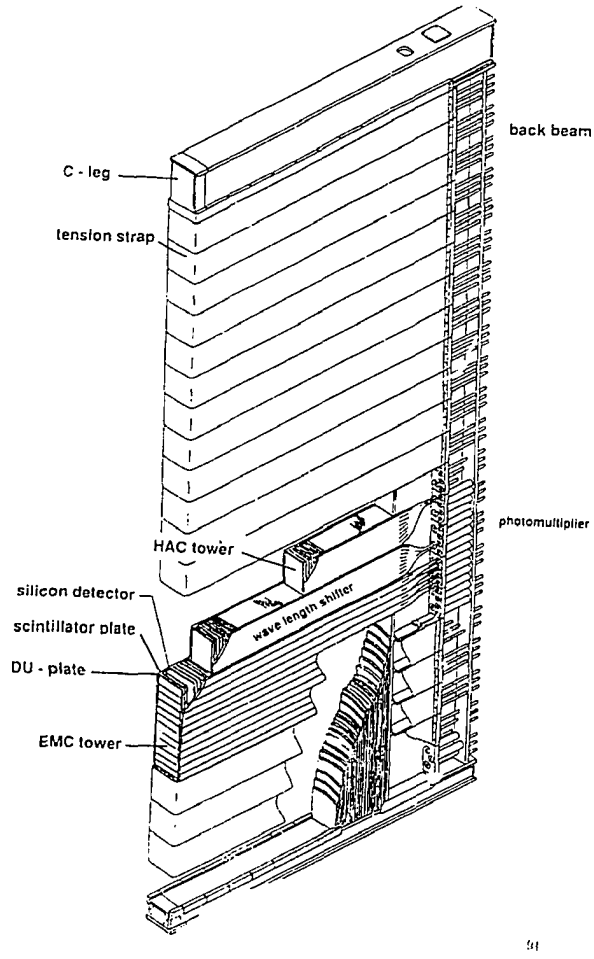

Figure 3.7: Typical FCAL module.

of the modules are read out as one section and form the electromagnetic calorimeter (EMC). The remaining part of the modules forms the hadronic calorimeter (HAC). The transverse sizes of the readout cells are typically 5 cm x 20 cm in the EMC sections of FCAL and BCAL and 10 cm x 20 cm in the RCAL. The HAC section cells are typically 20 cm x 20 cm. It is approximately 6λ deep in the FCAL, 4λ in the BCAL, and 3λ in the RCAL. The varying depth is dictated by HERA kinematics: most of the events have a large boost in the forward direction from the hadronic center

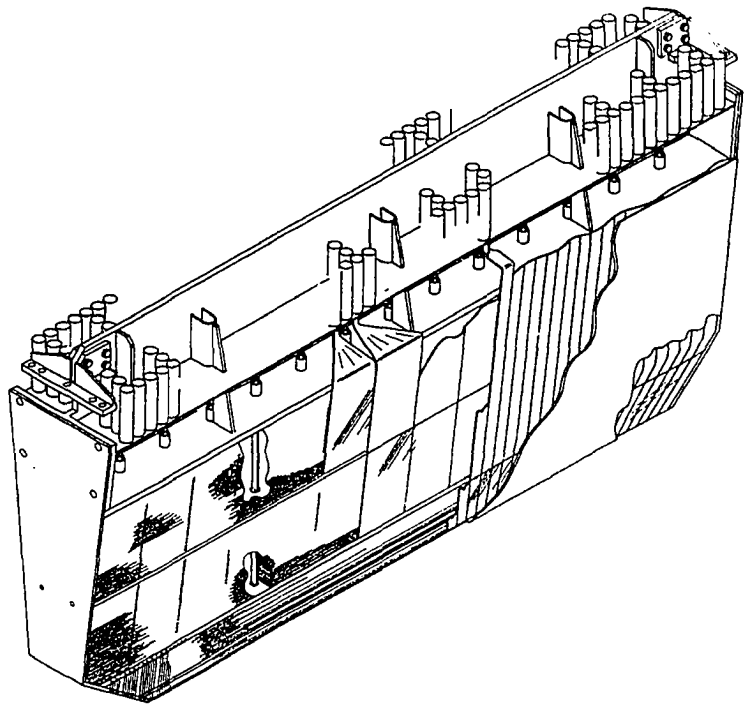

Figure 3.8: A BCAL module.

of mass frame. The HAC is readout as two sections, HAC1 and HAC2, in the FCAL and BCAL, and as one section in the RCAL, RHAC. The modules are divided into 20 x 20 cm^2 *towers*. An FCAL tower comprises four EMC cells, one HAC1 cell, and one HAC2 cell. An RCAL tower comprises two EMC cells and one HAC cell.

The depleted uranium plate thickness is 3.3 mm, which corresponds to 1 X_0. The plastic scintillator has a thickness of 2.6 mm. These values were obtained empirically from ZEUS test beam work and the experience of the HELIOS collaboration [77], [78], [79], [80] and give an e/h ratio of 1.00 ± 0.05. Stainless steel foil is wrapped around the DU plates for handling safety. The steel thickness also serves to adjust the signal from the DU natural radioactivity.

The scintillator is SCSN-38. This is polystyrene doped with the wavelength shifting dyes, butyl-PBD (1%) and BDB (0.02%) [81]. The fluor b-PBD absorbs the scintillation light from the

polystyrene base. It has an absorption peak of about 300 nm and emits 360 nm light at its emission peak. The emission peak matches the absorption peak of the BDB which subsequently emits the light at about 425 nm. It is desirable to increase the wavelength of the emitted light since this increases the attenuation length and the spectral transmittance of the scintillator. SCSN-38 has an attenuation length of about 70 cm and a decay constant of about 2 ns.

Each tile is covered with a layer of reflective wrapping to minimize light losses. It has a black correction pattern printed on it that improves the uniformity of the light response to 2% across the surface of the tile. The paper also protects the scintillator against mechanical damage.

The optical readout system is shown in Figure 3.9. An electrical signal is derived by directing light onto the surface of a photomultiplier tube (PMT). The light from the scintillator tiles of a readout cell is collected on both sides of the modules by 2 mm sheets polymethyl methacrylate (PMMA). Since a given flux of light per unit cross-sectional area entering a light guide cannot be increased, it is very inefficient to collect light from a large cross-sectional area and direct it onto a single PMT. The problem is avoided by doping the light guide with a wavelength-shifting flourescent dye. This allows the light from all of the scintillator tiles in a given section to be collected and directed onto a single PMT. (The alternative solution is to use a separate PMT for every scintillator tile which is impractical for large detectors). The dye, Y7, has an absorption spectrum that overlaps the SCSN-38 emission spectrum. It absorbs the light and re-emits it

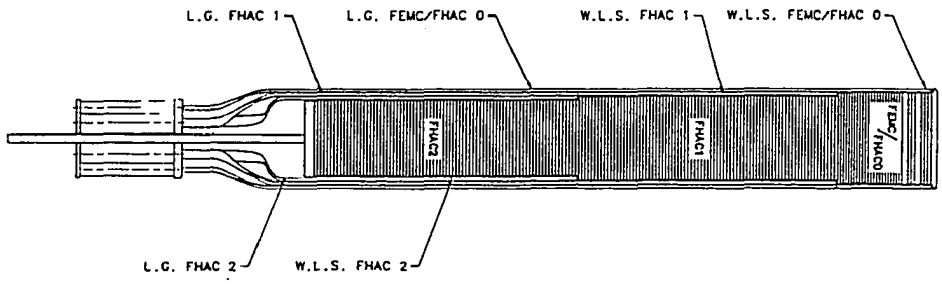

Figure 3.9: Light readout arrangement for a typical FCAL module.

isotropically at a longer wavelength, about 490 nm. The isotropic emission permits the light to be transported around the right angle formed by the scintillator tiles and the light guide. Apart from the surface facing the scintillator tiles, the PMMA is wrapped in a reflecting material. The light propagates by internal reflections along the bars to light guides, which direct the light onto the cathodes of PMTs mounted on the back of the modules.

Particles that directly traverse the wavelength shifting material will cause Cherenkov light to be emitted. This can contribute to non-uniformities because the light is shifted by the flourescent dye and cannot be distinguished from light originating in the scintillator. Ideally, the ratio of light yield to energy loss in the wavelength shifting material should be the same as the corresponding ratio in the calorimeter. This can be partially achieved by adding an ultra-violet absorbant that cuts off wavelengths below 360 nm, since SCSN-38 emits very little light below this wavelength. Non-uniformities caused by the different length light guide bars can be reduced by correction patterns that are stamped onto the back-reflector of the bars and by using different concentrations of dye.

The calorimeter PMTs have active bases. These eliminate the use of approximately 10^5 high voltage cables and have reduced power dissipation. A low DC voltage, with a maximum of 24 V, powers a 180 KHz oscillator. A step up ferrite transformer boosts the RF output to 120 V and drives a small Cockroft -Walton generator that is based on a series of capacitors, separated by diodes, that increase the voltage on successive dynodes of the PMT.

3.4.3.5 Calorimeter Resolution and Calibration

The energy resolution for 15 GeV electrons was measured in test beams [82] to be $\sigma(E)/E = 0.176/\sqrt{E}$ for FCAL modules and $\sigma(E)/E = 0.174/\sqrt{E}$ for RCAL modules, where E is in GeV. The response to electrons in the range 15 to 110 GeV was linear to within $\pm 1\%$ for FCAL EMCs. FCAL HACs and RCAL, which have a different type of PMT, showed deviations of 2% at 110 GeV. The resolution for hadrons was determined to be on average $\sigma(E)/E = 0.35/\sqrt{E}$ [78], in the energy range 2 - 100 GeV. Only a subset of the modules was calibrated in the test beams, but the module to module variations were less than 1% so there is no difficulty in transferring the energy scale to uncalibrated modules.

The absolute energy calibration, i.e. the factor for converting the charge collected by the PMTs into an energy in GeV, was also established in test beam measurements. The method is essentially the following. The total current is measured for a particle of a known energy for a given PMT high voltage setting. However, PMT gains can drift in time and, furthermore, when the

modules are transferred from the test environment to the HERA environment, the high voltage may not be at the exact value as the one demanded. The stability of the calibration is assured by using the quasi-DC current resulting from the radioactive decay of the U^{238}. This current is due to photons and electrons that penetrate the steel cladding and enter the scintillator. (Alpha particles from the decay are absorbed by the steel cladding.) It is proportional to the gain of the channel up to, and including, the PMT. The uranium has a lifetime of 4.5×10^9 years and so provides a stable signal, known as the UNO signal. It is determined by integrating the current for 20 ms. This time constant gives an accuracy of better than 1%. The EMC PMT high voltages are adjusted to give nominal current values such that the signals from minimum ionizing particles in the EMC sections appear in ADC channel 100; the currents in the other sections are derived by scaling with the volume of uranium. The currents from the PMTs are multiplied by the ratio of the nominal UNO signal to the measured UNO signal. Charge injectors on the Analog Cards are used to control the gain of the readout electronics from the PMT onwards. The absolute calibration is stable at the 1% level [79].

Before their installation into ZEUS, six FCAL and four RCAL modules were calibrated in test beams and the relative calibration of forty of the CAL modules was determined by cosmic ray muons [83]. The method of intercalibrating the modules prevented considerable delays that would have arisen if all of the modules had to be tested in a test beam.

A laser system injects light pulses into the light guides just before the PMTs. It is used to control the linearity of the PMTs and readout electronics. It is also employed to calibrate the time measurement since the timing of the pulses is known. The time resolution is a function of energy and was measured to be roughly $0.5 + 1.5/\sqrt{E}$ ns. This includes a contribution from the time jitter of the laser that is used to calibrate the times.

The calorimeter noise, which is primarily due to the uranium radioactivity, is in the range 17-19 MeV for EMC cells and 24-30 MeV fo. HAC cells. It is discussed in more detail in Chapter 5.

3.4.3.6 The Hadron-Electron Separator

It is possible to use the CAL for electron identification through the ratio of energy deposition in the HAC and EMC sections. However, there is a certain probability, $P_{h->e}$, that isolated hadrons could be misidentified as electrons. As an example, $P_{h->e}$ is about 0.7% for 5 GeV hadrons, if it is required that the electrons are detected with 90% efficiency [84]. For electron detection within or near a high multiplicity jet, the problem becomes much more difficult.

The solution is to place silicon diodes in the EMC sections. Provision for this detector, the hadron-electron separator or HES, has been made by leaving 15 mm gaps in the FCAL at 3.3 X_0 and 6.3 X_0 and in the BCAL and RCAL at 3 X_0. Since electromagnetic showers develop sooner than hadronic showers, the diode energy distributions for monoenergetic beams of electrons and pions are considerably different: the electron distribution is broad and centered about the beam energy, whereas the pion distribution is peaked at zero with a tail extending to the beam energy. The diodes are 3 cm x 3.2 cm and are mounted on "skis" which slide into the gaps. During the run, three modules of the RCAL were instrumented with diodes. The spatial resolution in both x and y was measured to be 7 cm.

When the diode and CAL information is combined, $P_{h->e}$ is reduced to 0.2% for 5 GeV hadrons. This is sufficient for electron identification in neutral current events. For electrons in jets, the improvement is a factor of five and it is expected that there will be only about 10% contamination of electrons by hadrons in jets in the FCAL and BCAL. (The contamination is equal to the hadron to electron ratio times $P_{h->e}$.)

3.4.3.7 The Backing Calorimeter

It is assumed in using the CAL to measure particle energies that it is thick enough to contain all of the energy. In order to ensure that this is the case, a backing calorimeter (BAC) [85] can veto events in which there is energy leakage or attempt to estimate the leakage.

The BAC is a sampling calorimeter that uses the plates of the iron yoke as the absorber material. Aluminum proportional tubes, inserted into slots in the yoke, are used for the readout. Each consists of 15 mm x 10 mm cell through which runs a gold plated tungsten anode wire. The cells are assembled into 7- or 8-tube wide modules which are covered by aluminum cathode pads. There are nine layers of tubes in the barrel region, ten layers in the forward region, and seven in the rear.

The energy is measured by summing the wire analog signals and the cathode signals. There is thus the option to add this to the CAL energy. The expected energy resolution is $\frac{\sigma(E)}{E} = \frac{1.1}{\sqrt{E}}$.

3.4.4 Muon Detectors

The muon detectors are the outermost components of the ZEUS detector system. Since muons are not subject to the strong force and do not lose much energy to Bremsstrahlung, they easily penetrate the CAL and the BAC. Electrons and hadrons, on the other hand, are unlikely to

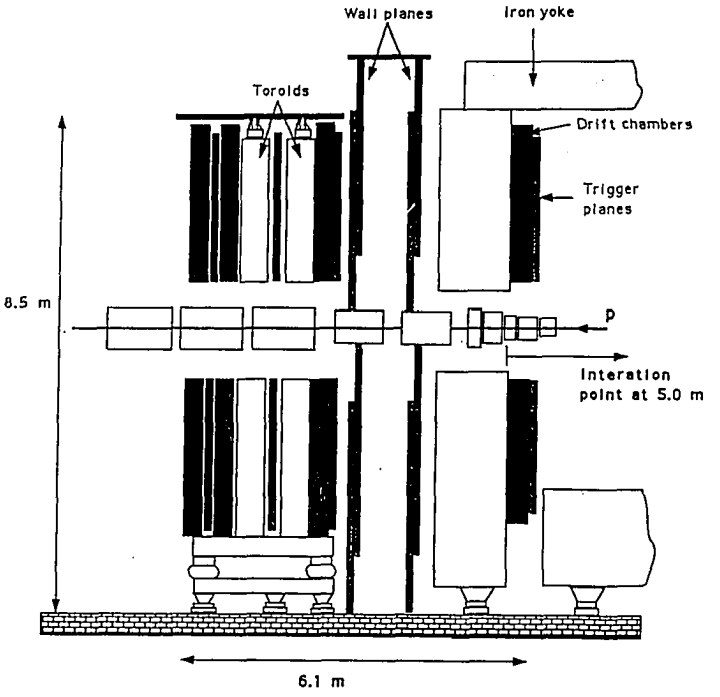

Figure 3.10: Vertical section through the FMUON detector along the beam axis.

do so. The determination of muon trajectories and momenta is important for the study of heavy flavour decays in addition to the rejection of background events, e.g. cosmic rays, beam-halo muons, or muons resulting from pion decays.

3.4.4.1 The Forward Muon Detector

The forward muon detector (FMUON) is a muon spectrometer comprising iron toroids interleaved with a set of drift chambers and limited streamer tubes (LSTs). A vertical section through the detector is shown in Figure 3.10. It is designed to provide an independent measurement of muon momenta up to approximately 100 GeV which will be particularly important at angles less than 200 mrad where the combined CTD and FTD resolution is poor. It provides coverage in the polar angular range from 5° to 32°. Detection of muons in the forward hemisphere is exigent because of the large boost at HERA.

There are two toroids 6 m in diameter with a combined thickness of 0.90 m. Each toroid has eight coils which provide an average bending field of 1.7 T.

A precise muon position measurement is provided by 4 planes of drift chambers each formed by 8 trapezoidal chambers. The chambers are made of aluminum honeycomb walls. Each chamber

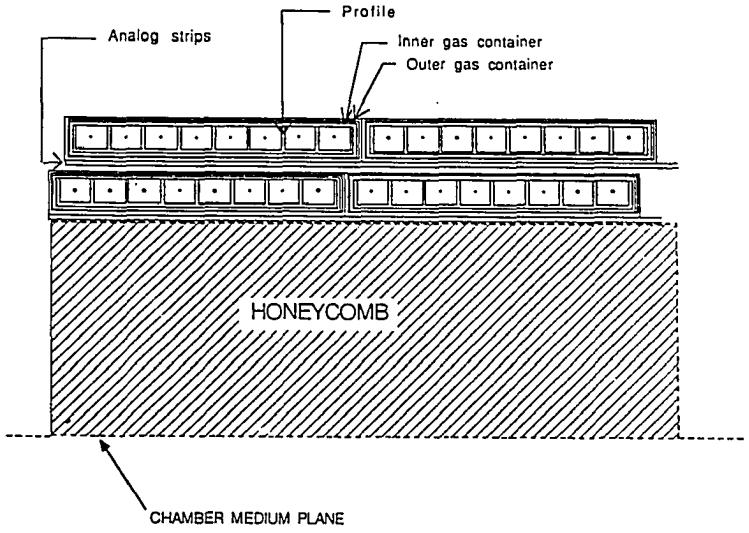

Figure 3.11: Cross-section of a BMUON chamber.

has 32 drift cells which run parallel to the chamber base in order to provide a good measurement of the radial coordinate. The cells are 73 mm x 60 mm with a wire length that varies from 570 mm to 2530 mm, depending on the radius.

Four planes of LSTs provide a trigger based on the direction and momentum of the candidate muon and also $\rho - \phi$ tracking information. Each plane is constructed from four chambers. Within a chamber, there are two layers of tubes placed horizontally. The layers are displaced by half a cell width to improve the acceptance. For each layer in the quadrant, ϕ strips and ρ strips are read out. The acceptance in the polar angle is between 5° and 33°. In addition, two planes of tubes cover the range from 18° to 36° and ensure intermediate angular coverage.

3.4.4.2 The Barrel and Rear Muon Detectors

Muon detection in the central and rear regions of ZEUS is accomplished by the barrel (BMUON) and rear (RMUON) detectors, respectively [86]. Each detector has two layers of muon chambers: one inside the magnetized iron yoke and the other outside. Muon momenta are determined by a direction measurement on each side of the yoke.

Each chamber consists of two double layers of LSTs. These are placed longitudinally with

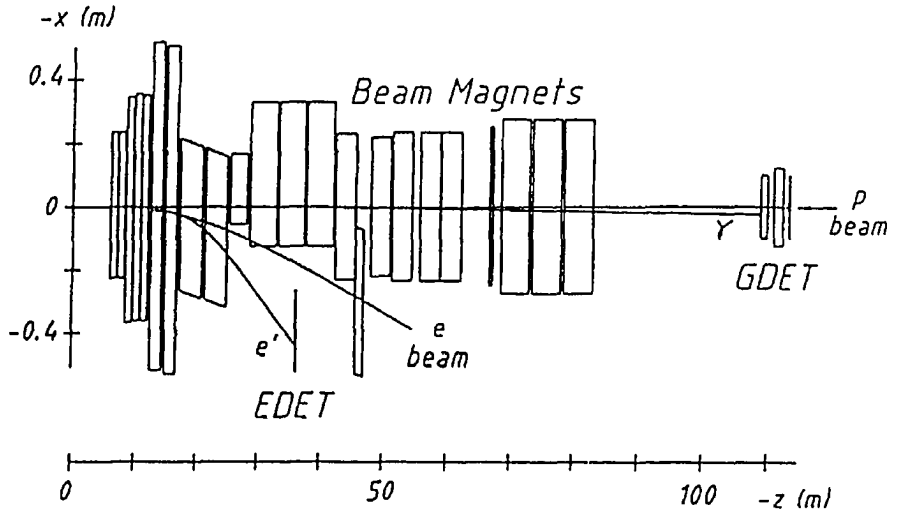

Figure 3.12: General layout of the luminosity detectors.

respect to the beam axis in the barrel region and horizontally and orthogonal to the beam axis in RMUON. Within each chamber, the two double layers of LSTs are separated by an aluminum honeycomb structure that gives mechanical support and provides the separation necessary for a precise measurement of the incident and exit angles. A cross-section of half of a muon chamber is shown in Figure 3.11. A typical chamber has dimensions 2 m x 8 m. The total active area is greater than 2000 m^2.

3.4.5 Small Angle Detectors

3.4.5.1 Luminosity Detector

Luminosity is measured by determining the rate of occurrence, R, of a process with a well known cross-section, σ. The luminosity, $\mathcal{L}$, is then calculated from Equation (3.2). The Bethe-Heitler process $ep \rightarrow ep\gamma$ is measured by the HERA experiments because it has a clear experimental signature and a large cross-section given by the formula

$$\frac{d\sigma}{dk} = 4\alpha r_e^2 \frac{E'}{kE}\left(\frac{E}{E'} + \frac{E'}{E} - \frac{2}{3}\right)\left(ln\frac{4E_pEE'}{m_pm_ek} - \frac{1}{2}\right), \qquad (3.11)$$

where E and E' are the initial and final electron energies, and E_p is the proton energy. The principal problem with this method is the large background from electron scattering off the

residual gas molecules in the beam pipe. This has a cross-section about six times larger than the electron-proton Bethe-Heitler process because of the strong Z dependence on the cross-section as is seen in Equation (3.7). This background is subtracted using the electron pilot bunch.

The layout of the luminosity detectors is shown in Figure 3.12. The photon is emitted at a small angle ($\theta_\gamma \leq 0.5$ mrad) with respect to the beam axis and travels down the proton beam pipe. At about -70 m there are dipoles which give the proton beam a vertical bend. The photon continues travelling along its original line of flight until it reaches a photon calorimeter at -107 m from the interaction point. There is a 2 X_0 carbon filter, made of graphite blocks, in front of the calorimeter that absorbs synchrotron radiation. The photon calorimeter is a lead-scintillator sandwich type calorimeter. Silicon pads have been placed at a depth of 7 X_0 to measure the horizontal and vertical position of the photon. This is important for determining the photon geometrical acceptance.

Scattered electrons are off the beam energy and are deflected out of the beam pipe at -10 m by the beam bending magnets. The electron detector, located at about -35 m, is also a lead-scintillator electromagnetic calorimeter. Both calorimeters have an energy resolution of $0.18/\sqrt{E}$. Figure 3.13 shows a scatter plot of the final state electron and photon energies as measured in the luminosity detectors. There is a band of events for which the sum of the two energies is equal to the energy of the electron beam.

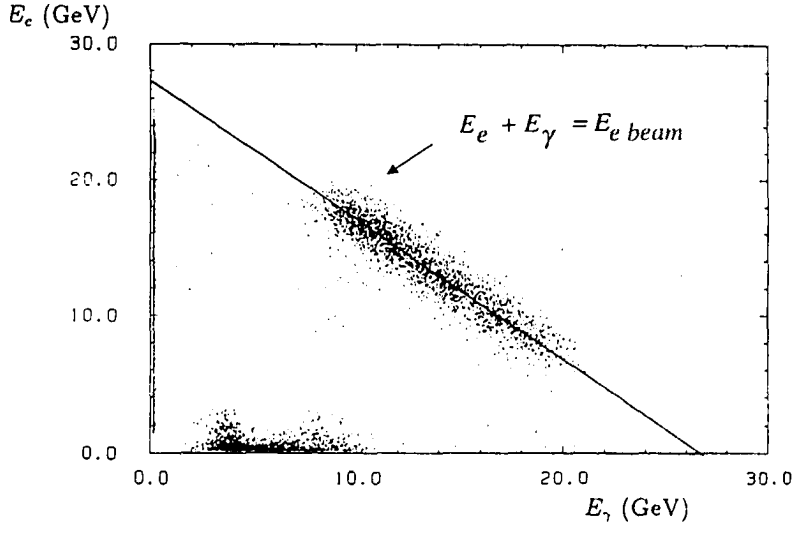

Figure 3.13: Distribution of the electron energy vs. the photon energy measured in the luminosity detector calorimeters. Figure from [87].

3.4.5.2 Leading Proton Spectrometer

The leading proton spectrometer (LPS) is designed to measure forward scattered protons with transverse momenta less than 1 GeV and longitudinal momenta greater than one third of the proton beam energy. One example of a process expected to yield a leading proton is diffractive scattering. The LPS has six detector stations located in the proton beam line at 24 m, 41 m, 44 m, 63 m, 81 m, and 91 m. Each station has silicon strip detector planes designed to measure horizontal and vertical hit positions.

3.4.6 Readout and Trigger Systems

3.4.6.1 Concepts

The readout and digitization of the component signals was a considerable challenge for the HERA experiments since the beam crossing interval is only 96 ns. This is orders of magnitude below the bunch crossing times of existing colliders and required the development of novel readout and trigger systems that can store and analyze the signals at the required rate.

Although the bunches cross every 96 ns, the rate of interactions is not 10 MHz, but is estimated to be approximately 50 kHz [88]. The majority is background from proton beam interactions with the residual gas in the beam pipe. Due to kinematical acceptance, the events that can deposit energy in the detector have z vertices ranging from about 2 m to -100 m. The rate of deep-inelastic electron-proton scattering at design luminosity is only on the order of 1 Hz, but the trigger rate is dominated by several hundred Hz of low Q^2 scattering events.

The interesting physics events could conceivably be separated from the background offline. However, there is a practical difficulty: the component readout systems are inactive during the digitization of the analog signals. This is known as *deadtime*. The high background to signal ratio would result in the collection of almost no events of interest if the deadtime was above 1%. Furthermore, there does not exist a system that can record the required amount of information if all of the events were accepted. The event size is estimated to be roughly 200 kBytes based on the number of readout channels and their dynamic range. This would give a data rate of 50 kHz X 200 kBytes, i.e. 10 GBytes/sec. Therefore, a *trigger* system that recognizes that an interaction has occurred and can discriminate between background and interesting physics events is needed.

An efficient trigger system that combines information from several components is unable to

arrive at a decision within 96 ns of an interaction for two reasons. The first is that it takes longer than this to perform the necessary calculations and message passing among the components. The second is that some components do not even detect their signals until several beam crossings after the interaction of interest, e.g. tracking chambers with long drift times. This means that the component readout systems must be able to store information from several events until a trigger decision is received. If they become inactive during this period, deadtime is introduced.

The continuous storage of signals is achieved with a FIFO† or pipeline. This is a system into which data enters every 96 ns and is continuously pushed forward as new data enters. Each channel in ZEUS has to be pipelined. The length of the pipeline is specified by the time for the slowest component to process its data, the time required by a global trigger processor to analyze the components' data, and the time associated with cable delays. A pipeline gives a deadtime free system until a positive trigger decision is received. At this point, the components must read out their pipelines and it is inevitable that some deadtime is introduced.

3.4.6.2 The ZEUS Trigger System

The trigger system is divided into three levels, where each level is defined by the decision time available. Most of the components have *local* first and second level triggers upon which *global* first and second level trigger decisions are based. The third level trigger bases its decision upon its own analysis of the complete event data. A schematic overview of the trigger and data acquisition system is shown in Figure (3.14).

The design of the global first level trigger (GFLT) anticipates an acceptance rate of 1 kHz. This number arises from several considerations. Foremost, is the requirement to keep the deadtime to below 1%: every time there is a GFLT accept, the components are inactive while they read out their pipelines. The GFLT, therefore, must perform logical operations on the local trigger results and arrive at a decision within 5 μs, i.e., 46 beam crossings. In order to allow for signal propagation delays, the component data is stored for 58 beam crossings in local pipelines. The pipelining ensures that there is no deadtime at this point. A positive decision triggers the components to read out their pipelines, digitize any remaining analog signals, and write the data into dual-port memories. These memories serve as second level trigger pipelines. During this operation, deadtime of about 1% is introduced at the design luminosity. (In future, there will exist the possibility abort the readout to the second level trigger pipelines based upon a quick analysis

†. First In First Out

ZEUS trigger scheme.

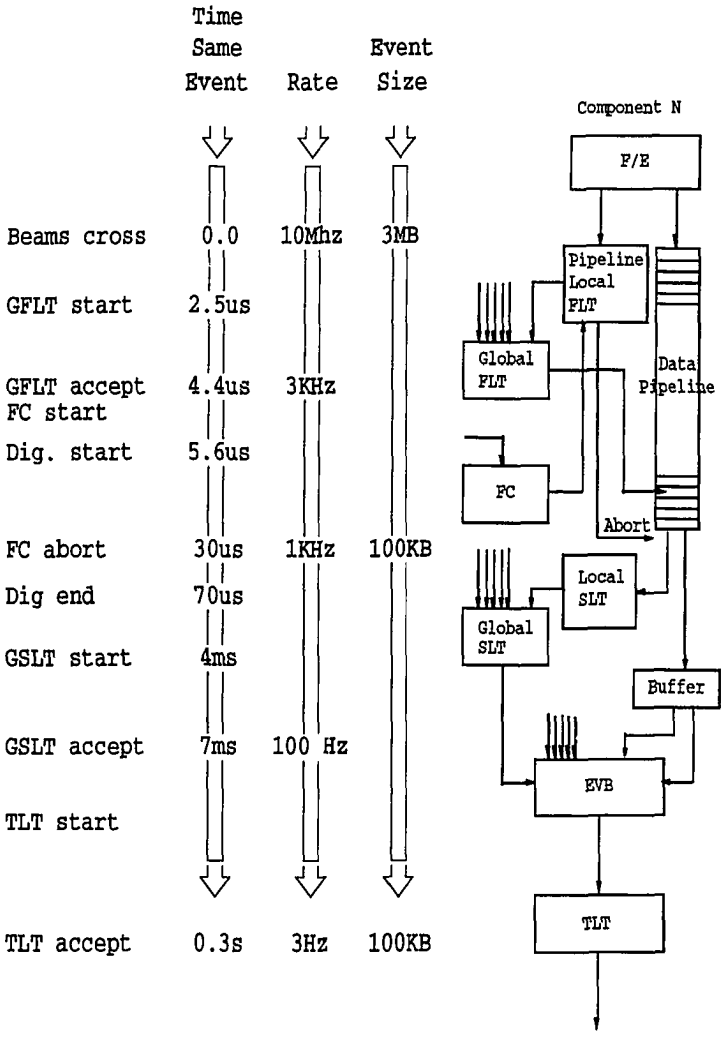

Figure 3.14: The ZEUS trigger system and data flow.

of the calorimeter first level trigger data. This hardware trigger processor is known as the fast clear.)

The components split their signals at the readout stage, with one part stored in a local analog or digital pipeline and the other sent to a component first level trigger (FLT) processor. The local processors are required to send their results to the GFLT within 2.5 μs of the crossing. Because of the short time available and the specific nature of the computations, they are custom built devices. The FLT processors do not necessarily have access to the full component data. For instance, the CAL has sixteen regional processors which work with neighbouring groups of cells and cannot make use of the full dynamic range of the calorimeter. In total, the GFLT receives fifty-one 16-bit data words. The trigger logic is discussed in the following section.

The synchronization of the trigger and readout system is done with a clock that is phase locked to the HERA bunch structure. The GFLT receives the signal from the HERA machine clock and distributes it to all the components.

The second level trigger (SLT) system has the task of reducing the trigger rate by a factor of ten from 1000 Hz to 100 Hz. This implies that the SLT processors have a decision time of a few milliseconds and can be implemented on programmable processors. A typical example of the hardware implementation is a network of transputers. A transputer is a single VLSI chip which has a processor, memory, and communications hardware. The latter comprises four serial links. The IMS T800, a typical transputer used in ZEUS, has a sustained uni-directional transfer rate of 1.7 MBytes/sec and a bi-directional rate of 1.1 MBytes/sec over distances less than 15 m. The data links and support of **occam**, a computer language that is appropriate for asynchronous parallel systems, make transputers suitable for a geographically distributed trigger and data acquisition system.

The SLT processors have access to more complete data than the FLT processors. It has also been fully digitized, i.e. the full dynamic range is utilized. This means that the calculations are more precise than at the first level. In addition, since the available processing time is about 5 ms and the data is accessible in buffers, the SLT processors can perform some iterative calculations. For example, the CAL processors group cells with energy deposits into clusters and the CTD processors estimate particle trajectories through the chamber. A Global Second Level Trigger (GSLT) combines the results of local processors, cross-checks them, and applies selection criteria to reach a decision.

If the GSLT accepts an event, the data from all the components corresponding to the accepted

event must be assembled in a single memory location for access by the third level trigger (TLT). This is the primary task of the event-builder (EVB) [89]. It transports the component data from local memories over transputer links to one of six TLT inputs. It is based on an asynchronous packet-switching transputer network. A 64 x 64 crossbar switch provides the connection between any component to any input of the TLT. This switch has a bandwidth of 24 MBytes/sec. The EVB also formats the event data into ADAMO data structures [90] and is responsible for broadcasting the GSLT decision to the components.

The function of the TLT is to further reduce the event rate from 100 Hz to around 5 Hz and, therefore, it has several hundred milliseconds of available processing time per event. The input rate is based on such factors as the bandwidth of the EVB and the time required to execute sophisticated trigger algorithms. Accepted events are written out via an optical link to an IBM mainframe for mass storage and to a central VAX for data quality monitoring. The output rate is essentially limited by the bandwidth that can be written to cartridges on the IBM. The TLT comprises thirty computers which are organized into six parallel branches. The hardware and control software will be described in some detail in the next chapter.

A two stage trigger strategy is necessary at the TLT because of the high rate of low Q^2 physics events. First, a series of algorithms designed for background rejection are run on the events. Then, the remaining events are passed through filter algorithms designed to select specific classes of physics events. Only background rejection was performed during the 1992 run because of the low luminosity. For 1993, four different filters were implemented. These employed relatively simple kinematic cuts based on CAL energy deposits, track counting, track matching with CAL clusters, and vertex position. Prescale factors are used to ensure that the combined filter acceptance rates do not exceed 3 Hz. A breakdown of the different contributions to the output rate for a typical run in 1993 is shown in Table 3.1.

The trigger system and the component readout systems comprise the experiment data acquisition system [91]. A run control program running on the central VAX is required to synchronize the more than twenty component and trigger computers. The run control uses a predefined set of commands and messages to coordinate each data-taking period. Individual data acquisition and trigger systems should always be in the same well defined state or simultaneously undergoing a transition from one state to another. For example, if data-taking must be paused because of high background rates, the run control informs the data acquisition computers to change from the ACTIVE to the PAUSED state. If this was not done, some systems that are data driven, such as the EVB or TLT, would timeout and enter into an

ERROR state. Other systems would remain ACTIVE and the system would no longer be synchronized.

Type	sub-category	Rate (Hz)
pass-through events		0.16
special triggers		0.2
sampling filter		0.35
physics filters		2.3
	soft photoproduction	0.8
	hard photoproduction	1.0
	deep-inelastic	0.5
	exotica search	0.5
total output rate		3.0

Table 3.1: Output rates from the TLT for different event categories. The rate for all of the physics filters is less than the sum of the rates since some events are accepted by more than one filter.

3.4.6.3 The Trigger

The intended final trigger system was not in place when the data for this thesis was collected. However, the available trigger was able to handle the input rate because HERA was not operating at full luminosity.

The GFLT decision was primarily an activity trigger based on CAL and C5 inputs. For triggering purposes, the CAL readout channels were grouped into 448 non-overlapping HAC and EMC *trigger towers* having a transverse size of about 20 cm x 40 cm. (The transverse size of a trigger tower is roughly equivalent to two mechanical CAL towers.) A first level trigger was issued whenever the energy sum in any of the EMC or FCAL HAC trigger towers exceeded a programmable threshold. The thresholds used are shown in Table 3.2. The second set of RCAL thresholds were used in conjunction with other requirements to trigger on very low Q^2 events in which the scattered electron does not enter into the active volume of the CAL. The thresholds shown in the first two columns were those used to select the data analyzed in this thesis. The FCAL beampipe region comprises the inner two rings of mechanical towers and the inner region contains the next two rings of towers. The RCAL beampipe region consists of the ring of towers

surrounding the beampipe.

First level triggers were vetoed if their signals were in coincidence with a signal from the C5 counters that was in time with the proton beam. These triggers are likely due to proton beam induced background events occurring outside of the detector region. The total first level trigger rate was about 18 Hz.

Region	HAC	EMC	EMC
FCAL Beampipe	70.0	50.0	-
FCAL Inner	25.0	20.0	-
FCAL Outer	10.0	10.0	-
BCAL	1.0	1.0	-
RCAL Non-beampipe	1.0	1.0	0.4
RCAL Beampipe	2.5	10.0	2.5

Table 3.2: Calorimeter first level trigger thresholds (in GeV) used for this run period.

Proton beam-gas events or proton interactions with the beampipe occurring upstream of the detector in the proton direction can deposit energy in the RCAL. The time at which the energy of the collision products is deposited will be earlier than the time from an electron-proton collision. The difference is approximately equal to the time it takes particles to travel twice the distance from the nominal interaction point to the RCAL. This corresponds to 11 ns. Since the origin of time for a given cell has been defined to be the time at which relativistic particles from an electron-proton collision at the nominal interaction point would deposit their energy in the cell, proton beam induced background events should have an RCAL time, t_{RCAL}, centered at about -11 ns. Assuming zero proton bunch length, the FCAL time, t_{FCAL}, should be zero for all events since particles reach FCAL at the same time regardless of where they originate.

Figure 3.15 shows the FCAL and RCAL timing distributions as measured online by the TLT during the 1993 run. The times are calculated as energy weighted sums from all PMTs in a given part, viz.,

$$t = \frac{\sum_i w_i t_i^{PMT}}{\sum_i w_i}, \tag{3.12}$$

where t_i^{PMT} is the time of the energy deposit measured by the PMT. The weight function, w_i, is defined by

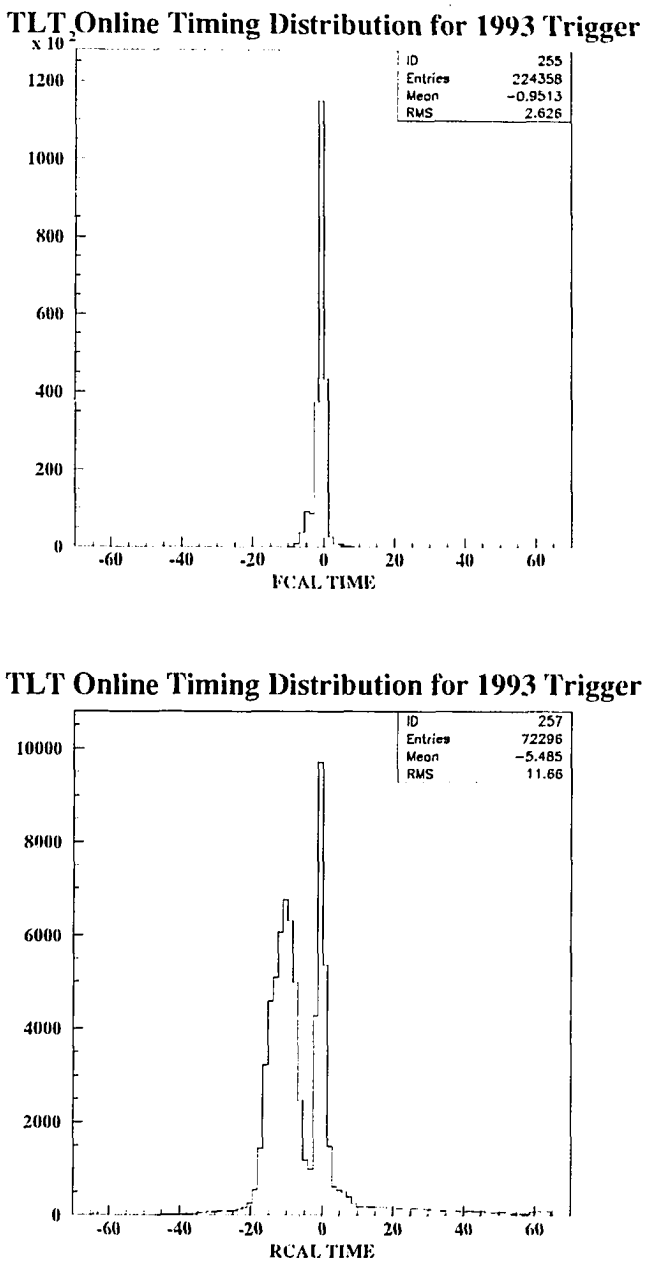

Figure 3.15: FCAL and RCAL timing distributions as measured online by the TLT. The times are measured in nanoseconds.

$$w_i = \begin{cases} 0 & \text{if } E_i^{PMT} < 0.2 \\ E_i^{PMT} & \text{if } 0.2 \le E_i^{PMT} \le 2 \\ 2 & \text{if } E_i^{PMT} > 2 \end{cases} \quad (3.13)$$

where E_i^{PMT} is the energy in GeV. The sum of the cell energies contributing to the sum must be greater than 1 GeV. The FCAL distribution is centered roughly around the origin, as expected. Two peaks are clearly seen in the RCAL distribution; one is centered around 0 ns and the other around -10 ns.

The width of the distributions is due to the proton bunch width and the fact that the bunches can be off-time. One can assume that both bunches are in-time, i.e. their centres cross the interaction point at the same time, and that the electron bunch is pointlike. The electron bunch will come into contact with the proton bunch at $z = l/4$, where l is the length of the proton bunch. If the electron collides with a proton at this point, t_{FCAL} will be $-l/4c$. The electron has roughly the same distance to travel to RCAL whether or not it collides at the interaction point. For interactions inside the active volume of the detector, t_{FCAL} depends on the proton bunch length and t_{RCAL} depends on the electron bunch length.

The RCAL time cannot be exclusively used for a trigger for upstream events because the t_{RCAL} distribution depends on the proton bunch length in this case. The proton bunch length also affects the distribution in t_{FCAL}, but it does not affect the difference t_{FCAL} minus t_{RCAL}. Figure 3.16 is an online CAL timing lego plot from the TLT that illustrates the good separation between background and physics candidate events on the basis of t_{RCAL} and t_{FCAL} minus t_{RCAL}. It can be seen in the figure that the spread in t_{RCAL} is smaller than the spread in t_{FCAL} minus t_{RCAL} for physics candidates. This demonstrates that the electron bunch length is smaller than the proton bunch length.

The TLT rejects background events by a cut on the average FCAL and RCAL times. The algorithm used for the collection of the data presented here calculated t_{FCAL} and t_{RCAL} from the towers surrounding the beampipe. A simple average of all the times from all cells with an energy exceeding 1 GeV were used to calculate the times. The algorithm in pseudocode was

IF $|t_{FCAL} - t_{RCAL} - 10.5| < 4.5$ ns AND
$|t_{RCAL} + 10.5| < 4.5$ ns THEN
Reject event as beam-gas event.

About 35% of the events passing the GFLT were removed by the timing cut. For the 1993 run, an

algorithm based on an energy weighted average of all cells and with tighter cuts was used. The algorithm was tested online in 1992 by flagging events.

In addition, the TLT removed events in which electrical discharges, or *sparks*, in CAL PMTs cause the trigger conditions to be satisfied. Sparks are believed to be caused by random discharges in PMT bases or between PMT cathodes and the shielding. The definition of a spark was a cell of energy greater than 60 MeV with an energy imbalance greater than 0.9 between the two PMTs of the cell. The energy imbalance is defined to be

$$imbalance = \left| \frac{E_{left}^{PMT} - E_{right}^{PMT}}{E_{left}^{PMT} + E_{right}^{PMT}} \right|. \qquad (3.14)$$

One and only one CAL FLT trigger bit could be set and the sparking cell had to be in the

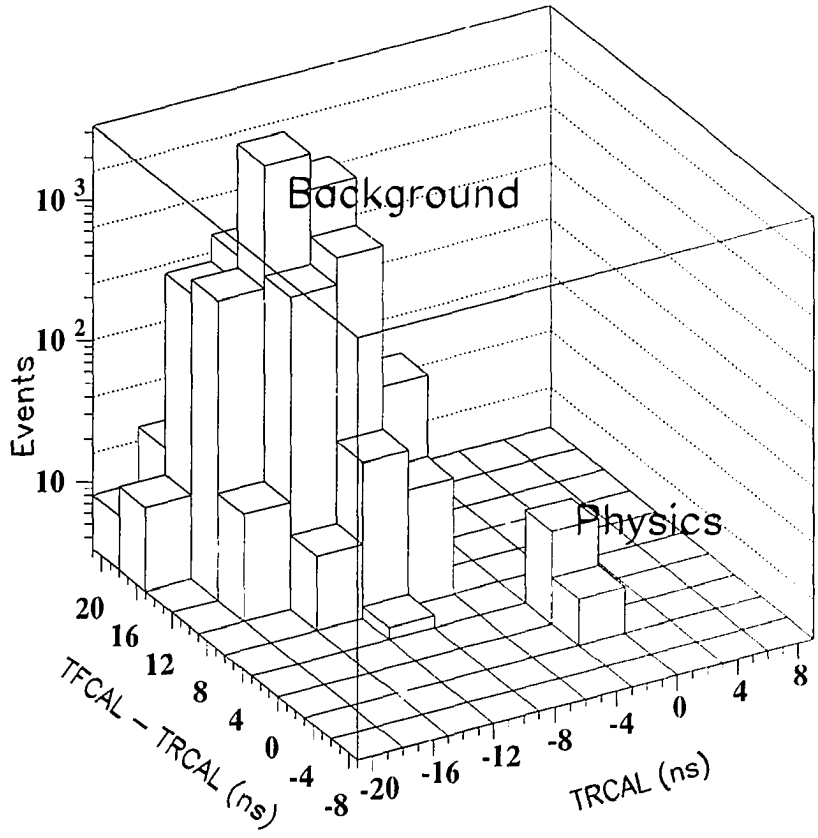

Figure 3.16: TLT lego plot showing t_{FCAL} - t_{RCAL} vs. t_{RCAL}.

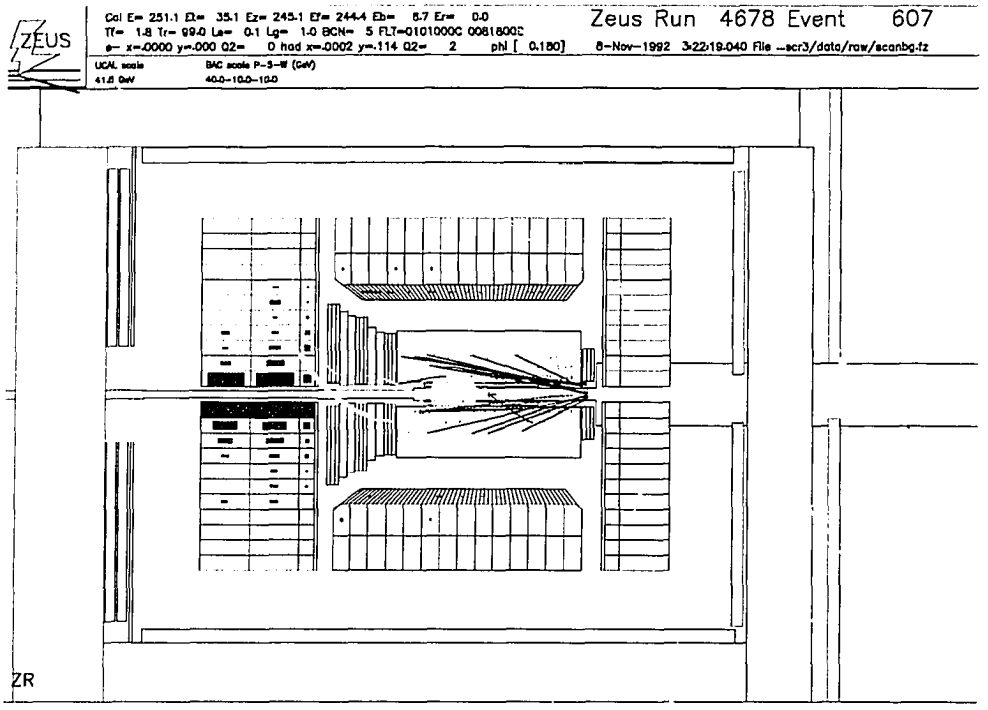

Figure 3.17: A proton beam-gas event with TLT reconstructed tracks.

corresponding trigger region. Finally, the total energy in the calorimeter minus the spark energy was required to be less than 2 GeV. Such events cannot be recognized by the first level trigger because it does not have access to all of the data from each event. This trigger removed about 30% of the GFLT accepted events.

Further reduction of background events originating outside of the interaction region is possible by determining the event interaction vertices. A fast three dimensional track reconstruction from hits in the CTD and VXD is done online at the TLT. The calibration of constants is carried out during data taking in real time. Figure 3.17 shows a beam-gas background event that was identified by the TLT from track reconstruction using the partially instrumented CTD. The tracks are clearly pointing to a vertex just outside of the interaction region. This event could not have been rejected on the basis of CAL timing as there was no energy deposited in the RCAL. During 1992, the TLT only flagged events classified as beam-gas by vertexing.

There are also background events from cosmic rays and halo muons. Halo muons result from the decays of pions that are produced in inelastic collisions of the beam protons with the rest gas or beam pipe components. Their trajectories generally correspond to the beam trajectory. Muons are identified by the fact that they are minimum ionizing and traverse the entire detector. The CAL energy, time, and cell positions are used to reduce this background. For example, the time difference between the top and the bottom of the BCAL is required to correspond to the transit time of a muon for cosmic ray candidates. An algorithm to detect background muons flagged events during the 1992 running and rejected events during the 1993 run.

After extensive checks of the CAL timing algorithm at the TLT, it was adapted to the GSLT during the latter part of running in 1992. A BCAL spark trigger was implemented at the GSLT after it was shown to be equivalent to the spark algorithm described above. This migration of triggers from the TLT to the GSLT is a strength of the TLT as it is relatively easy to implement, test, and understand new algorithms at the TLT. The GSLT also rejected cosmic rays based upon a BMUON trigger in combination with CAL and CTD SLT information.

Before any cuts were introduced at the GSLT, the rate of events into the TLT was about 18 Hz. The cuts described above reduced this to about 4 Hz. The deadtime was less than 0.1%. The trigger acceptance is discussed in Chapter 5.

3.4.6.4 The CTD Z-by-Timing Readout

The CTD z-by-timing readout system [92] provides a fast vertex determination that can be used for triggering. The system measures the difference between the arrival times of a pulse at each end of a sense wire. This difference can be converted into a z coordinate given the propagation velocity of the pulse along the wire. During the first run period, this readout system was used for track reconstruction. A tracking program, VCTRACK, has been running online in the TLT since the start of data taking. An advantage of online track reconstruction is that the results are contained in the dataflow of each event, thereby saving processing time offline.

The z-by-timing electronics are shown schematically in Figure 3.18. Pulses from each end of appropriately instrumented sense wires are amplified by preamplifiers that are mounted on the end-flanges of the chamber. The preamplifiers drive 42 m of coaxial cable to differential postamplifiers. The signals are subsequently fed into constant fraction discriminators which minimize the timing slew. The signal from the rear end of the detector provides the start pulse for a time-to-amplitude converter with a 50 ns cycle time. The stop pulse is provided by the signal

from the forward end of the chamber. A 10 ns delay is used to ensure that it always arrives after the start pulse.

The receipt of a start pulse causes a constant current source to begin charging a capacitor. When the stop pulse arrives, the charging ceases and the voltage across the capacitor, which is proportional to the time difference between the stop and start signals, is sampled by a 35 MHz flash analog-to-digital converter operated as a 7 bit device. The capacitor is then discharged. The maximum time between the receipt of a start pulse and the restoration of the baseline is 50 ns. The system can be calibrated by injecting test pulses at one of the two ends of the sense wires. The design resolution is 200 ps, which corresponds to 3 cm.

The data is simultaneously written to a 5 μs digital pipeline and the CTD first level trigger processors. The pipeline is implemented using fast random access memory (RAM) and a clocked Master Address Generator. The clock cycle time is 48 ns as it must be less than the cycle time of the

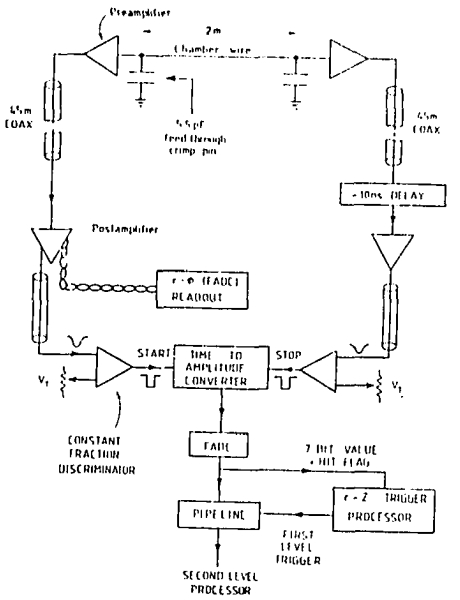

Figure 3.18: Block diagram of the time difference measurement electronics.

time-to-amplitude conversion. At each cycle, data is written into a RAM address generated by the Master Address Generator. As long as no GFLT accept signal arrives, the address lines are continuously cycled. If there is an accept, the Master Address Generator is stopped and the data corresponding to the accepted beam crossing is read out to the SLT system.

3.4.6.5 The Calorimeter Readout

The CAL readout electronics [93], [94] have stringent requirements. They must provide pipelined storage of the signals to give 1% deadtime at the nominal GFLT accept rate. The required dynamic range is governed by HERA kinematics. The most exacting demand is for FCAL EMC cells where it is possible that up to 400 GeV could be deposited in a single cell. The lower limit is set by calibration signals, e.g. uranium noise or minimum ionizing particle energy deposits. A minimum ionizing particle will deposit about 300 MeV in an EMC cell which must be measured with a precision of 3 MeV. This is a range of five orders of magnitude and requires seventeen bits. Nanosecond precision on the time of the energy deposition is necessary to reject background events. Finally, the system is required to read out signals produced by the uranium noise and to sum the signals from neighbouring PMTs to provide an input to the CAL FLT.

The analog PMT readout electronics are contained on Analog Cards which are mounted directly on the CAL modules to avoid cabling and noise problems. A schematic of a typical Analog Card is shown in Figure 3.19. Each signal is split into four channels: a channel for integrating the uranium noise (RM), high (RH) and low (RL) gain channels, and a channel that provides FLT analog sums (RT). Two different gain channels are required to provide the necessary dynamic range because sufficiently fast analog-to-digital converters usually only have a twelve bit range. The gain is determined by the input impedances, RH and RL, since the rest of the circuit is identical for both channels. As an example, the FCAL PMT high and low gain ranges are 0 to 18 GeV and 0 to 400 GeV, respectively.

A PMT signal arriving at the input of an Analog Card has a typical signal width of 20-30 ns. It is required to measure the charge, i.e. the integral of the pulse, and the time of arrival. The signal cannot be integrated because this is too slow and timing information cannot be obtained. The pulse has to be shaped so that the height of the shaped pulse is proportional to the charge of the original signal. The shaped pulse is sampled by an analog pipeline chip every 96 ns. Since there may be phase shifts between the clock driving the pipeline chip and the HERA clock, it is desirable to sample the pulse on opposite sides of the peak and weight the samples with the slopes

of the pulse instead of attempting to directly sample at the peak of the signal. The pulse height is given by the weighted sum of the two samples. This method implies that the pulse must have a width longer than the sampling interval. The shaper circuit, denoted by the symbol S on the Analog Card, delivers a pulse with a width of about 300 ns. The time measurement is obtained by the ratio of the two samples. Although the shaped pulse is wider than the bunch interval, the probability of an interaction is about 1% so that signal overlap from two consecutive events is not a problem. This can be checked by measuring the baseline before the pulse.

The readout pipeline is a switched capacitor array which also performs the sampling of the signal. A digital pipeline was not feasible because of high power consumption. The analog pipelines are implemented on a CMOS chip that contains four pipelines, each comprising a series of 58 capacitors. A schematic of the pipeline circuit is shown in Figure 3.20. When the signal is being sampled, the input is connected to all of the capacitors but only one has its other plate connected through a closed switch to ground so that current can flow and the capacitor will charge

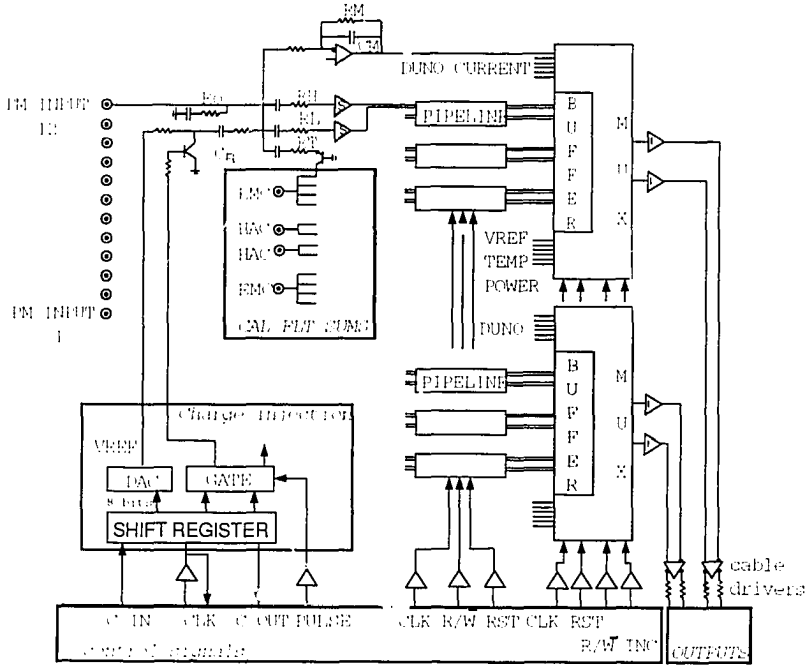

Figure 3.19: Schematic of a typical Analog Card.

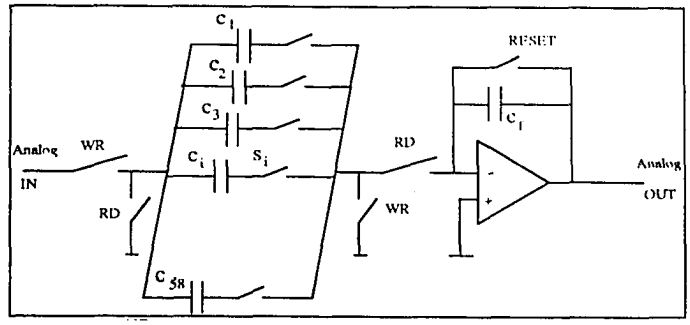

Figure 3.20: Schematic of the analog pipeline circuit.

up. Because the capacitance is only 1 pF and the equivalent resistance of the closed circuit is a few $k\Omega$, the capacitors charge within a few nanoseconds. The voltage can be held for several milliseconds with losses of less than 1%.

When a GFLT accept is received, the pipeline clock is stopped and the samples corresponding to the triggering beam crossing are read out and stored in an analog buffer. All of the capacitors in a pipeline are connected to the same readout operational amplifier. Once the desired samples are in the buffer, the pipelines are cleared and restarted. This method of analog buffering eliminates deadtime due to digitization. The analog signals are subsequently multiplexed to Digital Cards.

On the Digital Cards, the signals are digitized and the results are written to RAM. Digital Signal Processors calculate energies in GeV and times in nanoseconds from the digitized samples and stored calibration constants, and format the data for higher level trigger and data processing.

3.5 Offline Software

Ultimately, it is desired to reconstruct the event kinematics, identify particles, and determine their four-vectors. These quantities cannot be directly determined from data that is written to mass storage because it comprises energy deposits in cells and wire hits. Reconstruction software is used to calculate particle trajectories from drift chamber hits, from which the particle momenta and charges can be deduced. Calorimeter cell energy deposits are used to calculate particle

energies and are also used for particle identification. The reconstruction software can also apply corrections to the data, such as updating detector calibrations and correcting for bad readout channels.

The reconstructed data cannot be directly compared with theoretical predictions since the detector has inactive material, such as cables, and does not have perfect resolution or geometrical acceptance. It is necessary to calculate the effects of a non-ideal detector on the predictions. Since there are too many degrees of freedom, this cannot be done analytically and a detector simulation program based on Monte Carlo methods is used.

3.5.1 Detector and Trigger Simulation

The detector simulation program, MOZART, is based on GEANT 3.13 [95]. This is a general purpose program that provides a framework for describing detector geometry and particle tracking through the detector media. The simulation was checked and parameter settings were tuned by comparisons with test beam measurements. These comparisons showed that the CAL test data for hadronic showers was not described by GEANT; modification of the showering routines [96] was required for accurate reproduction of the test results.

The trigger logic is simulated in the program ZGANA. This permits the calculation of the trigger acceptance and allows for easy testing of new trigger criteria. ZGANA is run on Monte Carlo events that have been passed through the detector simulation. It determines which subtriggers the event would satisfy and sets a corresponding *trigger bit*.

3.5.2 Reconstruction and Analysis Software

It is important to have convenient input/output operations on subsets of the data for an experiment the size of ZEUS. To achieve this aim, the ZEUS reconstruction and analysis software [97] makes use of ADAMO, which is an example of an Entity-Relationship Model. Data is described in terms of entities (e.g. CAL cells or CTD hits), their attributes (e.g. position) and their relationships (e.g. a cell may be associated with a cluster of cells, or a hit may be associated with a track). Entities defined by the same set of attributes form an entity set. ADAMO maps the entity sets onto tables; the precise definition of the entity sets being given by the Data Definition Language (DDL). The tables are grouped into dataflows that allow convenient operations on subsets of tables.

As a specific example, consider the entity set comprising CAL cells that was used for this

analysis, i.e. cells that have energy deposits above some threshold. This set is mapped onto the table CALTRU, which has such attributes as the cell number, the cell energy, and the times from the two PMTs. A programmer accesses this table through a FORTRAN COMMON block that is defined in the DDL. CALTRU is filled by the reconstruction program, ZEPHYR, that gets the required information from tables containing the raw packed data. The calibrated raw data forms the dataflow RAWDATA, whereas CALTRU is part of the PHASE1 dataflow comprising reconstructed data from individual components. All of the component and trigger data is stored in tables.

Analysis programs are usually written within the EAZE program skeleton. This provides all the necessary ADAMO input/output calls. A user need only specify the required dataflows and write analysis subroutines which access the desired common blocks.

A visual display of events is provided by passing the results of the reconstruction software to a description of the detector geometry. The program that does this is called LAZE. It allows one to look at the detector from different perspectives and display reconstructed quantities such as tracks and CAL energy deposits.

3.5.2.1 Calorimeter Reconstruction

During this run, the raw data for each calorimeter cell comprised two longwords, one for each PMT, containing packed calibrated energy and time information. After unpacking, the CAL reconstruction program modules [98] applied offline corrections to the calibration and corrected for bad readout channels. The program removed EMC cells with an energy deposit of less than 60 MeV and HAC cells with less than 100 MeV. If an individual PMT contained less than 30 MeV for the EMC or 45 MeV for the HAC the cells were also removed. These cuts were chosen to minimize the influence of noise on the reconstruction of the kinematic variables. The Monte Carlo generator event samples had measured electronic and uranium noise added to the simulated cell energies and then the above cell and PMT energy cuts were applied. The CAL noise will be discussed further in Chapter 5.

3.5.2.2 Track Finding and Vertexing

Charged tracks are reconstructed from hits in the CTD and the VXD. At the time the analysis for this thesis was done, there were two tracking programs used within the ZEUS experiment; the analysis presented here used the program VCTRACK. The simplified version described below

was used to perform pattern recognition because only the wires with z-by-timing readout were instrumented. It has been modified considerably since 1992 as the instrumentation and understanding of the CTD has improved.

Starting with superlayer five (SL5), VCTRACK found the outermost superlayer with at least two hits. A dummy point at x=y=0 with σ = 5 cm (along the line passing through the origin and perpendicular to the track helix) was used to follow the segment inwards by looking for further hits. Hits were rejected if their spatial coordinates gave a poor fit to the trajectory; both the position in the x-y plane and the z coordinate were checked. For tracks starting in SL5, two of four possible hits were required in both SL5 and SL3 and three of eight possible hits in SL1. Tracks starting in SL3 also required three of eight hits in SL1. For tracks only in SL1, four of eight possible hits were required. A vertexing package [99] was used to fit the tracks to a vertex.

Chapter 4

The Third Level Trigger System

4.1 Introduction: The Bus Concept

The concept of a bus is important for understanding the third level trigger (TLT) system architecture. Busses are used for binary information transfer among processors and memory units. The definition of a bus system can be organized into several logical layers. On the lowest level, a bus is the physical communication medium. This level specifies the number of transmission wires, whether they are embedded in a backplane or enclosed by a single cable, and so forth. The highest level is the communication protocol. This includes defining the rules for accessing and releasing the bus, the exact sequence of events required for a successful data transfer, and error handling. There are various electrical and mechanical specifications in the intermediate levels. For example, it is necessary to detail how processors mechanically interface to the bus, what signal levels are required, etc.

The existence of industry standard bus systems means that processors and memory units fabricated by different manufacturers can communicate with each other. This is essential in a large international collaboration such as ZEUS. The ZEUS experiment uses VMEbus [101], Revision IEEE-1014-1987, as a standard. This is a backplane bus that typically has connectors for twenty-one cards and is housed in a crate. Extended systems can be constructed with *vertical* busses that connect physically separate busses together. There are also proprietary busses, examples of which are the internal busses in computers that allow the central processing unit (CPU) to communicate with memory and input/output devices.

4.2 Requirements on the System

There were four major design requirements on the TLT. First, the input bandwidth had to be sufficient to accommodate the expected data rate, which is equal to the event rate times the event size, and protocol overhead. From the previous discussion on the design of the trigger and data acquisition system, a reasonable maximum for this was 100 Hz x 200 KBytes, or 20 MBytes/sec.

Second, the system had to have sufficient processing power to reach the requirement of reducing the second level rate of 100 Hz to an acceptable physics rate of about 5 Hz. Iterative

offline code that was eventually to be run online was timed on Monte Carlo generated events. It was estimated that the system should be able to provide several seconds of MicroVaxII equivalent processing time per event. A MicroVaxII was a standard computer in high energy physics at the time of the tests in the mid-1980's. It is rated at about 1.1 Mips† which leads to a total system computing power requirement of about 1000 Mips.

Third, it was desirable that the system provide a software environment which is easily accessible to the typical "offline user". The reason for this is that algorithms for finding and matching event elements, such as tracking, are central to the performance of the TLT. Since this code is a result of many man-years of software development in an offline environment, it would be wasteful for the TLT to embark on major conversion work or duplication of the existing and tested code. This requirement entails support of a full operating system so that the analysis code runs in the same environment both offline and online.

Finally, the system had to exhibit both hardware and software robustness, since it is a critical link in the experiment data acquisition chain. Because it is so important that a program crash or a hardware failure not prevent data taking, overall system robustness is best achieved through redundancy. Although increasing the number of hardware units increases the probability of a unit failure, it reduces the probability of a fatal *system* failure.

A large number of independent processors, known as a processor *farm*, with a parallel input stream naturally satisfies these requirements. The use of a farm as opposed to, for example, a mainframe, also permits a staged testing and installation programme without imposing an early commitment to one particular solution or incurring a high initial cash outlay. This flexibility is important in the rapidly changing computer industry.

4.3 System Architecture

The design consists of a processor farm reading data from six shared EVB/TLT VMEbus crates. The architecture at the individual crate level is shown in Figure 4.1. The component data flows via the EVB transputer links into a 512 KByte triple-ported memory (TPM) on the VME module labelled 2TP. This 2TP, or two transputer, module [102] has two INMOS T800 transputers connected by way of private ports to the TPM. The TPM also has a port connected to the VMEbus which allows the TLT to access the events. The Fermilab Branchbus [103] is used as a vertical bus to link the EVB/TLT VME crates to the TLT processors.

†. Mips stands for *million instructions per second.*

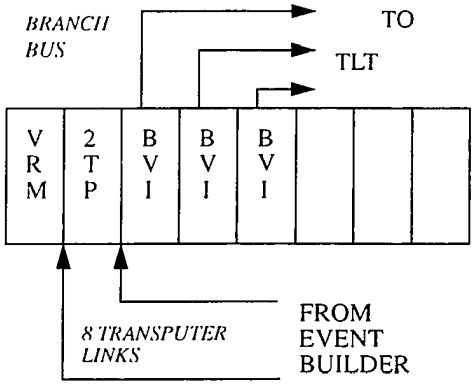

Figure 4.1: EVB/TLT VME crate.

The TPM is organized logically as a ring buffer. The EVB writes complete events contiguously into the memory commencing from the lowest address. Each event is preceded by two words; one gives the event size and the other is a status word. Once the first event is in the buffer, the TLT starts reading. The EVB can return to the starting address when it reaches the end of the memory because the TLT has been simultaneously reading the events. A number of memory words are reserved for the TLT and EVB to use as pointers to their locations in the buffer. This buffer organization gives the most efficient use of the available memory.

Each VME crate is read out by a *branch* of processors as shown in Figure 4.2. Physically, each branch is split into two Branchbus segments that are connected to the analyzing processors. A third segment is connected to a dedicated manager processor that manages the entire logical branch. Since read-modify-write cycles are not possible on the Branchbus, the manager handles the TPM ring buffer protocol, thus avoiding the use of a complicated semaphore for the analyzers. Each analyzer is assigned a starting address and an event size to read out by the manager process. The manager also handles any protocols with the EVB during run state transitions. For example, the TLT and the EVB handshake at run SETUP. If either fails to participate, an error message is sent to run control.

Triggered events are transported out of the TLT processors over the Branchbus and through a Fermilab Bus Switch to multiple destinations. The Bus Switch provides connectivity between any two Branchbus segments that are connected to it. It is a true crossbar switch which allows several

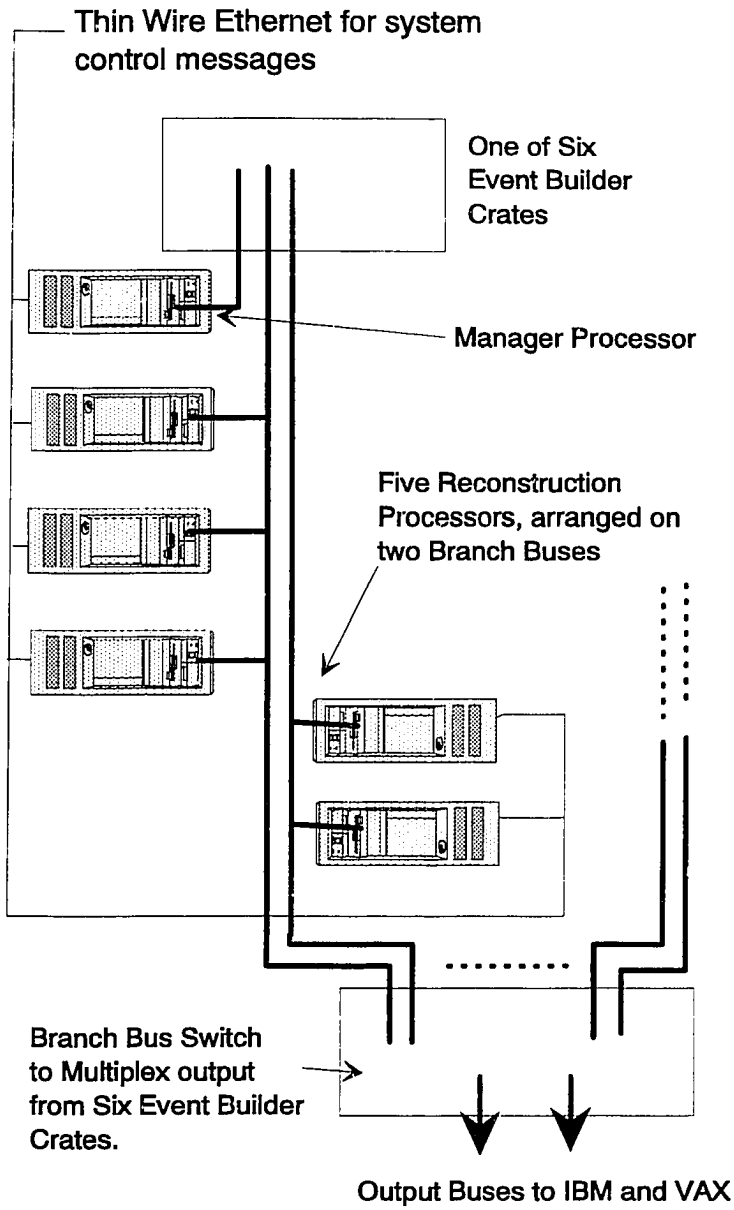

Figure 4.2: Schematic showing one branch of processors multiplexed to output.

simultaneous data paths. Processors on different Branchbus segments can be concurrently transferring data through the switch to the IBM 9000/720 mainframe for long term archiving, to local mass storage for short term archiving, and to the central data acquisition system VAX 8700 for small sample online data monitoring. Both the IBM and the VAX interfaces are based on VMEbus. The use of the Bus Switch also means that only one Branchbus connection, instead of twelve, is required in each of the output VME crates.

An important feature of the system is the separation of data and control busses. This simplifies the system and makes for more efficient data and control transfer. All transfer of event data within the TLT system takes place over the Branchbus segments connected to the analyzing processors. Control information is sent over a TLT thin-wire Ethernet segment and the dedicated Branchbus segments used by the branch managers to control the TPM buffers.

4.4 Data and Control Busses

4.4.1 Ethernet

Ethernet is a local area network technology that connects computer systems that are physically close. The maximum length of a single Ethernet is 1500 m. Standard Ethernet is a 50Ω coaxial cable about 1/2 inch in diameter. There is also a thin-wire Ethernet that uses standard RG-58C/U coaxial cable. This cable supports fewer connections and covers shorter distances than the standard Ethernet, but it is less expensive. Transceivers are used to convert the analog signals to digital form and vice-versa. Since all of the TLT computers are located together in a small area, thin-wire Ethernet was chosen because thick-wire would have been too bulky. Ethernet is a packet-switched network technology. This means that transmissions are divided into small packets that are multiplexed onto the Ethernet cable. The instantaneous bandwidth is 10 Mbits/sec.

There are about 200 computer systems connected by Ethernet in the ZEUS experimental hall. This has the advantage that any two computers can intercommunicate, however, the effective network bandwidth decreases rapidly as the number of communicating processes increases. Since the TLT generates a lot of internal messages, the TLT thin-wire Ethernet is isolated from the thick-wire segment in the experimental hall. This is accomplished by a *bridge*. This is a device that physically connects two separate wire segments and forwards packets from one network to the next. It contains logic that allows it to build up a table of the network addresses on each side of it. The bridge will then only forward those packets that are not local.

4.4.2 Branchbus

The Branchbus is a 32-bit data transfer bus that was developed at Fermilab. Blocks of data, up to a 256 KByte maximum, are transferred between a bus master and a bus slave. Pipelining is used so that more than one data word can be on the bus at a given instant. The Branchbus is multiplexed, meaning that it shares the same set of pins for address and data lines. Physically, the bus comprises two fifty conductor cables which carry differential signals; differential drivers and receivers which adhere to the RS485 standard are used. Each pair of signal lines is terminated with 120Ω. The maximum data transfer rate on the bus is 20 MBytes/sec, which is governed by a system clock that coordinates data transfers. Busses that use clocks are referred to as synchronous busses. On an asynchronous bus, such as VMEbus, cycle speed is set by the slowest participating module.

The Branchbus operates in master-slave mode, i.e., only one master at a time can access a slave. A transfer begins when a master executes an arbitration cycle. Each master has a different priority level (set by a dip switch). During the arbitration cycle, a master places its priority level on the bus and compares it against the level of any other masters which may be simultaneously requesting the bus. If a master wins the arbitration cycle, it executes a control cycle. In this cycle, two 32-bit control words are placed on the bus. They contain the Branchbus slave address, some control bits, the transfer count, and the starting VME address in the crate containing the Branchbus slave. If the slave acknowledges its address, the data cycle begins. Errors during the data transfer are signalled by the slave, e.g., a Branchbus parity error or a VMEbus error. A wait line is provided for cases in which the receiver is not able to keep up with the sender.

In the case of the TLT, the Branchbus master module is a VMEbus/Branchbus Controller (VBBC) [104]. This is a 6U VMEbus board inserted into a VME interface on the TLT processors. The Branchbus cables plug into two connectors on the VBBC front panel. The VBBC is a VMEbus slave and thereby allows the processors to become masters of the Branchbus. A transfer is initiated by checking and setting a BUSY bit in the control and status register (CSR) of the VBBC. The two Branchbus control words are then written into the VBBC data port. Finally, the transfer is started by setting either an input or output block transfer bit in the CSR. The CPU then reads from or writes to the data port of the VBBC.

The Branchbus slave module is a Branchbus/VMEbus Interface (BVI) [105] which functions as a protocol translator from the Branchbus to the VMEbus. BVIs are placed in the TLT/EVB and TLT output destination VME crates and act as VMEbus masters. They are capable of using all 32

VMEbus address lines (A32) or 24 lines (A24) for single or sequential transfers. In addition, they can handle 16 (D16) or 32 (D32) bit wide data transfers. These options are set in the control bits of the Branchbus control words. This feature is desirable since not all VME modules necessarily utilize all of the VMEbus data or address lines. If a BVI recognizes its address during the control cycle, it drives a slave connect line, thus allowing the master to start the transfer. A sixty-four longword FIFO is used for pipelining transfers.

An integral component of the TLT system is the Branchbus Bus Switch [106]. This is a sixteen port crossbar backplane housed in a standard 6U Eurocard cardcage which permits several concurrent data paths to run at the full 20 MBytes/sec each. Bus Switch Interface Boards (BSIB) provide the physical connection to the switch and translate the Branchbus RS485 signals to TTL Bus Switch signals as well as providing arbitration logic. Bus Switch arbitration gives equal priority to all BSIBs; requests for data paths are handled on a rotating basis. This is known as round robin arbitration. The switch is based on Texas Instruments crossbar chips and a programmable read only memory (PROM) containing routing information.

As an example of switch operation, consider the case of a TLT node outputting an event to the VME crate controlling the IBM output as shown in Figure 4.2. Once the VBBC has won the Branchbus arbitration cycle, it places the IBM crate's BVI address on the Branchbus during the control cycle. The BSIB converts this cycle into a Bus Switch arbitration cycle which is recognized by the switch arbiter. The map from the BVI address to the correct Bus Switch port, i.e., the correct BSIB, is provided by the routing PROM. If the path to the IBM crate is not in use, the switch arbiter arbitrates for it. The destination BSIB then executes the control cycle on its Branch Bus segment. When the BVI responds, the data transfer cycle through the switch may start.

4.5 The Processing Element

The TLT processing units are based on the MIPS R3000/R3010 RISC chip set [107]. RISC is an acronym for *reduced instruction set computer*. This is a computer architecture that was developed in the mid-1980's as an alternative to *complex instruction set computer* (CISC) architectures. In any processor, the time to achieve a given task is given by the product of the number of instructions required for the task, the number of cycles per instruction, and the time per cycle. Normally, an instruction can be broken down into several operations. In a typical CISC processor, the time required for the most simple operation dictates the cycle time. These

instructions generally require two to four cycles, whereas more complex instructions need on the order of seven to eight cycles.

The aim of the RISC architecture is to execute one *instruction* per machine cycle. This is achieved primarily through the use of instruction pipelines. As a simple example, suppose that every instruction comprises four operations and therefore requires four cycles. During the first cycle the instruction is fetched, during the second cycle there is a memory access, and so forth. A pipeline that holds four instructions and that executes a different operation from each instruction simultaneously could effectively achieve the goal of one instruction per cycle. During one cycle, the processor performs all four operations, albeit each belonging to a different instruction.

The pipeline architecture is most efficient if all instructions require the same number of operations. This can be approached by defining as simple an instruction set as possible†. Pipeline efficiency is improved further if each operation requires the same amount of time, since the cycle time is defined by the operation requiring the most time. Instructions that perform operations on operands in memory generally require more time than others. In the RISC instruction set, all operations are performed on operands that are in registers. Main memory is accessed only by specific load and store instructions. This is known as *load/store* architecture. There are special techniques for dealing with load instructions as well as branch instructions but they will not be dealt with here as only the general concept of RISC is important for this discussion.

The increased speed of RISC processors imposes stringent requirements upon the bandwidth between the memory and the processor unit. In particular, it must be high enough to deliver one instruction per cycle to the processor. Although, the load/store architecture alleviates the bandwidth requirements somewhat, other techniques are required. One of these is to use a relatively small amount of high speed memory to hold instructions and data that are frequently used. This memory is called *cache* memory. The bandwidth can be further improved by having separate data and instruction caches.

The problem with most of the techniques discussed above is that they tend to increase the number of instructions required per task. This is mitigated in RISC by optimizing compilers and providing support for operating systems. Although such techniques are not inherent to RISC processors and, in fact, were developed originally for CISC processors, the RISC architecture can utilize them more efficiently because of its streamlined instruction set.

---

†. This is what gave rise to the term "reduced instruction set".

In addition to reducing the processing time required for a given task, the architectural simplicity of RISC means that it can be implemented with fewer transistors than CISC architectures. This implies that it is easier for RISC to exploit new VLSI technologies.

The MIPS R3000/R3010 RISC chip set is the basis of the datastation 4D/35S from Silicon Graphics Incorporated (SGI). This datastation is the current TLT reconstruction processor. The clock runs at 36 MHz, which gives a processing power of 33 Mips. There are 64 KByte data and instruction caches, and 32 MBytes of RAM. A built-in SCSI port with a system disk of 200 MBytes is included in the enclosure. A single VME expansion slot allows the datastation to be integrated into a VME based system. The operating system is System V.3 UNIX with BSD and SGI enhancements.

A farm of thirty such processors satisfy the envisaged total CPU power requirement. The large amount of RAM is sufficient to hold the present analysis code which means that the processors do not waste time swapping code from the system disk to memory. The operating system supports interprocess communication via the TCP/IP protocol suite [108]. This feature is central to the implementation of the TLT control software, as discussed below.

Operating system features also proved very useful as a debugging tool. For instance, if there was a program crash while analyzing an event, the operating system would dump the analysis code and the event into a *core* file. The core file contains information about where the crash occurred as well as allowing the event in question to be extracted. It is then possible to run the analysis code offline in debug mode on the same event. This ability helped find coding bugs as well as identifying problems in the event structure. The operating system also allowed easy implementation of timeouts on the analysis code as protection against infinite loops. As a convenience, a user can login to any individual node and examine log files, or run diagnostics programs without having to first download them. The drawback to an operating system is that it occupies memory space and uses CPU cycles. The alternative is to download the only analysis image to the computing system. However, in this case, there is no information about program crashes.

A VBBC module resides in the 4D/35S VME expansion slot. It is controlled by a device driver that was adapted from a VBBC driver written at Fermilab. Events are read into a contiguous block of locked physical memory by setting up input transfers using the device driver. Data transfers to contiguous memory proceed faster than transfers to scattered locations.

4.6 Data Transfer Rates

Data transfer rate measurements have been made on all aspects of the system. Both the VBBC and the BVI can drive the Branchbus at 20 MBytes/sec. The bandwidth through the Bus Switch was measured by setting up several data paths. The sustained bandwidth for each path was determined to be 20 MBytes/sec, so that the maximum total bandwidth through the switch is equal to 20 MBytes/sec times the number of data paths, up to a maximum of eight.

The transfer rate from the TPM of the 2TP board over the VMEbus to the BVI is approximately 8 MBytes/sec. This is essentially limited by the TPM which does not respond to block transfer address modifiers. Therefore, the BVI has to release the VMEbus and initiate a new data transfer cycle after every longword transfer. Once the BVI receives the first dataword, it begins driving the Branchbus to send the data to the VBBC. However, the bandwidth from the VBBC into the locked RAM of the 4D/35S is only 2.5 MBytes/sec. The reason for this is that programmed input/output must be used from the data port of the VBBC over the internal input/output bus of the 4D/35S. Therefore, the BVI's 64 longword FIFO quickly fills up. Once this happens, the BVI empties its FIFO before rearbitrating for the VMEbus. If a second Branchbus/BVI combination is installed in the EVB crate, the second BVI can become the VMEbus master while the first is emptying its FIFO. This gives a potential bandwidth of 5 MBytes/sec per EVB crate and an aggregate rate over six crates of approximately 30 MBytes/sec.

In writing out data, one can take advantage of block writes. This, combined with the fact that fewer events are written out than read in, means that the outputting of events consumes little of the available bandwidth.

Data transfer to the IBM is over a 1.5 km high speed serial link fibre optic line. On the experiment side, the fibre optics are connected to a VME IBMlink module equipped with a direct memory access (DMA) controller and an on-board processor. (DMA controllers are specialized processors used for high speed data transfer. They relieve central processors of the tasks of incrementing addresses and keeping track of the transfer count.) TLT processors send accepted events through the Bus Switch to memory cards in the same crate as the IBMlink module. A dedicated SGI 4D/25S sets up DMA transfers from the memory buffers to the IBM. In order to accommodate interrupts from the IBMlink board, a CES vertical bus connects the 4D/25S to the VMEbus since the Branchbus does not have interrupt capabilities. Sustained transfer rates of about 1 MByte/sec are possible for event sizes larger than 100 KBytes.

The connection to the central data acquisition VAX 8700 is made via a CES VME board, the HVR 8217. It has a DMA controller and a daughter board which provides an interface to a DRB32 adaptor residing on the internal BI-Bus of the VAX. A TLT processor outputs events by sending data through the Bus Switch to VME memory and then initiating a DMA transfer to the DRB32. The bandwidth of the link exceeds 1 MByte/sec, which is certainly adequate for data quality monitoring purposes.

4.7 Control Software

The TLT control software was designed in formal manner using Structured Analysis and Structured Design (SASD) [109] software engineering techniques. In the analysis phase, the task of the system is defined and the different processes required to complete the task are proposed. These system specifications are rendered in a graphical and concise written form that is independent of the eventual implementation. Figure 4.3 is an example of a graphical specification. It is called a data flow diagram. The "bubbles" represent program units which can act on or transform data. Data stores are represented by the boxes while data flows are represented by the solid lines. The dotted lines indicate a transfer of control information.

This dataflow diagram is the top level TLT diagram. All external messages and datastreams must be on this diagram. For example, the TLT can receive events from the EVB, messages from run control, and requests for histograms and it is required to output accepted events. The basic processes necessary to deal with these tasks are also identified. For each process, there are lower level diagrams which specify the processes in more detail. All of the data flows, data elements, files, and processes are well defined in a *data dictionary*.

An essential part of the analysis phase for real-time systems is the specification of a state transition diagram. This defines the states of the processes and the conditions that can cause a change of state. The TLT state transition diagram is shown in Figure 4.4. For instance, the process Control_TLT in Figure 4.3 can receive a message from run control telling it to setup the TLT system for a run. It therefore changes from an IDLE state to a SETUP state and sends a message to Manage_Job instructing it to setup. If Control_TLT receives a message from Manage_Job that the setup was successful, it enters into the SETUP_IDLE state, otherwise it enters into an ERROR state. A well defined state transition diagram for the experiment and component run control systems is crucial for successful data acquisition.

The program modules and their interconnections are defined in the structured design phase

using structure charts. In addition, a short two or three sentence description in the vernacular of each module's functionality is given along with a brief pseudocode description of the module logic.

Teamwork [110], a computer aided software engineering tool, was used for all the analysis and design work. It not only allows one to easily draw the necessary diagrams, but also checks their logic to be sure there are no internal inconsistencies. The complete set of diagrams, charts,

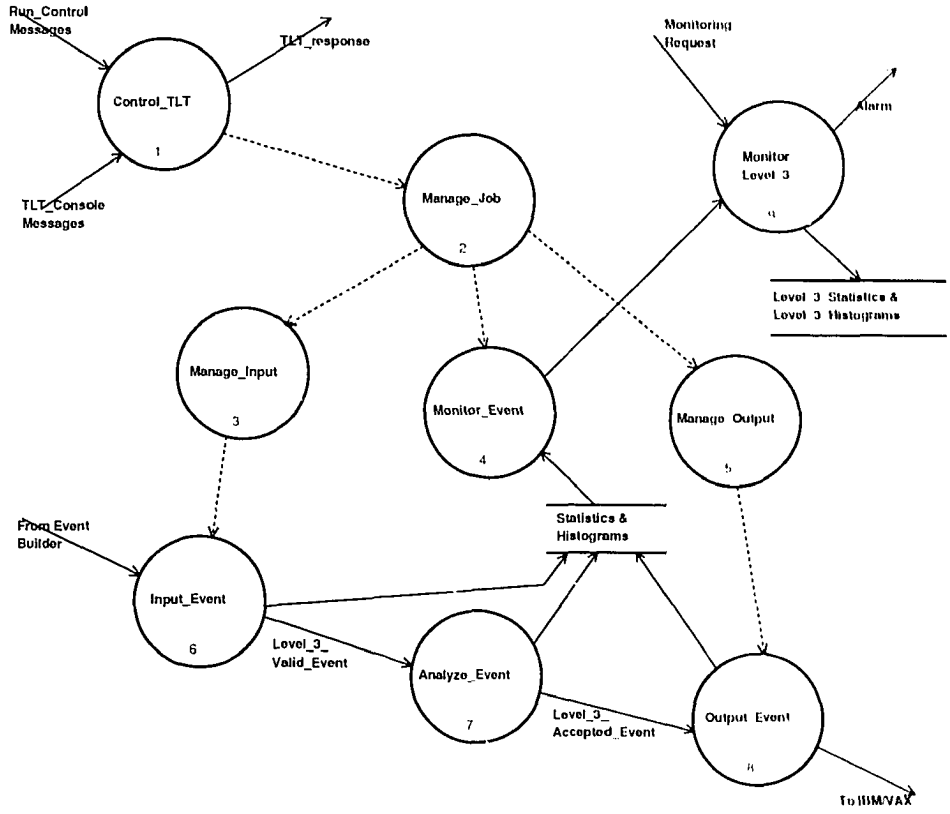

Figure 4.3: TLT top level data flow diagram.

module, and data definitions provides concise documentation of the system software.

The analysis and design resulted in a model that consists of several classes of cooperating processes all running on one physical processor or distributed over many pieces of hardware. This flexibility in task-to-processor mapping is extremely useful in the development environment where, generally, all the processes run on a single development machine. It also increases the robustness of the online system. For example, the process managing the TPM buffer could be run on an analysis node in the case of a hardware fault on the manager sub-branch.

The division of tasks into separate cooperating processes is advantageous for the software development environment, particularly in light of the fact that the analysis code must be developed offline. The input can be redirected to read from the online event stream or mass storage, depending on whether the running environment is online or offline. An analogous situation applies to outputting. The analysis code is interfaced then to the same software during both development and online running.

The model is implemented with an adaptation of the Fermilab Co-operative Process Software [111] which was developed by the Advanced Computing Project (ACP) group at Fermilab. The processes are divided into three broad classes: input management, output management, and analysis. Each class has a specific task and there may be multiple copies of a process in a given class.

The software to hardware mapping assigns to each logical branch of processors a single copy of the following processes. (They are all shown in Figure 4.3.) A job controller, Manage_Job, allocates hardware resources and communicates with the overall TLT supervisor process, Control_TLT. Each Manage_Job reads a system configuration file specifying how many copies of each process should be started and on which machines they should be run. It then starts up and synchronizes all of the analyzing and managing processes running on its branch. Manage_Job is also responsible for reporting errors to Control_TLT. An input supervisor, Manage_Input, initializes the EVB and VAX links, manages the TPM buffer protocol, and assigns events to analyzing processors that have placed themselves on an input queue. An output supervisor, Manage_Output, manages the writing of accepted events to the output destinations. A monitoring process, Monitor_Event, monitors the software and hardware performance at the crate level. It accumulates statistics on the branch and sends these at regular intervals to Monitor_Level_3. These processes are run together on the branch manager computer. This is an SGI 4D/25S since these processes do not require the computing power of a 4D/35S. Each 4D/35S processor runs a

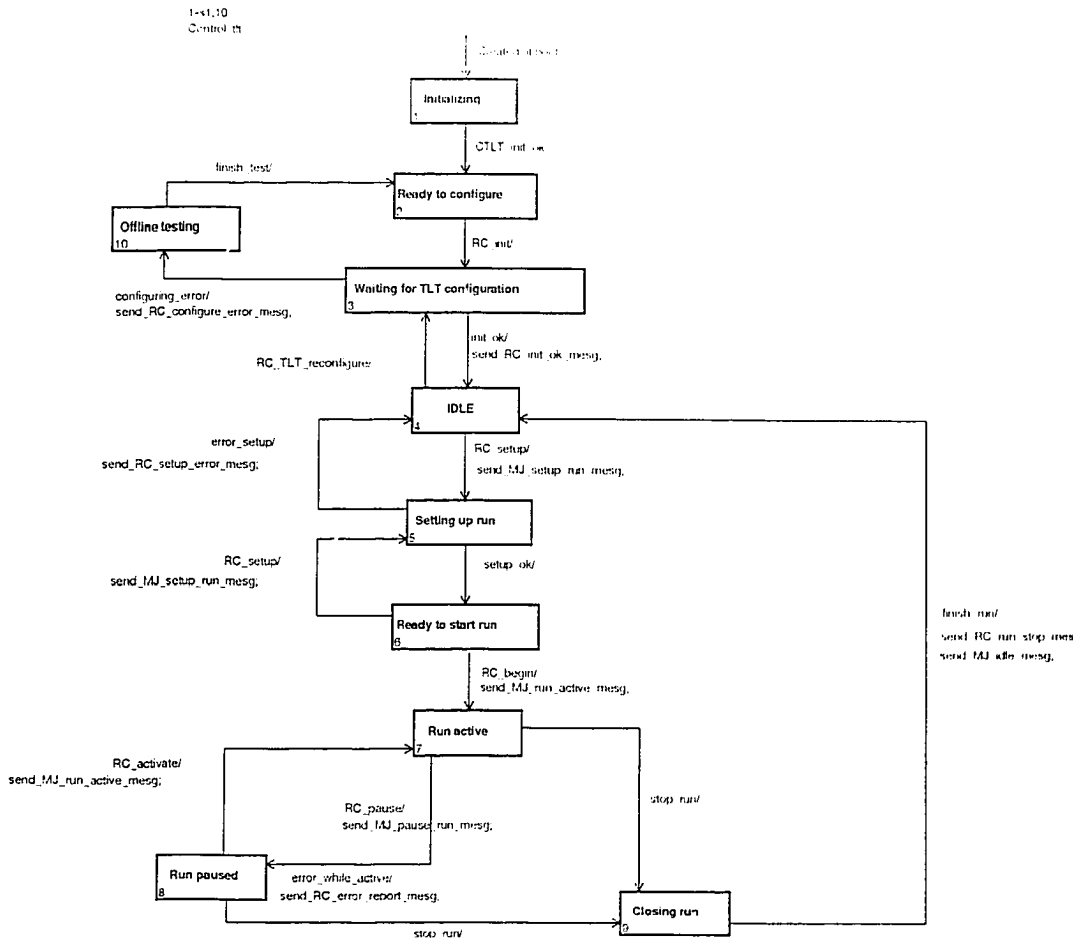

Figure 4.4: State transition diagram for the TLT.

copy of the analysis process, Analyze_Event.

The entire system is controlled by a TLT supervisor process, Control_TLT, and a global TLT monitor, Monitor_Level_3. These run on the TLT console, an SGI 4D/35G workstation. Control_TLT provides the communication link between the experiment run control or the console and the Manage_Job processes. Monitor_Level_3 collects statistics on the system performance and displays them on the workstation graphics monitor. This includes internal TLT statistics as well as histograms of quantities calculated by the analysis routines, such as the CAL timing histograms presented in Chapter 3.

TLT communication with the run control uses the Transmission Control Protocol (TCP) protocol, a reliable stream transport service [108]. This protocol requires that two communicating processes must first establish a connection before transmitting data. (In the ZEUS experiment, all the components communicating with run control must use the TCP protocol. Connections must be closed after each message is sent.) The TCP protocol guarantees that the packets of data arrive in the order in which they were sent and that there is no duplication or loss of data. This is done with a technique known as *positive acknowledgment with retransmission*. In this technique, the recipient transmits an acknowledgment to the sender each time it receives a data packet. If the sender does not receive an acknowledgment within a certain timeout period, it retransmits the packet. Duplication is avoided by assigning sequence numbers to packets and requiring senders and receivers to keep track of the sequence numbers of packets and acknowledgments. This data transfer protocol is essential for communication with run control as the entire data acquisition system would not be able to function if packets were lost, duplicated, or appeared out of sequence.

The disadvantage with the TCP protocol is that the sender and receiver must first establish a connection before a transmission and the sender must wait for packet acknowledgments from the receiver†. Furthermore, if the receiver or sender process dies, the TCP timeout period is 180 seconds. Such a delay would have the effect of introducing deadtime if the TLT input rate was high. A less time consuming protocol is the User Datagram Protocol (UDP). UDP is connectionless, it does not use acknowledgments to ensure that messages arrive, and it does not guarantee the order of messages. This protocol is used for internal message passing among the TLT processes because of its increased speed. This is particularly important for the requesting of events by Analyze_Event and the assigning of events by Manage_Input as this directly affects the

†. The TCP protocol actually uses a technique known as *sliding windows* that allows the sending of multiple packets before waiting for an acknowledgment. Nevertheless, there are still occasions when the sender must wait.

input bandwidth of the TLT. Provisions have been made in the control software to deal with lost messages and cases in which the ordering is important. Timing tests were performed to confirm that these provisions, in conjunction with the UDP protocol, were faster, and provided the same reliability, as the connected TCP protocol.

Both the UDP and TCP protocols can distinguish among multiple destinations on the same machine thereby allowing a number of processes to run on a single machine. This was useful for performing early tests at the University of Toronto before deciding to purchase several machines.

UNIX allows processes to use the UDP and TCP protocols through *sockets*. Processes can make system calls to open sockets, specify the desired protocol, bind the sockets to specific destinations, and send or receive data.

4.8 System Design Evolution

The original plans for the TLT system, developed circa 1986-1987, were slightly different from the implementation described above [112], [113]. The first proposal was a farm of VME based processor boards. The intended processor unit was a board developed by the ACP group and called the ACP-I. Each board has a Motorola MC68020 microprocessor running at 16.7 MHz, an MC68881 floating point processor, and 4 MBytes of memory. One hundred boards in six VME crates would have given a total of about 90 Mips of processing capability. The small amount of memory meant that it would have been impossible to run offline code or use an operating system, although a fairly rudimentary one was available. Nevertheless, code could be developed on a MicroVaxII host and written in FORTRAN77.

Events were to be distributed to the processors from a *single* EVB/TLT memory buffer via the Branchbus and its associated control modules. The sustained input bandwidth of this system was about 15 MBytes/sec. The TLT control computer was to have been a MicroVaxII. It could communicate with the VME crates via ACP modules that interface the MicroVax Q-bus with the Branchbus. Accepted events were to have been written out to a central data acquisition system VAX for online monitoring. The VAX was also meant to control the data transfer to the IBM. Event transfer to and from the farm would have taken place through the Bus Switch. It was recognized that the computing power and on-board memory of this system was inadequate [113], but work proceeded in order to gain experience with the VMEbus and Branchbus and to test the system architecture.

In late 1988 and early 1989 there was considerable uncertainty about the exact rate of beam-gas interactions. Estimates varied by over a factor of three, depending on assumptions about the vacuum

pressure, gas composition, and the design and setting of accelerator elements. As a result, a new architecture was proposed. A bus switch or series of switches could provide a direct connection between the component VME crates and the TLT crates. Extensive Monte Carlo studies at the University of Toronto using queuing theory showed that such a system could have a bandwidth in excess of 50 MBytes/sec and was stable against fluctuations in the event rate. An alternative solution, the present EVB transputer network with six TLT/EVB crates, was also put forward. After the ensuing "bus wars", the trigger and data acquisition group decided upon the transputer network architecture.

Around 1989 there were several more powerful candidate processor boards under development. One of these was the VME based ACP-II. It was to be based on the MIPS R3000 chip set running at a clock speed that corresponded to 20 Mips, have 8 MBytes of onboard memory extensible to 24 MBytes, and a full UNIX operating system. The development of this board was delayed and there was concern about future support. It was decided, therefore, to begin evaluating available commercial products. Because of market pressures, they are usually well supported and both the hardware and software are frequently upgraded.

A few manufacturers at this time had produced datastations that had VME interfaces. After a cost analysis and some field testing, the Silicon Graphics 4D/25S datastation was chosen. This machine has a processing power of about 16 Mips, 8 MBytes of RAM, and a VME interface with a bandwidth of 5 MBytes/sec for reads. It also runs the UNIX operating system and has an Ethernet interface and a system disk. Thus, it provided a familiar working environment as well as considerable flexibility. Each machine was fully independent and a user could login easily to any TLT processor.

It was also becoming clear that 8 MBytes of onboard memory would be insufficient as the size of the offline reconstruction code was considerably larger than initial projections. The increased size and complexity also meant that there were stronger processing requirements. These developments necessitated the upgrade of the processor unit to the SGI 4D/35S with its more powerful processor and potential for memory size increases. The drawback, however, was the slower VME interface.

4.9 Future Plans

Perhaps the most pressing concern of the system remains the issue of the input bandwidth since component estimates of the event size vary by more than a factor of three. It was decided in

1991 to develop a board that would couple the VBBC and the SGI VME interface to give the VBBC DMA master capabilities since the programmed input/output was the limiting factor in the bandwidth. This board, the VME DMA Extender (VDEXT), was developed and tested by the University of Toronto and Silicon Graphics.

The VDEXT is a 6U card which sits in the 4D/35S VME slot; the VBBC is inserted into the VDEXT. A block diagram of the VDEXT is shown in Figure 4.5. The 4D/35 VMEbus is the host VMEbus and the VBBC VMEbus is the local VMEbus. Block mode transfers of up to 256 bytes are possible. The address modifier code for the 4D/35S VMEbus is always set to block transfer mode. The modifier code for the local bus is programmable via the CSR on the VDEXT. In the case of multiple block transfers, the VDEXT rearbitrates for the 4D/35S VMEbus. This is necessary to prevent the CPU timing out on accesses to the internal bus during long DMA transfers.

Interrupts may be used to signal completion of the transfer or an error condition. Polling is possible, but this would slow the transfer since the CPU would be competing with the VDEXT for the VMEbus. Errors are also indicated in the CSR.

The boards have been produced and tested. They give a sustained rate of about 7 MBytes/sec for DMA transfers on the read cycle and 6 MBytes/sec on the write cycle. This gives a total input bandwidth of about 42 MBytes/sec. The use of two subbranches instead of one gives a marginal increase in performance because the maximum bandwidth from the 2TP TPM is about 8 MBytes/sec. The VDEXTs have been shipped to DESY, but it is not planned to install them until required.

More advanced plans include upgrading the processor unit to the SGI Indigo. This implies converting the TLT data bus from the Branchbus to a relatively new local area network technology called Fibre Distributed Data Interface (FDDI), since the Indigo only has an FDDI interface. The FDDI bandwidth is 10 MBytes/sec. The experiment also plans to eliminate the VAX 8700 used for online monitoring. Instead, events would be written out over an FDDI network to individual workstations.

4.10 System Performance

The TLT system, comprising thirty analyzing processors and six managing processors, has been in successful operation since the commencement of data taking in the spring of 1992. The modular design facilitated the installation and testing procedure. Along with the BMUON, GFLT, GSLT, and EVB, the TLT participated in the data acquisition system's first integration tests. These

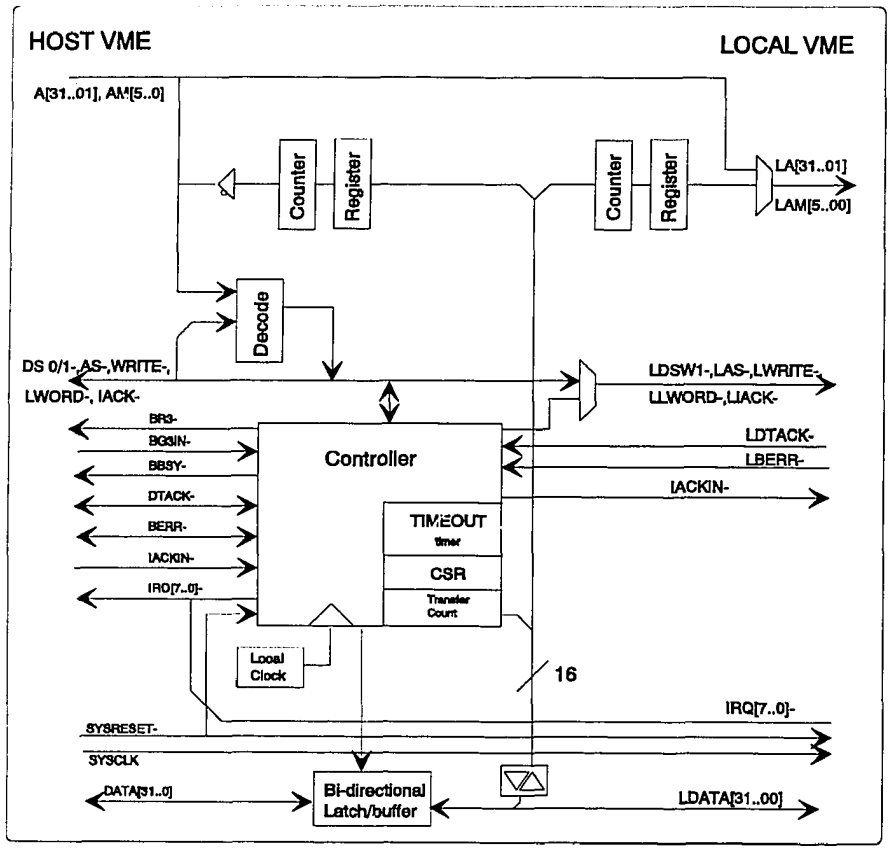

Figure 4.5: Block diagram of VDEXT controller. The host is the 4D/35S.

tests were important for testing and refining the run control sequencing and helped to ease the integration of other components into the data acquisition chain. During the 1992 running, the TLT input rate varied between 10 and 20 Hz. The typical event size was 150 KBytes. The output rate was about 5 Hz. HERA began operation with ninety bunches in 1993. This resulted in an input rate of about 60 to 70 Hz, while the output rate was about 4 Hz. The event size is slightly smaller, about 100 KBytes. The system was easily able to handle this rate without introducing deadtime. As HERA progresses to two hundred bunch operation, the input rate will not scale from the current rate because more stringent triggers will be implemented at the first and second levels.

The system hardware and control software is quite reliable and stable. In 1992, two ACP VME modules and two computer fan units failed and had to be replaced. It was also discovered that not *all* VME modules fully adhere to the VME specification. In particular, the relative position of some of the modules in the IBMlink crate was found to be critical. During the 1993 run, which lasted about eight months, hardware problems occurred at a rate of about one per month. The most common occurrence was a blown fuse in an ACP VME module. This failure rate is certainly acceptable and, because of the redundancy of the system hardware, these failures do not affect data taking. During this period, 40×10^6 second level triggers were processed and 4×10^6 events were written to the IBM.

The control software required only minor changes as a result of experience from the 1992 run. Most of these were related to providing clearer messages to the shift crew. There were also some changes to the experiment run control sequencing which, of course, necessitated changes for the components. No major design changes were required, which is remarkable considering the complexity of the system and the flexibility required of it. This can be attributed to careful software engineering.

Compilation and linking times for the analysis software were generally on the order of ten minutes or less on a 4D/35S development machine. The executable is about 32 MBytes and is distributed to the thirty analyzer nodes over ethernet. The distribution takes about ten minutes. The mean analysis time is about 250 ms, most of which is spent on pattern recognition.

Unlike third level triggers in most experiments, the TLT has been an important component to the trigger and data acquisition system from the start of running. For example, it was not foreseen to have to reject sparks in the trigger system. Since spark rejection requires knowledge about individual PMTs as well as global information, it is not possible at the first level trigger and is non-trivial to implement at the second level. The principal reasons for the TLT's adaptability is the access to all of the component and trigger system data, and the familiar software environment. Trigger algorithms are coded in FORTRAN and act on the same event elements as the offline reconstruction code. This

allows for easy offline independent checks of the trigger. This flexibility was very important for adapting to conditions that were unforeseen.

Chapter 5

Kinematics and Event Selection

5.1 Kinematics at HERA

The data studied in this thesis comes from the neutral current, deep-inelastic scattering reaction

$$ep \rightarrow e + \text{hadrons}. \tag{5.1}$$

Neutral current means that the exchanged boson can be either a photon or a Z^0 boson. The centre-of-mass energy is given by $\sqrt{s} = \sqrt{4E_eE_p} = 296$ GeV, where particle masses have been neglected. In lowest order (QPM), the deep-inelastic scattering process is just the interaction of the electroweak current with one of the quarks from the incoming proton which, after hadronization, gives rise to a *current jet*. The rest of the proton forms the target remnant. Although the basic properties of the final state hadronic system are given by this interaction, the detailed properties reflect higher order QCD effects.

The event kinematics are characterized by Q^2, the negative of the four-momentum transfer, and the scaling variable, x. Use will also be made of the variable y, although only two variables are necessary to specify the kinematics. The x - Q^2 dependence of the angle and energy of the scattered electron and the current jet is shown in Figure 5.1. These quantities are conventionally calculated in the laboratory frame from the energies of the incoming electron (E_e) and proton (E_p), the energy of the scattered electron (E'_e), and the electron scattering angle (θ_e), viz.,

$$Q_e^2 = 2E_eE'_e(1+\cos\theta_e) \tag{5.2}$$

$$x_e = \frac{E_e}{E_p}\frac{E'_e(1+\cos\theta_e)}{2E_e - E_e'(1-\cos\theta_e)}. \tag{5.3}$$

The variable y can then be calculated through the relationship

$$Q^2 = xys. \tag{5.4}$$

While the Q^2 reconstruction is accurate with this method, the accuracy of the x determination

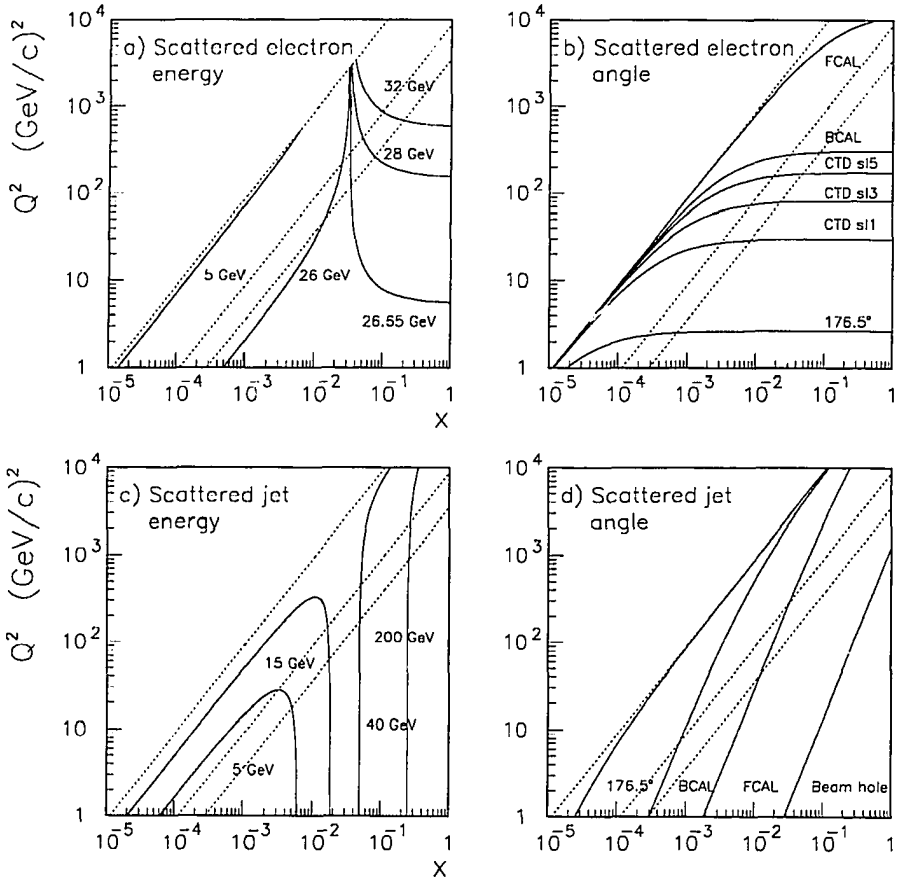

Figure 5.1: The x - Q^2 dependence of the angle and energy of the scattered electron and the current jet.

is poor. This is particularly true at low values of y (or high values of x) [114] since $\left.\frac{\partial x}{x}\right|_{E'} = \frac{1}{y}\frac{dE'}{E'}$. This can be seen graphically in Figure 5.1(a-b). A good measurement of Q^2 can be obtained from the measurement of θ_e, but this yields practically no information on the value of x at low Q^2 values. As an example, suppose Q^2 was determined to be approximately 10 GeV^2 from θ_e, and E_e' was measured to be 26.7 GeV when the true value was 26 GeV. Then the measurement of x would be too high by almost an order of magnitude. The physical reason for this sensitivity to x can be understood within the framework of the QPM in which the energy and momentum of the parton with which the electron interacts is given by the product of x times the momentum of the proton. The parton and electron momenta are equal at $x = 26.7/820 = 0.03$. Since the proton momentum is much larger than the electron momentum, a small change in x about this value has a large effect on the relative momentum of the parton and the electron.

At HERA, the hadronic final state can also be used to determine the event kinematics through calorimetric measurements. Indeed, this is the only possibility for charged current events in which the exchanged boson is a $W^{\pm}$ and the scattered lepton is a neutrino. A procedure was proposed by Jacquet and Blondel that does not require any jet algorithm or hypotheses about the proton structure [115]. In this method, y and Q^2 are expressed in terms of laboratory variables using energy-momentum conservation:

$$y_{JB} = \frac{\sum (E_i - p_{z_i})}{2E_e} \tag{5.5}$$

$$Q^2_{JB} = \frac{\left(\sum p_{x_i}\right)^2 + \left(\sum p_{y_i}\right)^2}{1 - y_{JB}}, \tag{5.6}$$

where p_x and p_y are the transverse momentum components of the particles making up the final state hadronic system, p_z is the longitudinal component, and E is the energy. The variable x is then obtained from Equation (5.4). The noteworthy feature about (5.5) and (5.6) is that hadrons emitted in the very forward direction, which are not detected because of the beampipe, generally give a small contribution to the sums. The reconstructed y and Q^2 values are, on average, lower than the true values. As with the electron method, the Jacquet-Blondel method is not accurate over all regions of phase space. In particular, it is poor at the reconstruction of Q^2 because of the quadratic dependence on the transverse momentum.

Alternatively, a combination of both the final state electron and hadronic system can be utilized. In the so-called double angle method [116], the kinematical variables are measured using the angle of the scattered electron and an angle that characterizes the hadronic final state, γ_h. In

the QPM with massless partons, γ_h would be the laboratory angle of the final state quark. The value of this angle is determined by four-momentum conservation and can be calculated from the transverse and longitudinal energy flow of the hadronic system as

$$\cos\gamma_h = \frac{(\sum p_{x_i})^2 + (\sum p_{y_i})^2 - (\sum (E_i - p_{z_i}))^2}{(\sum p_{x_i})^2 + (\sum p_{y_i})^2 + (\sum (E_i - p_{z_i}))^2}, \tag{5.7}$$

where the sums run over all observed final state hadrons. The physical significance of γ_h becomes more evident if Equation (5.7) is expanded. Neglecting the current jet mass and the transverse momentum of the proton remnant, one has

$$\cos\gamma_h = \frac{\sum E_i \cos\gamma_i}{\sum E_i}, \tag{5.8}$$

where the sums are over all the particles in the current jet. The cosine of γ_h is therefore the energy weighted average of the cosines of the particles in the current jet.

In calculating γ_h, the sum over particles is replaced by the sum over calorimeter energy deposits: E is now the energy measured in a calorimeter cell and p_x, p_y, and p_z are the cell energies multiplied by the appropriate angular factors. As with the Jacquet-Blondel method, particles lost in the forward beam pipe give a small contribution to the above sum. The kinematical variables are given in terms of γ_h and θ by

$$Q^2_{DA} = 4E_e^2 \frac{\sin\gamma_h (1 + \cos\theta_e)}{\sin\gamma_h + \sin\theta_e - \sin(\theta_e + \gamma_h)} \tag{5.9}$$

$$x_{DA} = \left(\frac{E_e}{E_p}\right)\left(\frac{\sin\gamma_h + \sin\theta_e + \sin(\theta_e + \gamma_h)}{\sin\gamma_h + \sin\theta_e - \sin(\theta_e + \gamma_h)}\right). \tag{5.10}$$

5.2 Vertex Determination

The event vertex is used for the calculation of angular variables. At least two well measured tracks, and a reduced chi-squared less than ten for the subsequent vertex fit, were required to define a valid event vertex in z; otherwise it was set to zero. The resolution in the z-position with the 1992 readout is estimated to be 4.5 cm. This was determined from a Monte Carlo event sample by comparing the reconstructed vertex with the generated vertex. Since the vertex resolution in the x and y coordinates was worse than the beam spread, these coordinates always were set to zero.

5.3 Electron Identification

Electron identification is required for tagging events as neutral current candidates. In this thesis, it is based solely on calorimeter information. Electrons generate electromagnetic showers, which have smaller lateral and longitudinal spreads in energy deposition than hadronic showers. Furthermore, electrons are generally well isolated as they are back-to-back in the azimuth with the hadronic system. However, as is shown in Figure 5.1, this is not the case at very high y, where the electron and current jet are both very forward in FCAL, and very low y where they are both in RCAL. Electron identification is more difficult in the very forward and backward regions where the azimuthal angle is not well defined. There were several algorithms developed within ZEUS, but only ELECT, the algorithm used for this analysis, is described.

ELECT begins by considering EMC cells with an energy greater than 1 GeV as possible electron candidates. This value was chosen since even low energy electrons of a few GeV will deposit most of their energy in a single EMC cell. (Recall from Chapter 3 that $2\rho_M$ is about 4 cm for uranium and the transverse EMC cell dimensions in RCAL are $10 \times 20\ cm^2$.) If two such cells are within 12° of each other, the cell with the highest energy is taken. For each candidate, the probability to be an electron is based on the energy weighted mean radius of the EMC energy within an inner cone of 5.7°. Since electromagnetic showers are usually contained longitudinally within the EMC section, ELECT also considers the EMC energy and the ratio of HAC to EMC energy in an outer cone. The energy of the electron candidates is given by summing all of the energy within an outer cone of 11.5°. The cone sizes were determined by tuning the algorithm with Monte Carlo events. The increase in the longitudinal spread of the shower when the electron impinges on the cracks between the CAL modules and the increase in the lateral spread caused by preshowering in the inactive material in front of the CAL is taken into account. If there was more than one candidate with a reasonable probability of being an electron, then the candidate with the highest transverse momentum was chosen as this gave the highest purity.

Position reconstruction algorithms are common to all electron finders. The HES was used to tune the RCAL position reconstruction algorithm because the size of the diodes is much smaller than the EMC cell size. Approximately one third of the scattered electrons traversed the HES plane. Since the BCAL was not instrumented with diodes, the BCAL position finding algorithm was tuned from test beam data.

The y-coordinate of the electron impact point on the face of the CAL is determined from the distribution of energy in the vertically adjacent cells contributing to the electron cluster. It is a

function of $\frac{E_1}{E_1+E_2}$, where E_1 is the energy of the EMC cell with the maximum energy among the cells contributing to the electron cluster, and E_2 is the energy of the cell with the highest energy above or below the cell with the maximum energy. The x-coordinate is determined from the signal balance between the left and right readouts of the cell with the maximum energy. It is a function of $\frac{E_{left}-E_{right}}{E_{left}+E_{right}}$. For the RCAL, Monte Carlo studies showed that the position resolution in x is about 1.2 cm, while that in y varies between 0.4 cm and 1.2 cm, depending on the position of the electron. This corresponds to an average resolution in polar angle of 0.3°.

5.4 Event Selection

Events were recorded using the three level trigger and data acquisition system that was outlined in Chapter 3. The total integrated luminosity was about 30 nb^{-1} and approximately 4.3×10^6 triggers were collected. There are considerably more triggers than deep-inelastic scattering events since the trigger criteria are not designed to be as stringent as possible. One reason is that HERA is the first collider of its type and, *a priori*, one cannot be certain of the nature of the physics and background events. Furthermore, it is inexpedient to apply rigorous cuts until experience has been gained with detector and trigger system operation.

All of the collected triggers were subsequently processed with the ZEUS offline reconstruction programs. After reconstruction, the data was passed through filter programs designed to select neutral current candidates and to remove cosmic ray and beam halo muon background events.

The first stage of the filter programs selected events that had an EMC trigger in the RCAL or BCAL since scattered electrons should cause such triggers. Algorithms based on the topology of cells in the calorimeter were then used to reject cosmic rays and beam halo muons. More rigorous spark and timing algorithms than used online were also applied. In particular, the times were calculated as energy weighted means according to Equations (3.12) and (3.13). The events remaining after these filters had timing consistent with events having vertices in the interaction region of the detector and are not visually obvious background such as sparks or cosmic rays. They comprise deep-inelastic scattering, *diffractive*, and *photoproduction* events as well as electron and proton beam-gas events that originated inside the detector system.

In photoproduction, Q^2 is almost zero so that the exchanged photon is quasi-real. The high centre-of-mass energy means that there can be a hard scattering between the photon and the partons in the proton that gives rise to a hadronic final state. The electron scatters through a small

angle and does not enter into the active volume of the detector. Photoproduction is a source of background to deep-inelastic scattering because a photon or charged pion from the hadronic final state may be misidentified as a scattered electron.

A useful variable that distinguishes deep-inelastic scattering events from photoproduction and proton beam-gas events is the quantity δ defined by

$$\delta = \sum E_i (1 - \cos\theta_i), \tag{5.11}$$

where the sum runs over all measured particles. For events where all final state particles are perfectly measured, conservation of energy and momentum implies that $\delta = 2E_e = 53.4$ GeV. Different final states produce different δ distributions since not all final state particles are detected, so that it is a good discriminator against background processes.

In deep-inelastic scattering, the scattered electron and the hadronic final state are both measured. Undetected particles which are emitted down the forward beam pipe give a negligible loss. Initial state radiation, which effectively reduces the energy of the incoming electron, moves events to lower values and measurement errors lead to a broadening of the distribution.

In photoproduction, however, the electron is scattered at a low angle and does not enter into the detector. Since the cosine of its angle is essentially -1, the electron has a potentially large contribution to the sum in Equation (5.11) that is not included. Therefore, photoproduction events predominantly give low values of δ. The same is true for proton beam-gas events since the electron is not scattered at all. An initial cut on these background events was made by requiring $\delta + 2E_\gamma > 25$ GeV, where E_γ is the energy measured in the luminosity detector photon calorimeter. Because the contribution from initial state photons is added to δ, this initial cut does not remove radiative events. In calculating δ, the sum in (5.11) runs over all calorimeter cells, E is the measured energy of the cell and θ is its polar angle with respect to the incident proton beam. At this point, the preselected sample contained about 2×10^4 events.

After these initial cuts that were common for all deep-inelastic scattering studies within ZEUS, the following specific requirements were made for the study presented in this thesis. In order to tag an event as a neutral current candidate it is imperative to identify an isolated electron. Figure 5.2 shows the Monte Carlo estimate of the efficiency and purity of the electron finder in the Q^2-x plane. The efficiency is defined as the number of correctly identified scattered beam electrons divided by the true number of scattered electrons. The purity is number of correctly identified electrons divided by the number of found electrons. The values were determined from a Monte

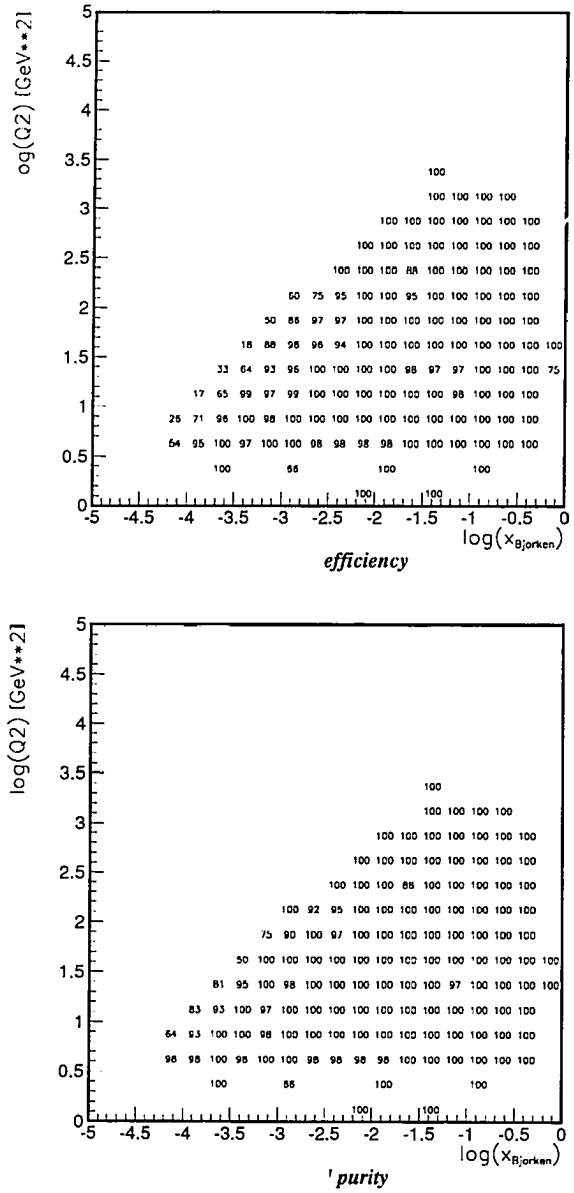

Figure 5.2: Efficiency and purity (in percent) of ELECT in the Q^2-x plane.

Carlo event sample in which one has complete knowledge of all generated electrons. The sample was passed through the filter programs and the δ cut. The efficiency and the purity are near 100% over most of the kinematic plane. The exception is along the 45° angle demarcating the kinematically allowed region. As shown in Figure 5.1, this corresponds to very low energy scattered electrons and so events were demanded to have an isolated electron of energy greater than 5 GeV.

Because the scattered electron energy and position measurements can be degraded by the partial loss of the electromagnetic shower into the RCAL beampipe, it is desirable to put a fiducial cut on the impact point of the electron. As can be seen from Figure 5.1(b), this can be effected by a minimum Q^2 requirement. It was required that $Q^2_{DA} > 10$ GeV^2, which roughly corresponds to a requirement that the scattering angle be less than 173°.

To remove most of the remaining background from photoproduction events and proton beam-gas events that originated inside the detector system, it was required that 35 GeV $< \delta <$ 60 GeV. Since any energy in the luminosity photon calorimeter was not summed, this cut also removed deep-inelastic scattering events coming from electrons that have emitted an energetic initial state photon.

The discrimination between deep-inelastic scattering and photoproduction is evident in Figure 5.3. The δ distribution for Monte Carlo generated photoproduction events before the electron energy requirement is shown as the dashed histogram. It is clearly centered at a δ value much lower than 53.4 GeV. The histogram with the solid line shows the same distribution for Monte Carlo generated deep-inelastic scattering events. This distribution is centered at twice the nominal incident electron energy but has a long tail that is attributable to radiative events. The photoproduction events which survive the 5 GeV electron cut are shown as the solid histogram and the deep-inelastic scattering events are shown as the shaded histogram. It can be seen that the electron cut and the δ cut at 35 GeV remove most of the photoproduction events but there is still some contamination. This will be discussed further in Chapter 6.

After these cuts and requirements, the remaining sources of background to deep-inelastic scattering events are interactions of the electron beam with the residual gas in the beam-pipe and diffractive scattering. It is possible to distinguish the background from the deep-inelastic scattering by the energy deposit in the forward region. The deep-inelastic scattering interaction of an electron with a quasi-free parton in the proton results in the disintegration of the proton. This gives an energy deposit in the FCAL around the forward beampipe. In diffractive scattering [117],

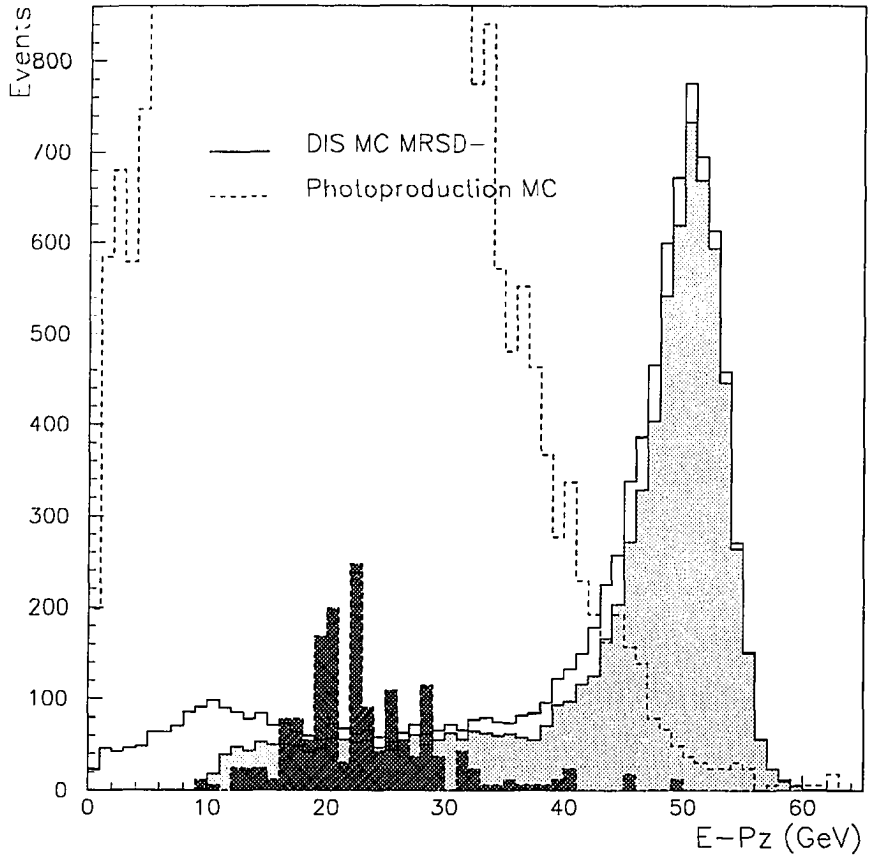

Figure 5.3: The δ distributions for photoproduction and deep-inelastic scattering Monte Carlo generated events. The dashed histogram shows the photoproduction events before the 5 GeV electron energy requirement. The same distribution for the deep-inelastic scattering events is shown as the histogram with the solid line. The solid histogram shows the photoproduction events and the shaded histogram the deep-inelastic events after the electron requirement.

on the other hand, the proton remains intact or is excited to a resonance state and does not disintegrate. Electron beam induced background events also deposit most of their energy in the RCAL or BCAL and very little energy in the FCAL since the electrons are moving in the negative z direction. This was verified by studying the events originating from the electron pilot bunch. It was thus required that the energy in the FCAL had to be greater than 1 GeV.

The above cuts define a deep-inelastic scattering event sample. However, since energy flow distributions are studied in Chapter 6 as a function of the kinematical variables, it is necessary to check that these variables can be reconstructed with reasonable accuracy. The reconstruction of kinematical variables has measurement errors introduced by CAL noise. Figure 5.4 shows HAC1/2 and EMC cell noise spectra that were obtained from random trigger runs. Cell energies can have negative values because the DSPs subtract the pedestals. If no cell energy cut is applied and the calibration is perfect, then on average there is no energy offset in randomly triggered events. However, the r.m.s. values of the cell noise spectra show that there is an event-to-event fluctuation with a width of about 2 GeV. (There are 3263 EMC cells and 2268 HAC1/2 cells.) The event-to-event variation can be reduced by applying a cell energy cut, but this also has the effect of introducing an energy offset due to noise. For example, if cell energy cuts of one times the r.m.s. width of the respective cell noise spectra are applied, there would be an unacceptable noise offset of about 27 GeV, but the event-to-event variation would decrease to 1.4 GeV. Both the noise offset and the event-to-event variation decrease as the cell energy cut is increased. At the same time, increasing the cut removes physics information. The cell energy cuts were made about four times the r.m.s. width of the cell noise spectra, which corresponds to 60 MeV for EMC cells and 100 MeV for HAC cells. This implies an energy offset of 0.45 GeV with an r.m.s. width of 0.2 GeV. About 0.2% of the EMC cells and 0.05% of the HAC cells have noise exceeding the cell energy cuts.

The influence that the noise has on the kinematical variables is best illustrated by y_{JB}, since it is directly calculated from the total energy: it gives an artificial y_{JB} of 0.006 with a width of 0.003. The effects of this are shown in figure 5.5, which is a scatter plot of the reconstructed y_{JB} vs. the generated y_{JB}. The Monte Carlo events have CAL noise simulated and the cell energy cuts have been applied. The low y region is the most sensitive to the CAL noise. This can be understood physically by noting that low y corresponds to high x. Consequently, the current jet is close to the beam pipe and gives a small contribution to the numerator in Equation (5.5). Noise in the central or rear regions of the CAL, however, has a small or negative p_z and can have a relatively large contribution to the numerator. Since the points on the scatter plot begin to deviate from a diagonal

line below a y_{JB} of about 0.02, it was required that $y_{JB} > 0.02$.

In the following chapter, the data and Monte Carlo predictions are plotted in three different x bins: $x < 10^{-3}$, $10^{-3} < x < 10^{-2}$, and $x > 10^{-2}$. As an estimate of the quality of the x reconstruction,

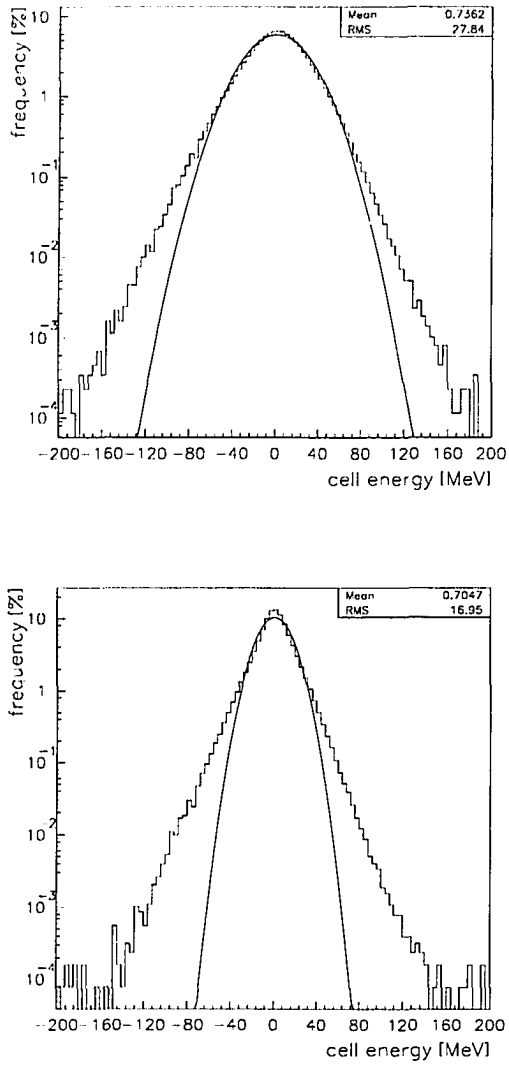

Figure 5.4: Cell noise spectra. Top figure is HAC cells and bottom figure is EMC cells.

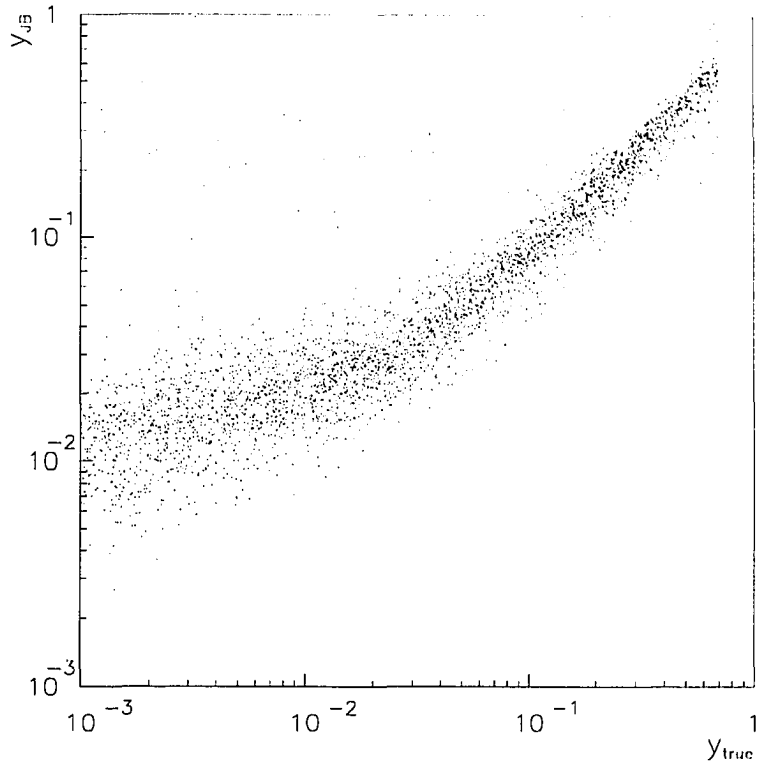

Figure 5.5: Reconstructed y_{JB} vs. generated, or true, y_{JB} for Monte Carlo generated events. Noise has been simulated and cell energy cuts have been applied.

Figure 5.6(a) shows a scatter plot of the generated x and the reconstructed x_{DA} from a Monte Carlo simulation. The selection criteria are exactly as described above with the exception of a more relaxed y_{JB} cut: 0.01 instead of 0.02. There is a good correlation except at high x values. Figure 5.6(b) shows the same correlation, but now with the y_{JB} cut of 0.02. There is a noticeable improvement in the correlation at large x values. The relative resolution in x, $\sigma(x)/x$, is approximately 30% for $x = 10^{-2}$, 60% for $x = 10^{-3}$, and 80% for $x = 5\times10^{-4}$. It varies smoothly with x. The relative resolution in Q^2 is about 25% and is roughly independent of Q^2 [118].

A sample of 2444 events satisfied these selections, of which approximately 70% had a

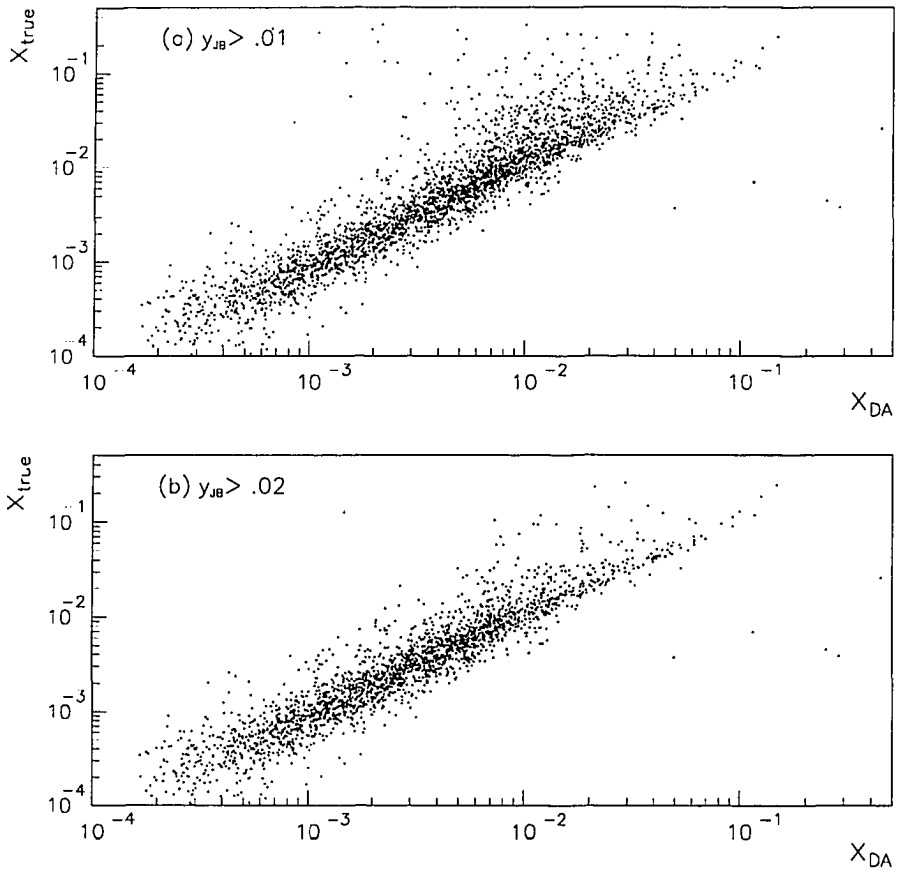

Figure 5.6: The true, or generated, value of the variable x vs. the reconstructed value for two different values of a y_{JB} cut. All other cuts are as described in the text.

reconstructed vertex. The reconstructed vertex distributions for the data and for a Monte Carlo event sample are shown in Figure 5.7. There is reasonable agreement between the data and the Monte Carlo. The data vertex distribution is not centered at zero because the efficiency for finding a vertex increases as the interaction moves towards RCAL. This is due to the increased acceptance in the CTD of particles from the proton remnant jet. All of the measured vertices are within the z range covered by the CTD.

The beam bunch crossing numbers of all the selected events were checked. None of the events had bunch crossing numbers which corresponded to the electron or proton pilot bunches. A sample of 840 selected events were visually inspected to check the purity of the sample. A total of eleven events, approximately 1%, were identified as contamination from cosmic ray interactions and other obvious background sources. These events were removed from the data sample. The effect of the residual background from photoproduction reactions is small, as discussed later, and does not affect the conclusions.

The event samples generated by the Monte Carlo methods were processed with the ZEUS detector simulation program, the trigger simulation and the offline reconstruction procedure. They were then subjected to the same selection procedure applied to the data. Table 5.1 shows the

Sample	Number of Events
Data	2400
PS(W^2)	1300
PS(Q^2)	2100
PS(Q^2(1-x))	2600
ME	1200
ME+PS	3600
CDM	1300
CDM+BGF	1300
HERWIG	2200
HERWIG+SUE	3100

Table 5.1: List of event samples and approximate number of events that satisfied the event selection criteria.

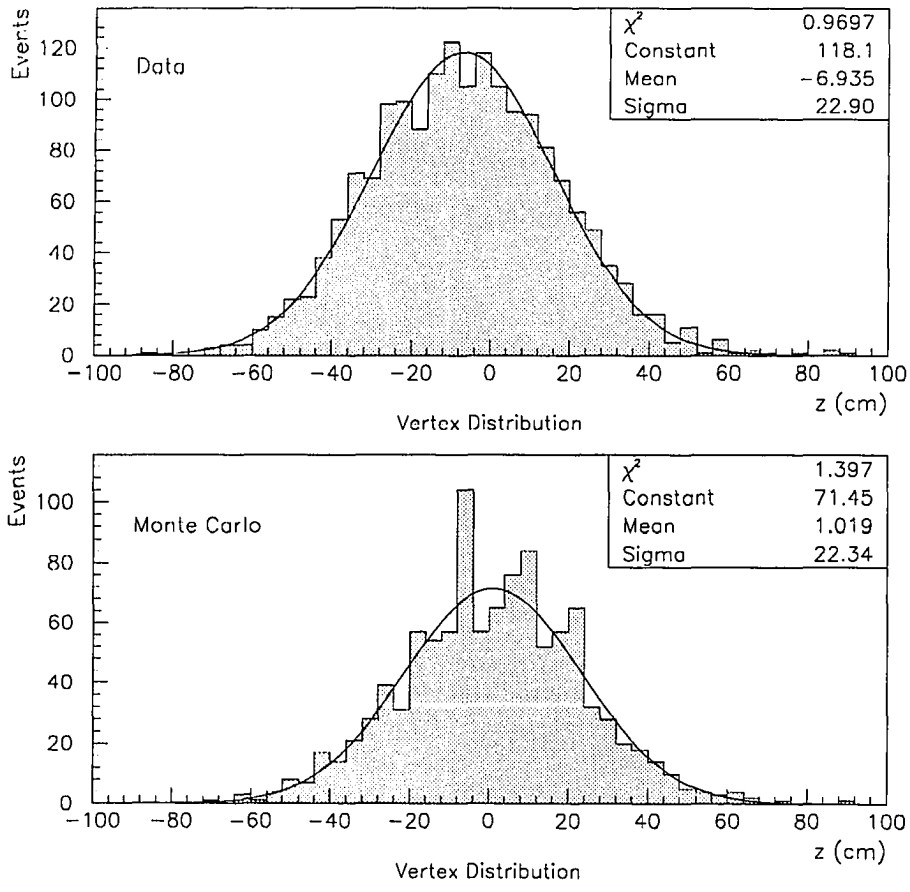

Figure 5.7: Vertex distributions for data sample and a Monte Carlo (colour dipole model plus radiative corrections) sample. It is required that more than one track contribute to the vertex and that the reduced chi-squared of the vertex fit be less than ten.

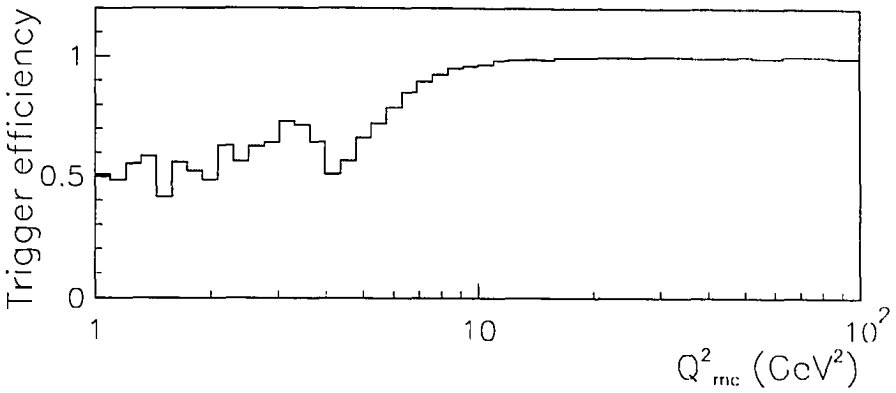

Figure 5.8: The CAL first level trigger efficiency as a function of Q^2.

approximate number of events that satisfied the selection criteria for the data and each of the models. A summary of the models is provided in Table 2.3 and they are discussed in the second part of Chapter 2.

5.5 Trigger Acceptance

The trigger acceptance for neutral current events is estimated by examining the trigger bits in Monte Carlo events. The CAL first level trigger acceptance as a function of Q^2 is shown in Figure 5.8. The acceptance increases with increasing Q^2 up to about 8 GeV^2 after which it becomes flat. It is desirable to choose a kinematical region in which the acceptance is flat, or at least not rapidly changing, in order to minimize any systematic error on the acceptance. This was another motivation for demanding that Q^2 be greater than 10 GeV^2 in order to avoid any systematic error. The trigger acceptance is flat in x. This kinematical dependence is partly due to the fact that a component of the trigger is based upon finding a scattered electron. For fixed x, the scattered electron is further removed from the beampipe as Q^2 increases, whereas the scattering angle has little x dependence. This can be seen in Figure 5.1(b). For $x > 3\times10^{-4}$ and $Q^2 > 8$ GeV^2 the trigger acceptance exceeds 97.5% [119]. The acceptance was checked for events subjected to the above selection cuts and was found to be greater than 99%.

It is necessary to continuously check the performance of the trigger hardware to ensure that

the trigger simulation accurately represents the hardware. The efficiency of the trigger hardware was monitored with selected data samples and with charge injection into the readout electronics of the CAL. Less than 3% of the trigger towers gave no signal and all RCAL EMC channels were active. For $10\ \mathrm{GeV}^2 < Q^2 < 100\ \mathrm{GeV}^2$, more than 95% of all events satisfied the RCAL EMC trigger.

The sensitivity to individual trigger channel defects was reduced by the fact that a single event can exceed more than one of the trigger thresholds, so that the overall efficiency of the hardware was greater than 99% in all regions of x and Q^2. The trigger calibration scale error, which is approximately 10%, resulted in an uncertainty of 1% to the trigger acceptance for $Q^2 > 10\ \mathrm{GeV}^2$.

5.6 Data Characteristics

It is imperative to compare some of the properties of the selected events with a Monte Carlo simulation of deep-inelastic scattering events in order to gain confidence that the detector has been properly modelled and that the background has been removed. Figure 5.9(a) shows the measured electron energy distribution and the prediction of the CDM Monte Carlo simulation. (The electron energy spectrum is obtained from the electroweak cross-section. Therefore, it is not really a *prediction* of the CDM QCD model but is obtained from that part of LEPTO that generates the hard scattering for ARIADNE.) The data are shown as points with statistical errors and the simulation as the shaded histogram. It can be seen that the agreement is not particularly good as the position of the peak is shifted to lower values than predicted. This effect is attributed to inaccurate modelling of the inactive material between the interaction point and the front of the RCAL in the detector simulation program [119].

Because of this poor agreement, Equations (5.2) and (5.3) cannot be used to determine the kinematics. However, if Q^2 is calculated from (5.9) and then (5.2) is used to solve for E_e', the distribution shown in Figure 5.9(b) is obtained. The data and simulation are in agreement if the double angle method is used. Therefore, all variables are measured using the double angle method and henceforth the subscript denoting the measurement method will be dropped.

Figure 5.10(a) shows the electron polar angle distribution. This is primarily a consequence of the $1/Q^4$ factor in the cross-section (Equation (2.10)) and is well described by the Monte Carlo simulation. The distribution in γ_h is shown in Figure 5.10(b) and also gives satisfactory agreement with the CDM simulation. The agreement is not as good as that of the electron angle because the

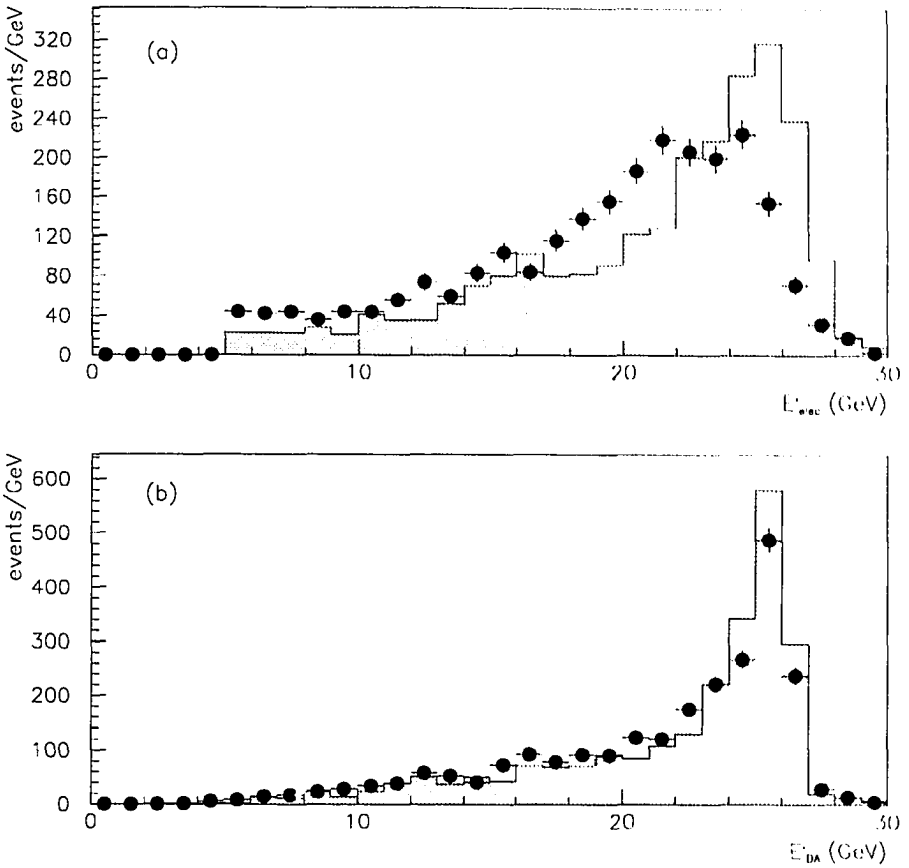

Figure 5.9: The electron energy spectrum as measured (upper distribution) and as calculated from the double angle method (lower distribution). The histograms show the colour dipole model Monte Carlo simulation including radiative corrections.

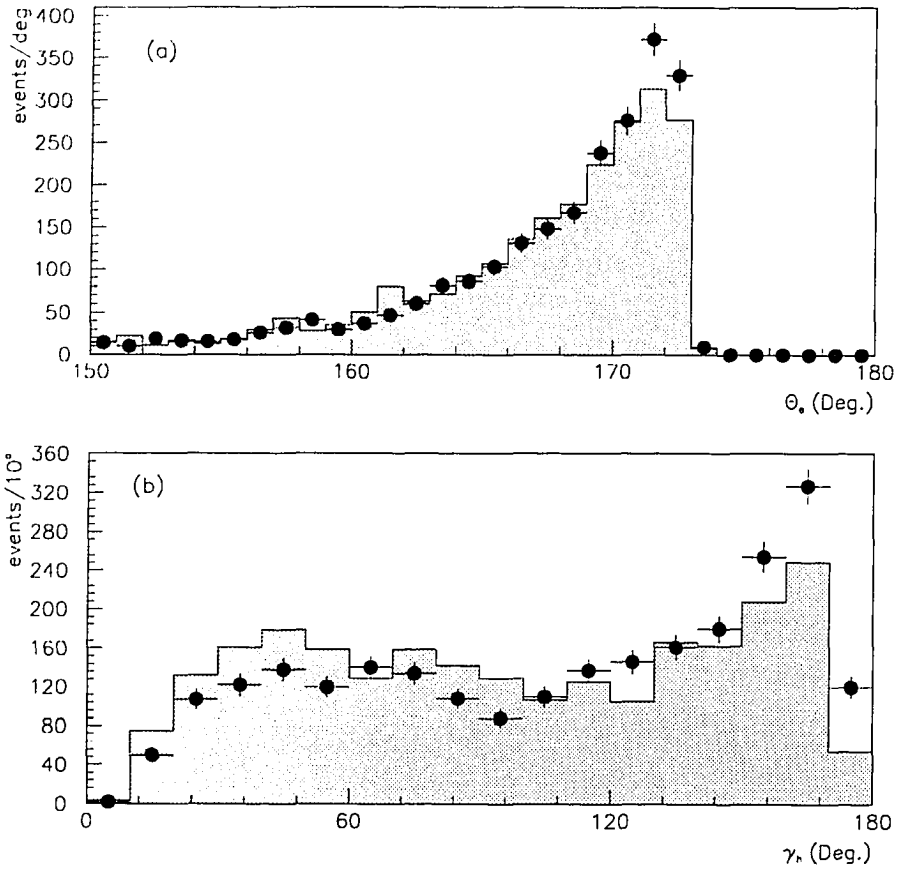

Figure 5.10: Comparison of the data with the Monte Carlo simulation: (a) electron angle, (b) hadron system angle, γ_h. The histograms show the CDM Monte Carlo simulation including radiative corrections.

Monte Carlo distribution is sensitive to the structure function parametrization used by the event generator.

Although the electron energy distribution demonstrated inadequate detector modelling in part of the RCAL, this problem can be avoided by using the double angle method for reconstructing the kinematics. Furthermore, the reasonable agreement between the data and the Monte Carlo simulation for the double angle scattered electron energy and angle suggests that there are not other problems with the detector modelling. This is because this method uses the hadronic final state which deposits energy throughout the detector.

The distribution of events in the W^2-x plane is shown in Figure 5.11. The data reaches x values that are two orders of magnitude smaller than have been accessible to previous fixed target experiments [25] [26] in this range of momentum transfer so that the W^2 values extend to almost 10^5 GeV^2. The maximum value of W^2 is given by s. The broad range spanned in x and W^2 at HERA allows a study of the dependance of QCD radiation on these two variables. The QPM kinematics are also illustrated in Figure 5.11(a) by the γ_h contours (full lines) that mark the boundaries between the three parts of the calorimeter. The dashed line shows a 10° contour that is discussed later. The γ_h contours are generally in RCAL for low x events because low x partons carry a small fraction of the proton's momentum (in the QPM). Conversely, γ_h generally points in the direction of FCAL for high x events because high x partons have a large momentum component along the proton direction.

The W^2 range is much larger than that of Q^2 as seen in Figure 5.11. The Q^2 distribution has been normalized to the number of events, N. It falls rapidly with Q^2, reflecting the dominant effect of the photon propagator, whereas the distribution in W is relatively uniform. The histogram shows the prediction of the CDM model. The data is predominantly at low values of Q^2 and overlaps the Q^2 range of previous experiments. Since the exchange of a Z^0 is suppressed by a term of the form $(Q^2/(Q^2+M_Z^2))$, this data sample is dominated by the exchange of a virtual photon.

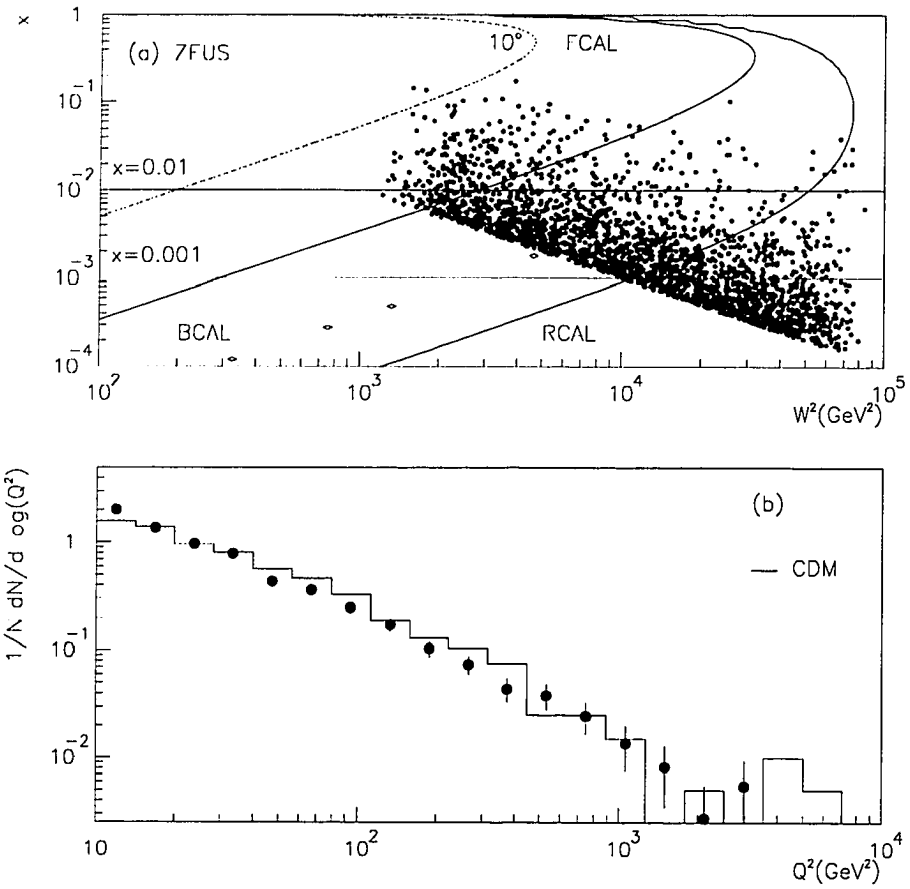

Figure 5.11: (a) The W^2 - x distribution of the data marked with the x bins used in the analysis. The contours of the angles corresponding to the boundaries of the calorimeter components are also shown. The dashed curve corresponds to a 10° contour. (b) The Q^2 distribution. The histogram shows the CDM Monte Carlo with radiative corrections.

Chapter 6

Hadronic Energy Distributions

In Chapter 2 it was stated that results from lower energy deep-inelastic scattering experiments and the observation of two jet events at HERA indicate that it is necessary to include QCD contributions to the QPM in describing the structure of the hadronic final state in deep-inelastic scattering. The exact matrix elements, calculated order by order in the strong coupling, can be used to estimate these corrections. However, only partial second order results exist for deep-inelastic scattering. Alternatively, models based on the leading logarithm approximation, with modifications for coherence effects, can be employed. There are several such models, which can be divided into two general classes: parton showers and colour dipoles. Both the parton shower and colour dipole models describe present e^+e^- data for the radiation of the final state quarks. They are also in fair accord with the lower energy deep-inelastic scattering data, but the agreement is not as good as for e^+e^- annihilation. As shown in the preceding chapter, the present data extends to much lower x values than has been observed previously and where the W^2 and Q^2 values are very different. This results in contrasting predictions for the PS(W^2) and PS(Q^2) models. Since low x partons result from a sequence of emissions from higher x partons, it is expected that collinear and infrared coherence effects should be important in the low x region. It therefore provides a powerful testing ground for the different models.

6.1 Results

A series of calorimeter cell energy distributions is used to compare the data with the predictions of the Monte Carlo models discussed in Chapter 2. Each calorimeter cell defines a vector, $\vec{E}$, with direction given by the event vertex and the geometrical centre of the cell, and magnitude by the energy deposit. In order to study the x dependence of the QCD radiation, the distributions are plotted in three different x bins: $x < 10^{-3}$, $10^{-3} < x < 10^{-2}$, and $x > 10^{-2}$. The highest bin is close to the x region covered by existing data, whereas the lowest x region only becomes accessible at HERA energies.

This thesis is concerned with a study of models of QCD radiation and not with phenomenological models of the proton remnant. Therefore, in all of the comparisons, cells with $\theta < 10^{\circ}$ are removed to reduce the influence of the proton remnant. All CAL cells corresponding

to the scattered electron have also been removed. The error bars on the data that is to be presented are statistical and are within the symbols if they are not shown. Systematic checks on the Monte Carlo event samples are discussed in the following section. All of the Monte Carlo samples shown were generated with the MRSD0 parton density parametrization [120].

The hadronic final state energy flow distributions as a function of the polar angle, θ, are shown in Figure 6.1 for the three x regions and for different W^2 selections. These distributions show data only and illustrate that the general features of the data agree with the QPM current jet kinematics that are shown in Figures 5.1(c-d). In the lowest x range, Figure 6.1(a), a jet energy peak at large angles is clearly visible superimposed on a falling distribution at small angles. The current jet is expected to be in RCAL at low x because the struck parton's four-momentum is much less than that of the incoming electron. With HERA kinematics, the current jet swings from the forward to the backward region at fixed x as the W^2 values increase. This is because the momentum transfer to the struck parton increases, as can be seen in Equation (2.31). This effect is illustrated in Figures 6.1(b-d), showing the results in the intermediate x range. At high x, shown in Figure 6.1(e), the data exhibits a smooth fall with θ since for most of the events the hadronic system has a high energy and populates the forward region. In all cases, however, the energy is distributed over the full range of polar angles.

The transverse energy flow of the hadronic system is shown in Figure 6.2. To illustrate better the model comparisons, the same data are shown separately in two sets of three x-range plots. These distributions show transverse energy weighted azimuthal angles, ϕ, where $\phi = 0^\circ$ is defined by the direction of the scattered electron. The absolute value of ϕ is taken because of the azimuthal symmetry with respect to the scattered electron. The transverse energy, E_T, of each cell is given by $E\sin\theta$. In the QPM, this distribution should be peaked sharply at $\phi = 180^\circ$ with very little energy over the rest of the angular range.

In all cases, the data peak at $\phi = 180^\circ$ with the hadrons balancing the E_T of the electron. This is particularly clear in the two higher x bins. In the lowest x region, the data show a broader E_T distribution. In addition, the total E_T, which is the area of each distribution, increases as x decreases, i.e. as W increases. This feature of the data is shown in Figure 6.3.

The histograms in Figures 6.2(a-c) show the predictions of several different models. The first order matrix element calculation (dashed-dotted histogram) predicts a distribution that is more peaked in ϕ than is observed, particularly at the lower x values. This poor agreement between the data and the predictions of the first order matrix elements highlights the need to take into account

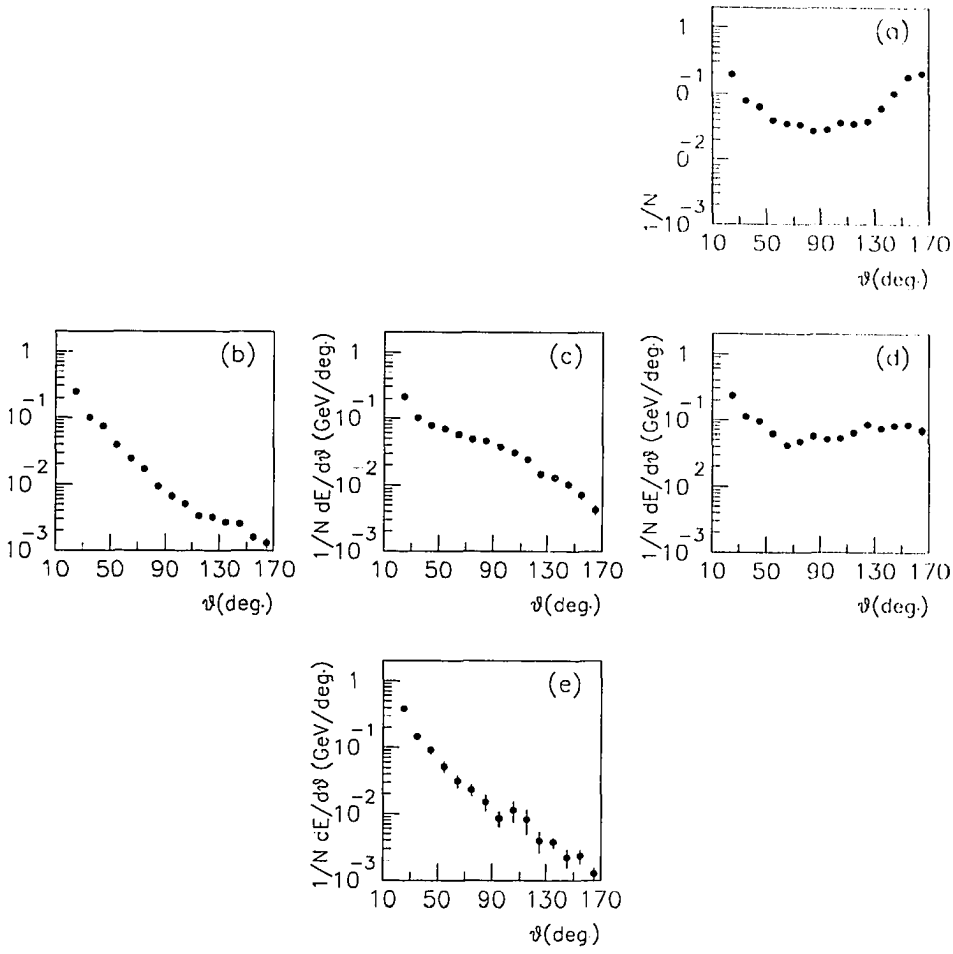

Figure 6.1: The energy weighted θ distributions in the ranges of x and W^2 used in this analysis. In (a) $x < 0.001$ and $15000 < W^2 < 60000$ GeV^2. In (b)-(d) $0.001 < x < 0.01$ with $1000 < W^2 < 7000$ GeV^2, $7000 < W^2 < 15000$ GeV^2 and $15000 < W^2 < 60000$ GeV^2, respectively. In (e) $x > 0.01$ and $1000 < W^2 < 60000$ GeV^2.

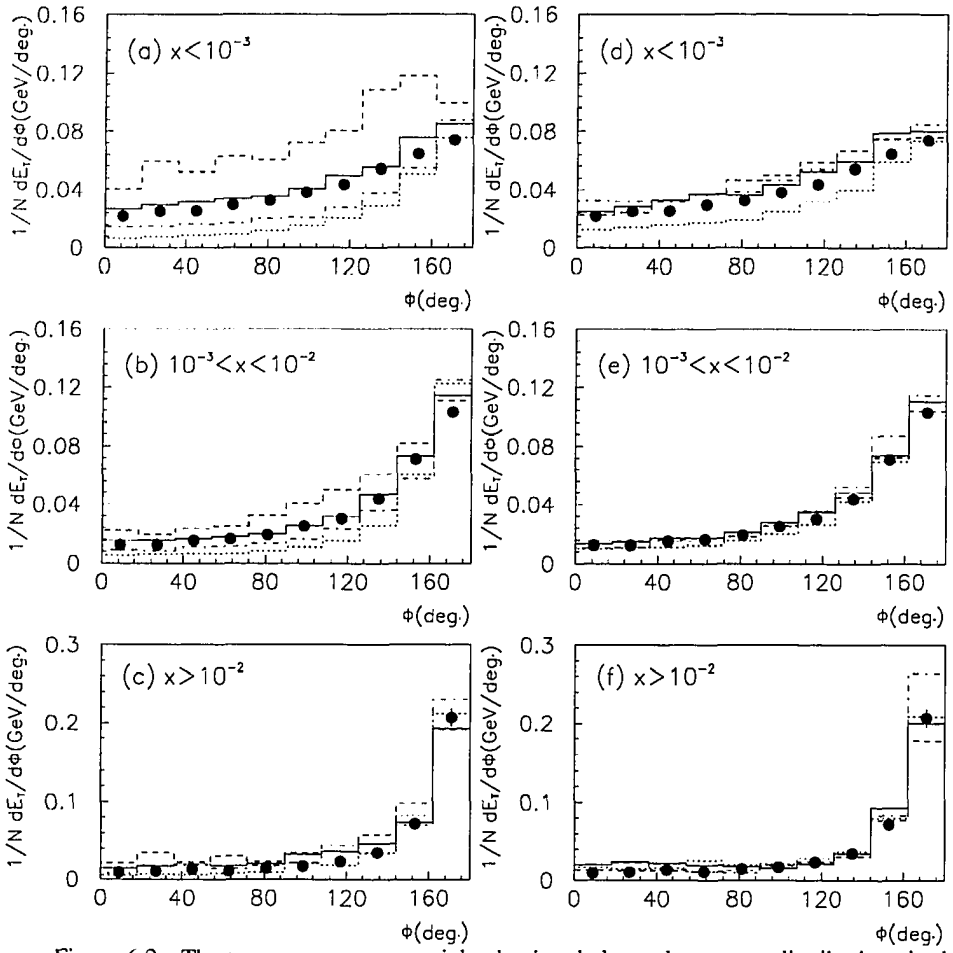

Figure 6.2: The transverse energy weighted azimuthal angular energy distributions in the three ranges of x: $x < 10^{-3}$, $10^{-3} < x < 10^{-2}$, and $x > 10^{-2}$. The scattered electron is defined as $\phi = 0$. The data points are shown as the dots. In (a-c) the full histogram is ME+PS, the dashed histogram PS(W^2), the dotted histogram PS(Q^2), and the dashed-dotted histogram ME. In (d-f) the full histogram is CDM+BGF, the dashed histogram is CDM, the dotted histogram is PS(Q^2(1-x)), and the dashed-dotted histogram is HERWIG.

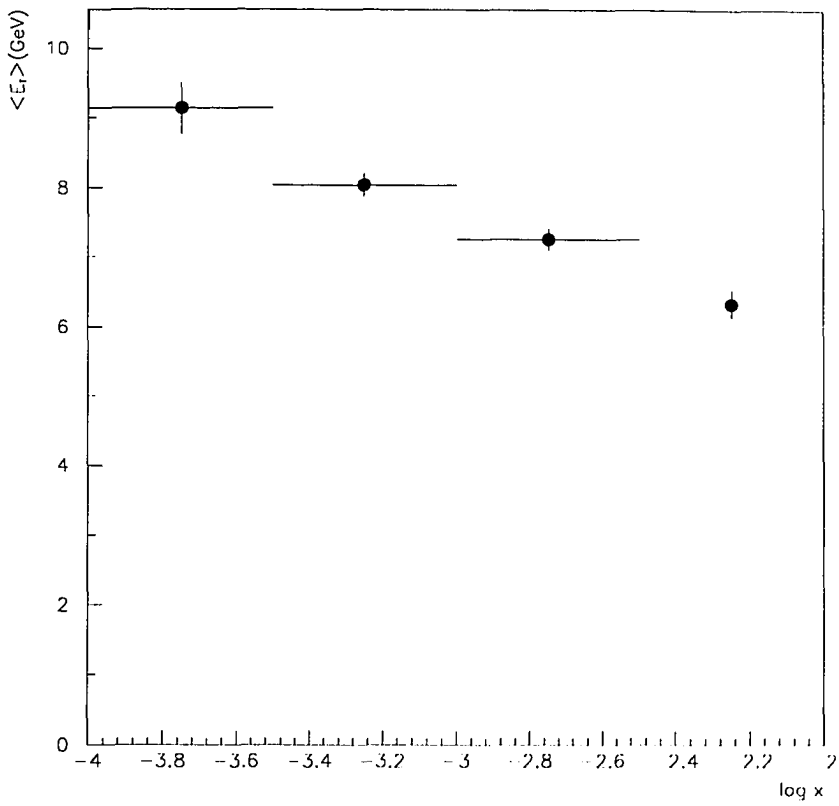

Figure 6.3: The mean E_T of the hadronic final state with respect to the proton direction as a function of x.

higher orders in α_s. The PS(W^2) model (dashed histogram) reproduces the general shape of the data but much overestimates the E_T. Since W^2 is the virtuality scale that gives the full emission phase space, this result shows that coherence effects have a significant effect on parton emissions. On the other hand, the PS(Q^2) approach (dotted histogram) predicts even less E_T than the matrix elements, particularly at the lower x values. The ME+PS model (full histogram), in which coherence effects are properly taken into account in the first hard emission, gives a good description of the E_T distributions of the data.

It can be demonstrated that the observed broadening of the event structure in the transverse

plane is due *not* to kinematics, but primarily to QCD radiation, by a comparison of the data with the predictions of the PS(Q^2) model. This is because this model yields little gluon radiation so that its predictions are close to those of the QPM. The x dependence of the PS(Q^2) predictions, therefore, is essentially due to kinematic effects. As can be seen, this is much smaller than the x dependence of the data.

The different behaviour predicted by the W^2 and Q^2 choices of the virtuality scale, shown in Figure 6.2(a), can be understood from Equation (2.31): at low x, the values of W^2 are much larger than those of Q^2. This allows more gluon radiation since the parton shower can be evolved to a higher virtuality scale. For the highest x region, however, the predictions of the two parton shower models are similar since the Q^2 and W^2 values are more similar. In this region all of these models give a reasonable representation of the data.

The PS(Q^2(1-x)) choice (dotted histogram) is shown in Figures 6.2(d-f). It gives a good description of the data in the two highest x bins, but predicts too little E_T at low x. The comparisons with the CDM (dashed histogram) and CDM+BGF models (full histogram), along with the HERWIG model without the soft underlying event (dashed-dotted histogram), are also shown in these figures. It is clear that these models are in reasonable accord with the E_T distributions of the data. However, the HERWIG model does predict a more peaked distribution in the highest x region than is observed. The HERWIG prediction including the soft underlying event is not shown but is similar.

The fact that the CDM model, which has the exact matrix element calculation for the QCD Compton process, and the CDM+BGF model give a reasonable description of the data is in accord with the above result that first order matrix elements and higher order effects are necessary because of large coherence effects. HERWIG, however, does not include any matrix element calculations and seems to give a reasonable description of the data. Although it has a more sophisticated treatment of coherence effects than the PS(Q^2) model, these are for soft and collinear gluons, not for hard emissions. The reason for this apparent contradiction is given in the following section.

To study the transverse energy arising from gluon radiation, the energy component perpendicular to the scattering plane, $(E_t)_{out}$, was measured. The scattering plane is defined by the z-axis and an axis in the x-y plane that was determined by maximizing the sum $\sum_i E_{T_i} \cos\phi_i$. The sum is over all cells, including those associated with the found electron. In the QPM, this is the plane that contains the beam axis, the scattered electron and the struck quark. The only $(E_t)_{out}$ in

this model is that due to hadronization.

In Figure 6.4, the mean $(E_t)_{out}$ of the hadronic system is shown as a function of W^2 for the different x bins. The data show an increase of $(E_t)_{out}$ as W^2 increases. This might be expected since an increase in W^2 at fixed x means that the increase in the hadronic final state energy is due entirely to Q^2. Therefore, energy is not taken by the remnant and is available for QCD radiation. These comparisons with the Monte Carlo models show the same general trends seen in the previous comparisons. Again, the PS(Q^2), PS(W^2), and ME predictions are in poor agreement with the data, whereas the CDM, ME+PS, and HERWIG predictions are in general agreement with the data, although some deviations are evident at high x and high Q^2.

A more sensitive display of the energy flow for the low x region is shown as a function of pseudorapidity in Figure 6.5. The pseudorapidity, η, is given by $\eta = -\ln(\tan(\frac{\theta}{2}))$. This plot shows the energy weighted pseudorapidity difference between each calorimeter cell not assigned to the scattered electron and that of the hadronic system angle γ_h, i.e. $\Delta\eta = \eta - \eta_{\gamma_h}$. Since γ_h is the direction of the scattered quark in the QPM, this model predicts a peak at $\Delta\eta = 0$. For a γ_h at the RCAL/BCAL boundary, the 10° beampipe cut corresponds to a $\Delta\eta$ of approximately 3.1, so that the shape of the peak at large $\Delta\eta$ is influenced by this cut. The fall off at negative values of $\Delta\eta$ is not affected by the rear beam pipe, which is near $\Delta\eta = -1.5$.

It is striking that almost all of the energy appears at positive values, between the direction of γ_h and that of the proton remnant. Such behaviour is expected from the gluon radiation that should be concentrated in this angular range. For this low x range, there is a continuous distribution of energy flow from that associated with the struck quark to that coming from the proton remnant even though γ_h points in the direction of the RCAL, i.e. opposite to the direction of the proton remnant, as can be seen in Figure 5.11(a). In addition, a shift in the peak from the expectation of the QPM model is clearly seen.

The predictions of PS(W^2) (dashed histogram), PS(Q^2) (dotted histogram), and ME (dashed-dotted), shown in Figure 6.5(a), do not reproduce the data. The peaks in the PS(Q^2) and ME distributions are centered at γ_h ($\Delta\eta \approx 0$). Since these models have the correct kinematics and include the detector simulation, this indicates that the shift in the data is in fact due to QCD radiation. The ME+PS prediction (full histogram) is in better agreement with the data near $\Delta\eta = 0$ although the peak is somewhat broader than that observed. This prediction falls below the data in the large $\Delta\eta$ region. However, as discussed below, in this region the model prediction is very sensitive to the y_{cut} parameter used to ensure that the matrix element cross-section calculations are well behaved. In this plot, a value of 0.01 has been used; the prediction with the default value of 0.015 underestimates the data even more.

The colour dipole models are compared to the data in Figure 6.5(b). Both the CDM (dashed histogram)

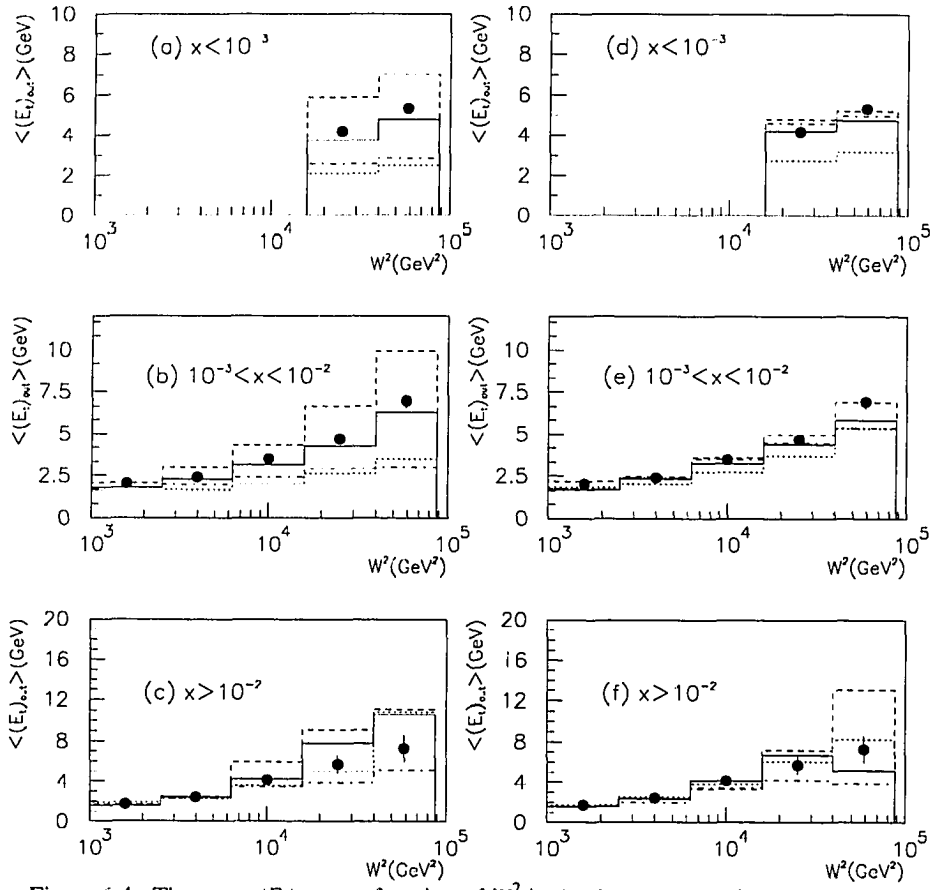

Figure 6.4: The mean $(E_T)_{out}$ as a function of W^2 in the three ranges of x. The data points are shown as the dots. In (a-c) the full histogram is ME+PS, the dashed histogram PS(W^2), the dotted histogram PS(Q^2), and the dash-dotted histogram ME. In (d-f) the full histogram is CDM+BGF, the dashed histogram is CDM, the dotted histogram is PS(Q^2(1-x)) and the dash-dotted histogram is HERWIG.

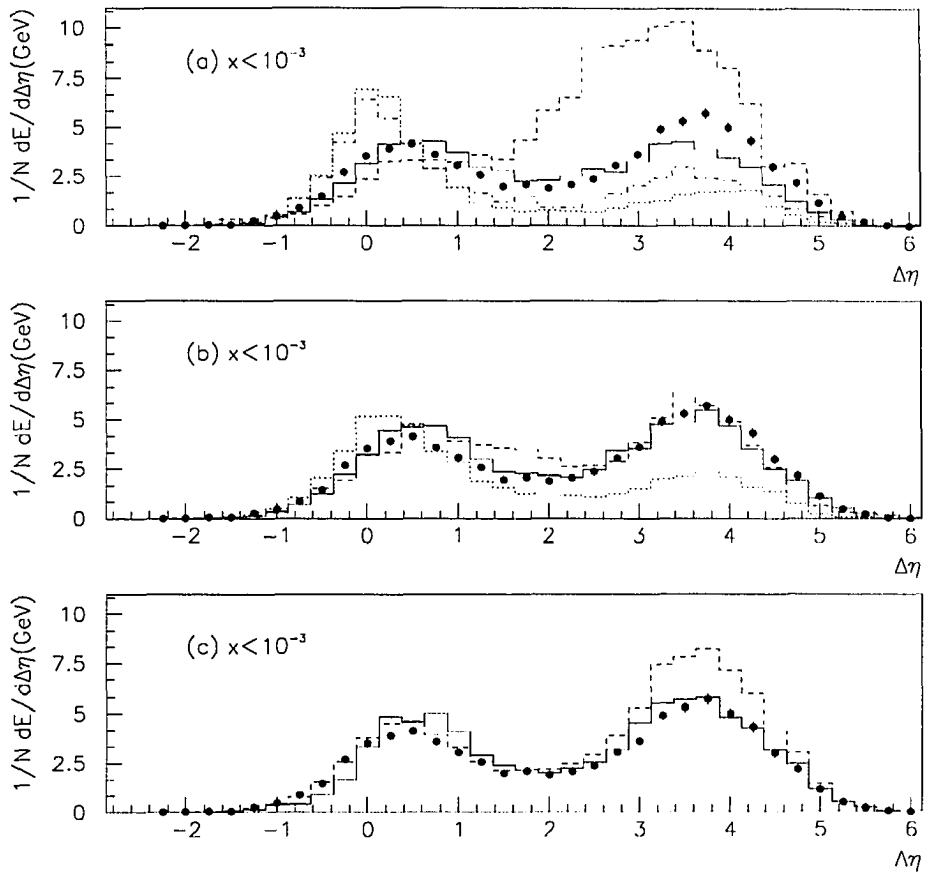

Figure 6.5: The energy weighted pseudorapidity difference, $\Delta\eta$, of the hadronic system calorimeter cells with respect to the struck quark from the quark-parton model. The data points are shown as the dots and are the same in all three figures. In (a) the full histogram is ME+PS, the dashed histogram is PS(W^2), the dotted histogram is PS(Q^2), and the dash-dotted histogram is ME. In (b) the full histogram is CDM+BGF, the dashed histogram is CDM and the dotted histogram is PS(Q^2(1-x)). In (c) the full histogram is HERWIG without the soft underlying event and the dashed histogram is HERWIG including the soft underlying event.

and the CDM+BGF (full histogram) give a better representation of the data than the other models, particularly at large $\Delta\eta$. However, these models somewhat overestimate the energy in the region between the quark and the proton remnant. The CDM+BGF model gives a better description of the data than does the CDM model, thereby giving evidence for the existence of the boson-gluon fusion process.

The PS(Q^2(1-x)) model is shown as the dotted histogram in Figure 6.5(b). It reproduces the peak at $\Delta\eta = 0$ better than either the PS(W^2) or PS(Q^2) models, but predicts too little energy for $\Delta\eta > 1$. It must be stressed that the differences in the Lund models in the larger $\Delta\eta$ region are due solely to differences in the treatment of QCD radiation because all models use the same hadronization of the proton remnant.

Figure 6.5(c) shows the predictions of the HERWIG model both with (solid histogram) and without (dashed histogram) the soft underlying event. The latter is in equally good agreement with the measurements as the CDM+BGF model whereas the prediction with the inclusion of an underlying event overestimates the energy flow in the large $\Delta\eta$ region.

6.2 Systematic Checks

To investigate whether these results are sensitive to the details of the models, various checks were made. The FCAL energy requirement of 1 GeV, applied after the other event selection cuts, rejected about 1% of the events in all of the Monte Carlo samples, with one exception. It removed about 4% of the events from the data sample. The exception was HERWIG without the soft underlying event, for which the fraction of events rejected was approximately 17%.

Unlike the majority of deep-inelastic scattering events that have a substantial energy deposit in the angular region encompassed by the proton beam direction and the struck quark, the rejected HERWIG events resemble diffractive events. Indeed, in about 5% of the events in the data sample, the hadronic energy deposit closest to the proton beam direction is at an angle larger than 25° [121]. That is, many of these events have a single jet in BCAL or RCAL and no energy in FCAL. The occurrence of such diffractive events was predicted in [122], but diffractive scattering has not been incorporated into HERWIG. A study of the HERWIG events that did not pass the FCAL energy requirement showed that the partonic final state usually contained only a struck quark and a proton remnant with the latter remaining in the forward beam pipe. The significance of this will be commented upon at the end of this chapter.

To study the effects of the electroweak radiative corrections, the predictions of ARIADNE

calculated both with and without the interface to HERACLES were compared. The shifts observed in the distributions were negligible compared to the large differences in the predictions of the various models. This is expected because of the coarseness of the kinematical binning and the removal of most of the hard initial state radiative events by the δ cut.

The effect of setting the vertex to $z = 0$, in the events for which no vertex could be determined by tracking and vertexing programs, was checked with the CDM model. The event kinematics were calculated by assigning the vertex to the nominal IP in all events, and by using the actual value of the generated vertex. There were some slight differences in a few bins of some of the distributions, but they were always smaller than the statistical errors. The insensitivity to the vertex distribution is due to the coarseness of the kinematical binning.

The dependence of the predictions of the QCD models on the parton density parametrization was studied using two sets of parametrizations by Morfin and Tung (MTB1 and MTB2) [123] and two sets by Martin, Roberts, and Sterling (MRSD0 and MRSD-) [120]. For all plots, the differences were within the statistical errors. As an example, the predictions of the PS(W^2) model for the transverse energy flow plot are shown with the MRSD0 set (solid histogram) and the MRSD- set (dashed histogram) in Figure 6.6. The predictions are shown without any detector simulation. The parton density parametrization affects the kinematical distribution of events, primarily in x. Since the distributions are plotted in three different x bins and normalized to the number of events, the insensitivity to the input parametrization might have been expected.

However, the initial state radiation predictions of parton shower models also depend upon the parton density parametrization as can be seen in Equation (2.29). Therefore, it was imperative to check this dependence because the predictions for the hadronic final state at a *fixed* x and Q^2 of a given model can differ depending upon the parton density parametrization. The fact that the parametrizations were indistinguishable shows that this effect is not large for these distributions, but it is possible to find distributions in which the differences resulting from different parametrizations are discernible [124].

The sensitivity of the PS and ME predictions to model parameters was also studied to determine if the observed differences between the data and model predictions could be reduced by parameter tuning. Parameters that affected the number of radiated partons generated, and their energy and transverse momentum, were varied. The strategy was to first perform the comparisons without any detector simulation in order to save computing time. Then, if any of the parameter changes resulted in significant differences, the comparisons would be redone with the full detector

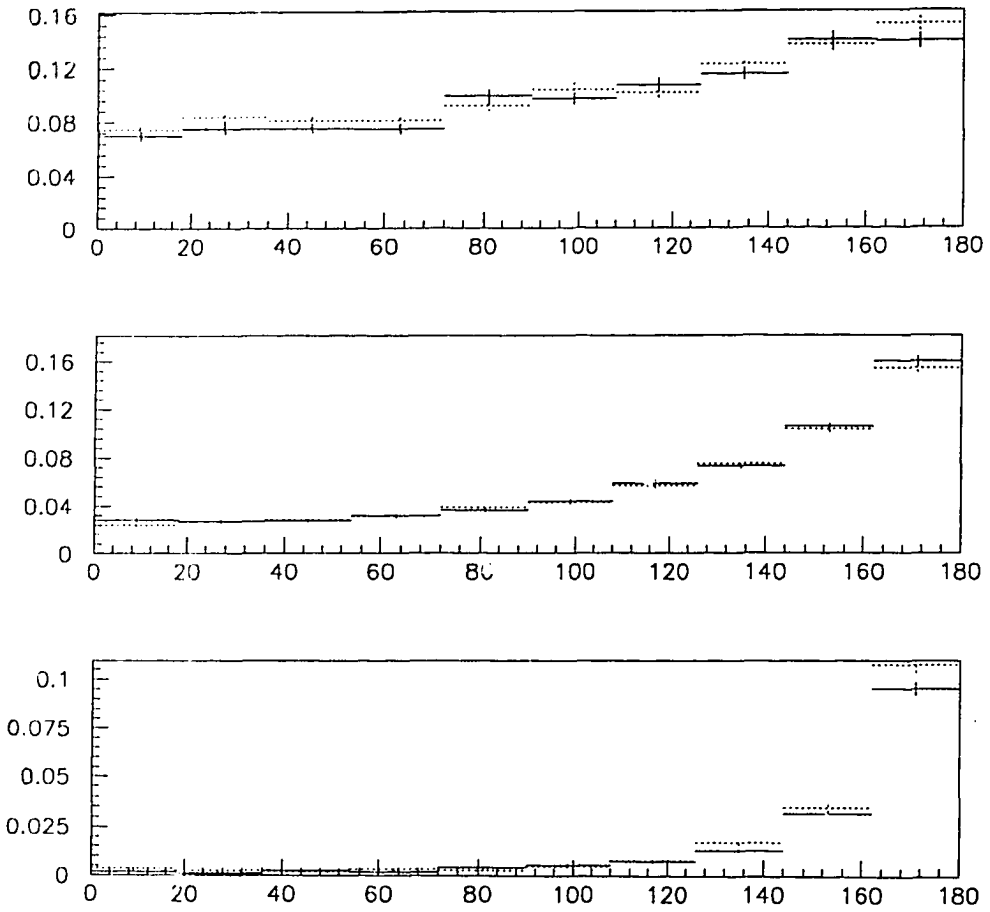

Figure 6.6: The predictions of the PS(W^2) transverse energy weighted azimuthal angle energy distribution, without any detector simulation, for the three x regions. The full histogram is the prediction with the MRSD0 parton distribution parametrization and the dashed histogram is with the MRSD- parametrization. (The scale on the left ordinate is arbitrary.)

simulation.

The *minimum* virtuality of 1 GeV in both the initial and final state parton showers was increased and decreased by a factor of three. (Reducing this parameter by more than a factor of three resulted in computer numerical problems.) This is the virtuality at which partons are assumed to be on mass-shell. The effect of these parameters for an energy weighted θ distribution is shown in Figure 6.7. The model shown is the PS(W^2) model. Since this model overestimates the data, both of these parameters were increased in order to reduce the amount of radiation generated

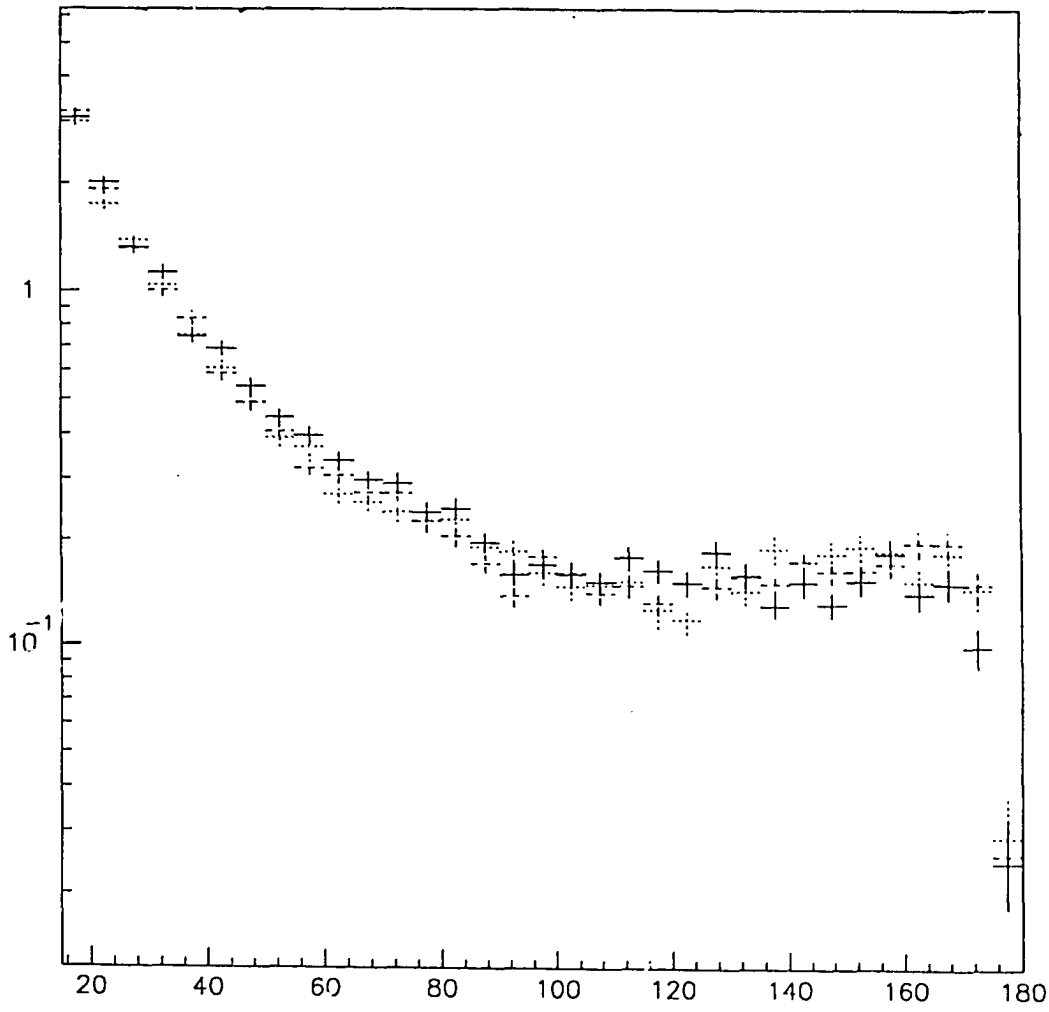

Figure 6.7: The predictions of the PS(W^2) model (without any detector simulation) for an energy weighted polar angle distribution. The solid histogram is with default parameter settings, the dashed histogram has Q_0^2 set to 3 GeV^2 and the dotted histogram has m_0 set to 2.5 GeV. (The scale on the left ordinate is arbitrary.)

in the parton showers. There is a small systematic decrease in the amount of energy predicted in the forward region but no difference is noticeable in the rear region.

The Λ parameter of the strong coupling used in both the initial and final state showers was

also varied by a factor of three since the value of the strong coupling affects the amount of radiation. In addition, the Gaussian width of the transverse momentum distribution of the partons within the proton was varied. The effect of the fragmentation was checked by changing the parameters that govern the energy-momentum fraction and the p_T distributions of the primary produced hadrons in the Lund string model. The transverse energy flow plots were the most sensitive to these changes. Nevertheless, the effects were always either smaller than or on the order of the statistical errors. The ME model is sensitive to the y_{cut} parameter in the forward region. An increase from 0.0025 to 0.015 decreases the prediction for the energy deposited in the $10^\circ - 20^\circ$ region by approximately 10%. However, the transverse energy flow has little sensitivity to this parameter. All of these variations are larger than those made in tuning the values to match lower energy data [32]. Table 6.1 lists the parameters changed, their default values, and the exact

Parameter	default value	range of variation
y_{cut} (PARL(8) in LEPTO)	0.0025	[0.0025,0.015]
Q_0^2 (PYPAR(22) in LEPTO)	1.0 GeV^2	[0.5,3.0]
m_0^2 (PARE(22) in JETSET)	1.0 GeV	[0.5,2.5]
p_T (PARL(3) in LEPTO)	0.44 GeV	[0.0,0.88]
Λ in initial state shower (PYPAR(21) in LEPTO)	0.25 GeV	[0.07,0.80]
Λ in final state shower (PARE(21) in JETSET)	0.40 GeV	[0.07,0.80]
a (PAR(31) in JETSET)	0.5	[0.3,0.8]
σ_q (PAR(12) in JETSET)	0.35 GeV	[0.3,0.88]

Table 6.1: Parameters varied in the parton shower and matrix element models.

range of variation. To summarize, the effects of changing the parton shower and matrix element model parameters are small and do not reduce the discrepancy between the model predictions and the data. They would be negligible if a detector simulation were performed.

In addition to checking the models, it is also necessary to examine effects that could introduce systematic changes in the shapes of the distributions. A possible source of contamination of the deep-inelastic scattering sample is photoproduction background. This mainly occurs in the low Q^2, low x regions. To estimate this background, events with $Q^2 < 2\text{GeV}^2$ were generated with the

PYTHIA [125] program. They were passed through the complete event selection to determine the background. The estimated photoproduction background is 10% in the lowest x region and 3% overall.

Since the electron identification algorithms have differing purities for accepting deep-inelastic scattering events compared to possible photoproduction background, the effect of this background can be checked by using a different algorithm. The data selection and the distributions were redone with EEXOTIC, a modified version of ELECT that has been tuned to improve the purity. A direct comparison of ELECT and EEXOTIC does not directly show the effect of reducing the photoproduction background as the algorithms also differ in their assignment of calorimeter cells to the electron. This latter effect can be isolated by comparing Monte Carlo distributions, which have no photoproduction background, using the two algorithms. The upper plot in Figure 6.8 shows the CDM predictions for the transverse energy weighted azimuthal angular distribution in the lower x region. The solid points are for ELECT and the dotted points are for EEXOTIC. It can be seen that the differences are small and that there is no change to the overall shape of the distribution. The lower plot shows the data. At large angles, it appears that the photoproduction events have the effect of shifting the data points up, however, this effect is small when compared to the model differences shown in Figure 6.2. Figure 6.9 shows the energy weighted pseudorapidity difference distribution for the data. Again, the solid points are for ELECT and the dotted points are for EEXOTIC. The distribution is the same shape for both of the electron identification algorithms. It therefore can be concluded that the photoproduction background does not affect any of the conclusions and that the shape of the distributions is not dependent upon the choice of electron identification algorithm.

As a further check, it is also possible to reduce possible photoproduction background by increasing the energy cut on the found electron from 5 GeV to 10 GeV. This change also does not alter the overall trends of the distributions so that the conclusions are unchanged.

A proper comparison of Monte Carlo model predictions with data requires that the CAL calibration be well understood. The calibration procedure was described in Chapter 3. The *in situ* calibration can be checked with halo muons which traverse the RCAL and FCAL along their tower structure. Dedicated halo muon runs were taken for this purpose with a trigger that required a coincidence between an energy deposition above a threshold in the BCAL and a hit in the vetowall. For each CAL section type, the spectra of deposited energy was determined and fit functions were used to determine the most probable value of energy deposition. The most

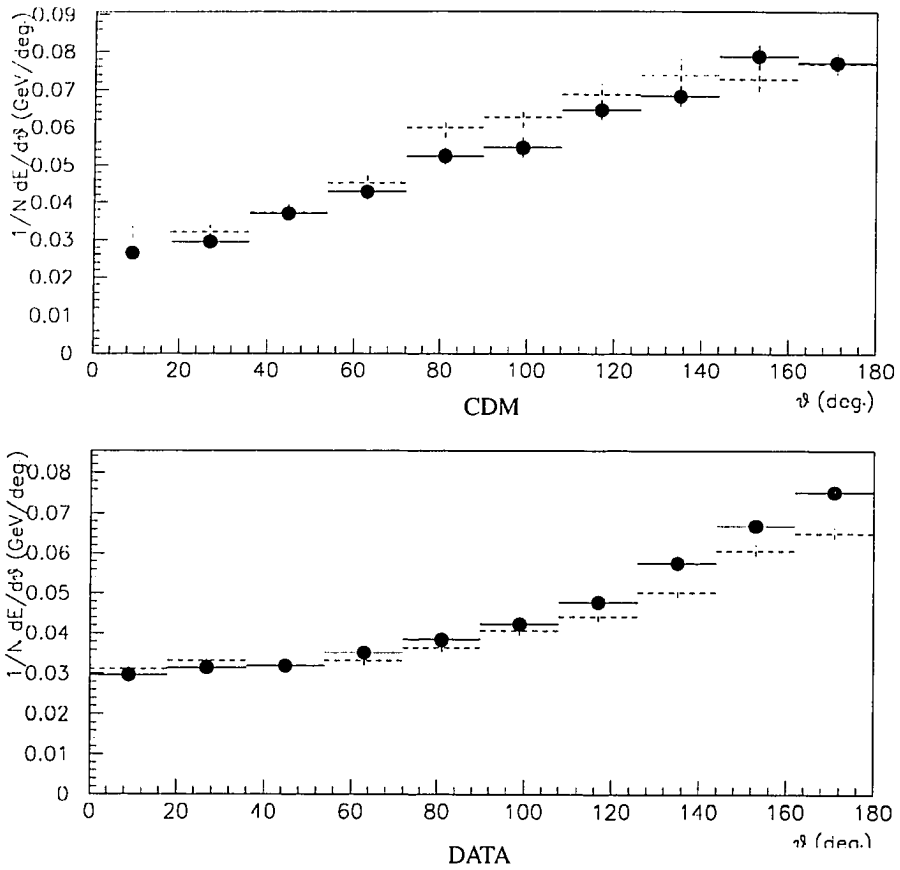

Figure 6.8: The transverse energy weighted azimuthal angular distribution with the ELECT and EEXOTIC electron finders for $x < 10^{-3}$. The top figure shows the CDM model predictions and the bottom figure shows the data. The solid points are for ELECT and the dotted points are for EEXOTIC.

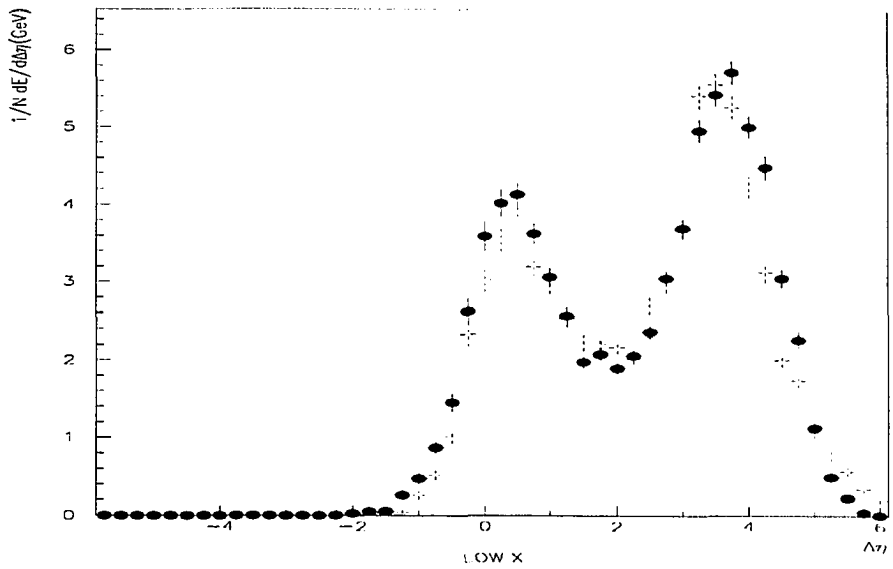

Figure 6.9: The energy weighted pseudorapidity difference of the data for two different electron identification algorithms. The solid points are for ELECT and the dotted points correspond to EEXOTIC.

probable values, μ/UNO, are calibrated with the UNO signal by multiplying the energy deposit by the ratio of the nominal current from the UNO signal to the actual uranium current. The comparison of the results from the halo muon and cosmic muon analysis is shown in Table 6.2. The halo muons systematically deposit more energy because of their higher momentum. The difference between the cosmic and halo muons is higher for RCAL than FCAL because the muons generally lose a few GeV in traversing the BCAL. It can be concluded that the energy scale is known to within 4%. This, however, is very conservative because a difference is expected due to the higher momentum of the halo muons. A more accurate measurement will be possible when the FMUON information is available. Although there is no reason to suspect that the calibration is different in the ZEUS environment than in the test beams, the effect of varying the hadronic energy scale by $\pm 5\%$ was checked. It is smaller than the statistical errors.

The detector simulation shows that the energy corrections due to dead material and the

smearing coming from resolution and acceptance effects are about 20% for most of the distributions. The correction factors for Figures 6.5 and 6.2 are shown in Figures 6.10 and 6.11, respectively. The factors were determined by dividing the CDM Monte Carlo prediction for a

Section Type	$\langle \mu/UNO \rangle_{cosmic}$	$\langle \mu/UNO \rangle_{halo}$	mean difference
FEMC	0.3279 GeV	0.3379 GeV	3.0%
FHAC1	1.0698 GeV	1.0925 GeV	2.1%
FHAC2	1.0749 GeV	1.1001 GeV	2.3%
REMC	0.3270 GeV	0.3400 GeV	3.9%
RHAC1	1.0716 GeV	1.1156 GeV	4.0%

Table 6.2: Comparison of cosmic muon analysis with halo muon analysis.

given distribution, without any detector simulation, by the same distribution after the detector simulation. In order to make a meaningful comparison of the different model predictions, the correction factors must be the same for all models. This is not *a priori* true because detector response and acceptance is a function of particle energies and angles and the various models can give distinct distributions in these variables. The correction factors for the two extreme models, $PS(W^2)$ and $PS(Q^2)$, were calculated and are the same as for the CDM model within statistical errors.

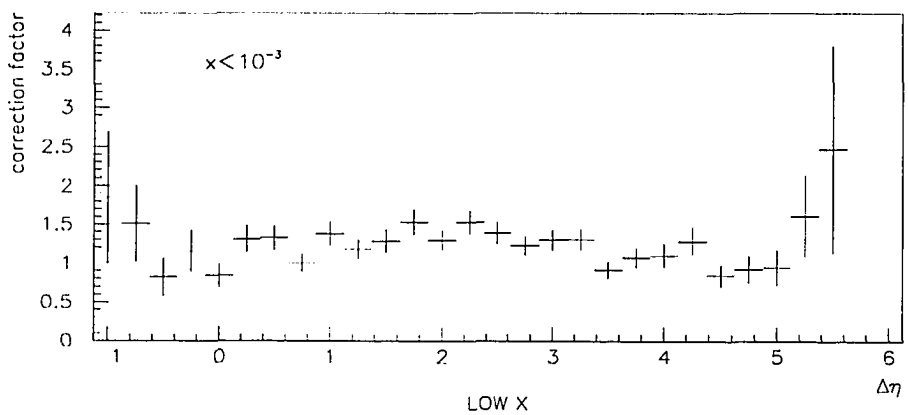

Figure 6.10: Correction factors for Figure 6.5.

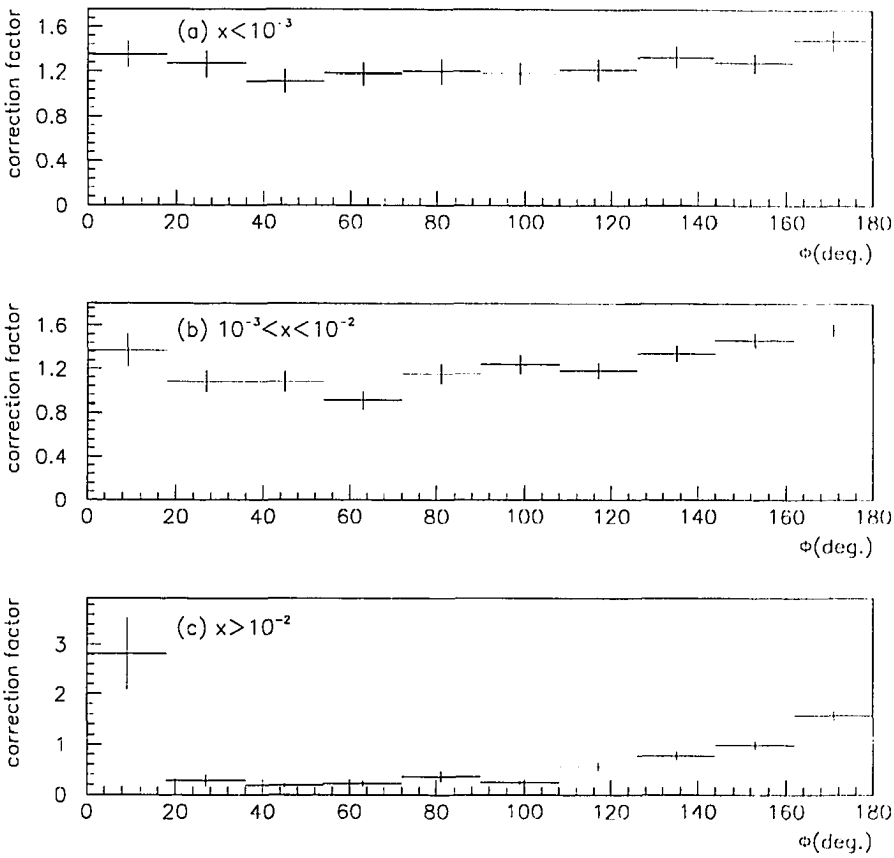

Figure 6.11: Correction factors for Figure 6.2.

The correction factors for the transverse energy flow distribution at high x, shown in Figure 6.11(c), are generally less than one. An explanation is that the transverse energy is calculated from the polar angle of the centre of the CAL cells, so that it is implicitly assumed that the energy is evenly distributed over the cell. However, the energy weighted polar angle distribution in the high x range is steeply falling with theta and so this method tends to overestimate the transverse energy in this kinematical region.

6.3 Summary and Discussion

Measurements in the laboratory frame of hadronic energy distributions in deep-inelastic scattering at HERA have been presented. For decreasing x, an increase in E_T, with respect to the proton direction, of the hadronic system is observed as well as a general broadening of the energy flow in the transverse plane. In the low x region, the peak in the hadronic energy flow in the direction of the current jet is shifted from the position expected by the QPM towards the proton remnant with most of the energy appearing between the position of the expected jet peak and that of the proton remnant. This is a remarkable illustration of the effects of QCD radiation.

The comparisons with the data show that the Lund model, in which the first order matrix elements are combined with parton showers, gives a reasonable description of the energy flows. By contrast, the predictions of a model based on the first order matrix elements alone are in disagreement with observation, thus demonstrating the importance of higher order QCD effects. Furthermore, in the Lund parton shower model alone, neither the choice of W^2 nor Q^2 to set the virtuality scale for the parton showers can describe the final hadronic state. The scale $Q^2(1-x)\max(1, \ln\frac{1}{x})$, motivated by the behaviour of the matrix elements, also fails. The differences cannot be accounted for by changes in the fragmentation parameters, model parameters, or parton density parametrizations.

The patent failure of the PS(W^2) model, in particular at low x, shows the strong effect coherence has on reducing the total available emission phase space. On the other hand, the failure of the PS(Q^2) and the PS(Q^2(1-x)) models shows that the phase space reduction cannot be achieved by applying an effective p_T-cutoff on the gluon radiation. The exact first order matrix elements are necessary for a correct description of the data.

The predictions of the colour dipole model also agree with the overall trends of the data. The colour dipole model with the inclusion of the boson-gluon fusion process gives the best description of the data. If the boson-gluon fusion process occurs, then one would expect that its

inclusion in a Monte Carlo model would be necessary for a correct description of the data. The fact that it does improve the description of the data cannot be construed as proof for the existence of this process, however, when combined with the ZEUS observation of two jet events, it does give very good evidence.

The predictions of the HERWIG parton shower model apparently give a reasonable description of the energy flows. The difference between the HERWIG parton shower model and the PS(Q^2) model cannot be attributed entirely to a more sophisticated treatment of coherence effects since the HERWIG sample used in the comparison with the data was biased. This is because of the relatively large number of generated events that did not pass the selection criteria. These events illustrate two points about the HERWIG model. First, there are no perturbative gluons generated in these events so that either the maximum virtuality is too low or the minimum virtuality is too high. Second, the cluster hadronization model, in contrast to the string model, predicts almost no energy between the struck quark and the remnant when there are no radiated gluons. Cluster hadronization, therefore, is only applicable when many hard gluons are simulated.

The HERWIG model with the soft underlying event overestimates the energy flow in the proton remnant region. This is not surprising because the soft underlying event is meant to simulate soft interactions in proton-antiproton collisions among partons that did not participate in the hard scattering. Such interactions are not present in electron-proton scattering because of the point-like behaviour of the electron.

A weakness in the Lund model is the sensitivity to the matrix element cut-off parameter. A reduction of this parameter increases the number of first order events generated which contribute considerably to the amount of energy predicted in the forward region. A study of these events showed that this was attributable to the boson-gluon fusion events and not to the QCD Compton events. This can be explained as follows [127]. At low x in the HERA laboratory frame, most of the boson-gluon fusion events have one quark in the rear direction and one in the very forward direction. Since there is a string stretched from each quark to the remnant, it can be understood why these events give a large contribution to the energy in the forward direction: a second string pulling a small amount of the remnant energy into the detector can contribute to a large percentage of the total energy in the calorimeter since the remnant is so energetic. As y_{cut} is reduced, a smaller invariant mass between all parton pairs is required, but there will still always be two strings drawn. That is, there is no smooth transition between a QPM event and a first order boson-gluon fusion event. This is not same for QCD Compton events. In this case, as y_{cut} is decreased in value,

events with softer gluons can be generated. Since the gluon is a kink on a single string between the struck quark and the remnant, there is a smooth transition from a QPM event to a quark- soft gluon event.

Similar model comparisons, using a subset of the models presented in this thesis and a data set of about 1.6 nb^{-1}, have been published by the H1 collaboration [126]. Their results are in agreement with the conclusions presented in this thesis.

The comparisons of the data with the Monte Carlo models demonstrates that there is a strong x dependence on gluon radiation. A study of this region thus provides a good testing ground for both perturbative and non-perturbative QCD models and thereby also gives insight into the basic underlying partonic processes. The analysis presented in this thesis excludes several perturbative models and indicates possible difficulties with the non-perturbative hadronization models. It provides further evidence in support of QCD as only those models that include the exact first order matrix elements and higher order effects give a reasonable description of the data. The data is not described by models that approximate these effects. Furthermore, the fact that the ME+PS and CDM models describe the data indicates that there is not yet evidence for deviations from Altarelli-Parisi evolution in the x range studied in this thesis.

Appendix A

The ZEUS Collaboration

M. Derrick, D. Krakauer, S. Magill, B. Musgrave, J. Repond, S. Repond, R. Stanek, R.L. Talaga, J. Thron

Argonne National Laboratory, Argonne, IL, USA [n]

F. Arzarello, R. Ayad[1], G. Bari, M. Basile, L. Bellagamba, D. Boscherini, A. Bruni, G. Bruni, P. Bruni, G. Cara Romeo, G. Castellini [2], M. Chiarini, L. Cifarelli, F. Cindolo, F. Ciralli, A. Contin, S. D'Auria, C. Del Papa, F. Frasconi, P. Giusti, G. Iacobucci, G. Laurenti, G. Levi, Q. Lin,B. Lisowski, G. Maccarrone, A. Margotti, T. Massam, R. Nania, C. Nemoz, F. Palmonari, G. Sartorelli, R. Timellini, Y. Zamora Garcia[1], A. Zichichi

University and INFN Bologna, Bologna, Italy[f]

A. Bargende, J. Crittenden, H. Dabbous[3], K. Desch, B. Diekmann, T. Doeker, M. Geerts, G. Geitz, H. Hartmann, D. Haun, K. Heinloth, E. Hilger, H.-P. Jakob, S. Kramarczyk, M. Kückes[4], A. Mass, S. Mengel, J. Mollen, D. Monaldi[5], H. Müsch[6], E. Paul, R. Schattevoy, J.-L. Schneider, D. Schramm, R. Wedemeyer

Physikalisches Institut der Universität Bonn, Bonn, Federal Republic of Germany[c]

A. Cassidy, D.G. Cussans, N. Dyce, B. Foster, R. Gilmore, G.P. Heath, H.F. Heath, M. Lancaster, T.J. Llewellyn, J. Malos, C.J.S. Morgado, R.J. Tapper, S.S. Wilson, R. Yoshida *H.H. Wills Physics Laboratory, University of Bristol, Bristol, U.K. [m]*

R.R. Rau

Brookhaven National Laboratory, Upton, L.I., USA [n]

M. Arneodo, T. Barillari, M. Schioppa, G. Susinno

Calabria University, Physics Dept.and INFN, Cosenza, Italy[f]

A. Bernstein, A. Caldwell, I. Gialas, J.A. Parsons, S. Ritz, F. Sciulli[7], P.B. Straub, L. Wai, S. Yang

Columbia University, Nevis Labs., Irvington on Hudson,N.Y.,USA [o]

J. Chwastowski[8], A. Dwurazny, A. Eskreys, Z. Jakubowski[9], B. Niziol , K. Piotrzkowski, M. Zachara, L. Zawiejski

Inst. of Nuclear Physics, Cracow, Poland[j]

B. Bednarek, P. Borzemski, K. Eskreys, K. Jelen, D. Kisielewska, T. Kowalski, E. Rulikowska-

Zarebska, L. Suszycki, J. Zajac
Faculty of Physics and Nuclear Techniques, Academy of Mining and Metallurgy, Cracow, Poland[l]

T. Kedzierski, A. Kotanski, M. Przybycien
Jagellonian Univ., Dept. of Physics, Cracow, Poland[j]

L.A.T. Bauerdick, U. Behrens, J.K. Bienlein, S. Böttcher, C. Coldewey, A. Dannemann, G. Drews, P. Erhard[10], M. Flasinski[11], I. Fleck, R. Gläser[12], P. Göttlicher, B. Gutjahr, T. Haas, L. Hagge, W. Hain, D. Hasell, H. Hultschig, G. Jahnen[13], P. Joos, M. Kasemann, R. Klanner, W. Koch, L. Köpke, U. Kötz, H. Kowalski, J. Krüger, J. Labs, A. Ladage, B. Löhr, M. Löwe, D. Lüke, J. Mainusch, O. Manczak[14], M. Momayezi, J.S.T. Ng, S. Nickel, D. Notz, K.-U. Pösnecker[15], M. Rohde, J. Roldán[16], E. Ros[8], U. Schneekloth, J. Schroeder, W. Schulz, F. Selonke, E. Stiliaris[16], E. Tscheslog[17], T. Tsurugai, W. Vogel[18], G. Wolf, C. Youngman *Deutsches Elektronen-Synchrotron DESY, Hamburg, Federal Republic of Germany*

H.J. Grabosch, A. Leich, A. Meyer, C. Rethfeldt, S. Schlenstedt
DESY-Zeuthen, Inst. für Hochenergiephysik, Zeuthen, Federal Republic of Germany

G. Barbagli, A. Francescato, M. Nuti, P. Pelfer
University and INFN, Florence, Italy[f]

G. Anzivino, R. Casaccia, S. De Pasquale, S. Qian, L. Votano
INFN, Laboratori Nazionali di Frascati, Frascati, Italy[f]

A. Bamberger, A. Freidhof, W. Kröger, T. Poser, S. Söldner-Rembold, G. Theisen, T. Trefzger
Physikalisches Institut der Universität Freiburg, Freiburg, Federal Republic of Germany[c]

N.H. Brook, P.J. Bussey, A.T. Doyle, J.R. Forbes, V.A. Jamieson, C. Raine, D.H. Saxon
Dept. of Physics and Astronomy, University of Glasgow, Glasgow, U.K.[m]

H. Brückmann[19], G. Gloth, U. Holm, H. Kammerlocher, B. Krebs, T. Neumann, K. Wick
Hamburg University, I. Institute of Exp. Physics, Hamburg, Federal Republic of Germany[c]

A. Fürtjes, E. Lohrmann, J. Milewski[14], M. Nakahata[20], N. Pavel, G. Poelz, W. Schott, J. Terron[16], F. Zetsche
Hamburg University, II. Institute of Exp. Physics, Hamburg, Federal Republic of Germany[c]

T.C. Bacon, R. Beuselinck, I. Butterworth, E. Gallo, V.L. Harris, D.B. Miller, A. Prinias, J.K. Sedgbeer, A. Vorvolakos, A. Whitfield
Imperial College London, High Energy Nuclear Physics Group, London, U.K.[m]

T. Bienz, H. Kreutzmann, U. Mallik, E. McCliment, M. Roco, M.Z. Wang
University of Iowa, Physics and Astronomy Dept., Iowa City, USA [n]

P. Cloth, D. Filges
Forschungszentrum Jülich, Institut für Kernphysik, Jülich, Federal Republic of Germany

S.H. An, S.M. Hong, C.O. Kim, T.Y. Kim, S.W. Nam, S.K. Park, M.H. Suh, S.H. You
Korea University, Seoul, Korea [h]

L. Chen, R. Imlay, S. Kartik, H.-J. Kim, R.R. McNeil, W. Metcalf
Louisiana State University, Dept. of Physics and Astronomy, Baton Rouge, LA, USA [n]

F. Barreiro[21], G. Cases, L. Hervás[22], L. Labarga[22], J. del Peso, J.F. de Trocóniz[23]
Univer. Autónoma Madrid, Depto de Fisica Teórica, Madrid, Spain [l]

F. Ikraiam, J.K. Mayer, G.R. Smith
University of Manitoba, Dept. of Physics, Winnipeg, Manitoba, Canada [a]

F. Corriveau, D.J. Gilkinson, D.S. Hanna[7], J. Hartmann, L.W. Hung, J.N. Lim, R. Meijer Drees, J.W. Mitchell, P.M. Patel, L.E. Sinclair, D.G. Stairs, M. St.Laurent, R. Ullmann *McGill University, Dept. of Physics, Montreal, Quebec, Canada* [a] [b]

G.L. Bashindzhagyan, P.F. Ermolov, L.K. Gladilin, Y.A. Golubkov, V.A. Kuzmin, E.N. Kuznetsov, A.A. Savin, A.G. Voronin, N.P. Zotov
Moscow State University, Institute of Nuclear Pysics, Moscow, Russia [k]

S. Bentvelsen, M. Botje, A. Dake, J. Engelen, P. de Jong, M. de Kamps, P. Kooijman, A. Kruse, H. van der Lugt, V. O'Dell, A. Tenner, H. Tiecke, J. Uijterwaal[24], M. Vreeswijk, L. Wiggers, E. de Wolf, R. van Woudenberg
NIKHEF-Amsterdam, Netherlands [i]

B. Bylsma, L.S. Durkin, K. Honscheid, C. Li, T.Y. Ling, K.W. McLean, W.N. Murray, I.H. Park, T.A. Romanowski[25], R. Seidlein
Ohio State University, Physics Department, Columbus, Ohio, USA [n]

G.A. Blair, A. Byrne, R.J. Cashmore, A.M. Cooper-Sarkar, R.C.E. Devenish, D.M. Gingrich[26], P.M. Hallam-Baker[8], N. Harnew, T. Khatri, K.R. Long, P. Luffman, I. McArthur, P. Morawitz, J. Nash, S.J.P. Smith[27], N.C. Roocroft, F.F. Wilson
Department of Physics, University of Oxford, Oxford, U.K. [m]

G. Abbiendi, R. Brugnera, R. Carlin, F. Dal Corso, M. De Giorgi, U. Dosselli, F. Gasparini, S.

Limentani, M. Morandin, M. Posocco, L. Stanco, R. Stroili, C. Voci
Dipartimento di Fisica dell' Universita and INFN, Padova, Italy[f]

J.M. Butterworth, J. Bulmahn, G. Feild, B.Y. Oh[28], J. Whitmore[29]
Pennsylvania State University, Dept. of Physics, University Park, PA, USA[o]

U. Contino, G. D'Agostini, M. Guida[30], M. Iori, S.M. Mari, G. Marini, M. Mattioli, A. Nigro
Dipartimento di Fisica, Univ. 'La Sapienza' and INFN, Rome, Italy[f]

J.C. Hart, N.A. McCubbin, K. Prytz, T.P. Shah, T.L. Short
Rutherford Appleton Laboratory, Chilton, Didcot, Oxon, U.K.[m]

E. Barberis, N. Cartiglia, C. Heusch, B. Hubbard, J. Leslie, W. Lockman, K. O'Shaughnessy, H.F. Sadrozinski, A. Seiden, D. Zer-Zion
University of California, Santa Cruz, CA, USA[n]

E. Badura, J. Biltzinger, R.J. Seifert, A.H. Walenta, G. Zech
Fachbereich Physik der Universität-Gesamthochschule Siegen, Federal Republic of Germany[c]

S. Dagan[31], A. Levy
School of Physics,Tel-Aviv University, Tel Aviv, Israel[e]

T. Hasegawa, M. Hazumi, T. Ishii, S. Kasai[32], M. Kuze, Y. Nagasawa, M. Nakao, H. Okuno, K. Tokushuku, T. Watanabe, S. Yamada
Institute for Nuclear Study, University of Tokyo, Tokyo, Japan[g]

M. Chiba, R. Hamatsu, T. Hirose, S. Kitamura, S. Nagayama, Y. Nakamitsu
Tokyo Metropolitan University, Dept. of Physics, Tokyo, Japan[g]

R. Cirio, M. Costa, M.I. Ferrero, L. Lamberti, S. Maselli, C. Peroni, A. Solano, A. Staiano
Universita di Torino, Dipartimento di Fisica Sperimentale and INFN, Torino, Italy[f]

M. Dardo
Facultá di Scienze, University of Torino, Alessandria, and INFN-Sezione di Torino, Torino, Italy[f]

D.C. Bailey, D. Bandyopadhyay, F. Benard, S. Bhadra, M. Brkic, B.D. Burow, F.S. Chlebana, M.B. Crombie, G.F. Hartner, G.M. Levman, J.F. Martin, R.S. Orr, J.D. Prentice, C.R. Sampson, G.G. Stairs, R.J. Teuscher, T.-S. Yoon
University of Toronto, Dept. of Physics, Toronto, Ont., Canada[a]

F.W. Bullock, C.D. Catterall, J.C. Giddings, T.W. Jones, A.M. Khan, J.B. Lane, P.L. Makkar, D. Shaw, J. Shulman

University College London, Physics and Astronomy Dept., London, U.K. [m]

K. Blankenship, J. Kochocki, B. Lu, L.W. Mo

Virginia Polytechnic Inst. and State University, Physics Dept., Blacksburg, VA, USA [o]

K. Charchul a, J. Ciborowski, J. Gajewski, G. Grzelak, M. Kasprzak, M. Krzyzanowski, K. Muchorowski, R.J. Nowak, J.M. Pawlak, A. Stopczynski, T. Tymieniecka, R. Walczak, A.K. Wroblewski, J.A. Zakrzewski, A.F. Zarnecki

Warsaw University, Institute of Experimental Physics, Warsaw, Poland [j]

M. Adamus

Institute for Nuclear Studies, Warsaw, Poland [j]

H. Abramowicz[14], Y. Eisenberg, C. Glasman[33], U. Karshon[31], A. Montag[31], D. Revel, A. Shapira

Weizmann Institute, Nuclear Physics Dept., Rehovot, Israel [d]

C. Foudas, C. Fordham, R.J. Loveless, A. Goussiou, I. Ali, B. Behrens, S. Dasu, D.D. Reeder, W.H. Smith, S. Silverstein

University of Wisconsin, Dept. of Physics, Madison, WI, USA [n]

W.R. Frisken, K.M. Furutani, Y. Iga

York University, Dept. of Physics, North York, Ont., Canada [a]

[1] supported by Worldlab, Lausanne, Switzerland

[2] also at IROE Florence, Italy

[3] now at SAP, Heidelberg

[4] now at TRIUMF, Vancouver

[5] now at Univ. of Bologna

[6] now a self-employed consultant

[7] now at DESY as Alexander von Humboldt Fellow

[8] now at CERN

[9] now at DESY

[10] now at IST GmbH, Darmstadt

[11] on leave from Jagellonian University, Cracow

[12] now at Martin & Associates, Hamburg

[13] now at Harry Hoffmann, Fitzbek

[14] on leave from Warsaw University, Warsaw

[15] now at Lufthansa, Frankfurt

[16] supported by the European Community

[17] now at Integrata, Frankfurt

[18] now at Blohm & Voss, Hamburg

[19] deceased

[20] now at Institute for Cosmic Ray Research, University of Tokyo

[21] on leave of absence at DESY, supported by DGICYT

[22] partially supported by Comunidad Autónoma de Madrid, Spain

[23] supported by Fundación Banco Exterior

[24] now at SSC, Dallas

[25] now at Department of Energy, Washington

[26] now at Centre for Subatomic Research, Univ.of Alberta, Canada and TRIUMF, Vancouver, Canada

[27] now with McKinsey Consultants, Sidney, Australia

[28] on leave and supported by DESY 1992-93

[29] on leave and supported by DESY 1991-92

[30] permanent address Dip. di Fisica, Univ. di Salerno, Italy

[31] supported by the MINERVA Gesellschaft für Forschung GmbH

[32] now at Hiroshima National College of Maritime Technology

[33] supported by the DAAD - Deutscher akademischer Austauschdienst

[a]supported by the Natural Sciences and Engineering Research Council of Canada

[b]supported by the FCAR of Quebec, Canada

[c]supported by the German Federal Ministry for Research and Technology (BMFT)

[d]supported by the MINERVA Gesellschaft für Forschung GmbH, by the Israel Ministry of Energy, and by the Israel Academy of Science

[e]supported by the Israel Ministry of Energy, and by the German Israeli Foundation

[f]supported by the Italian National Institute for Nuclear Physics (INFN)

[g]supported by the Japanese Ministry of Education, Science and Culture (the Monbusho) and its grants for Scientific Research

[h]supported by the Korean Ministry of Education and Korea Science and Engineering Foundation

[i]supported by the Netherlands Foundation for Research on Matter (FOM)

[j]supported by the Polish Government and Ministry of Education Research Programs

[k]supported by the German Federal Ministry for Research and Technology (BMFT), the Volkswagen Foundation, and the Deutsche Forschungsgemeinschaft

[l]supported by the Spanish Ministry of Education and Science through funds provided by CICYT

[m]supported by the UK Science and Engineering Research Council

[n]supported by the US Department of Energy and by the US National Foundation

"supported by the National Science Foundation

Bibliography

[1] P. Ramond, Ann. Rev. Nucl. Part. Sci. 33 (1983) 31.

W.J. Marciano, Ann. Rev. Nucl. Part. Sci. 41 (1991) 469.

G. Altarelli, Ann. Rev. Nucl. Part. Sci. (1989) 357.

[2] F. Halzen, A.D. Martin, "Quarks and Leptons: An Introductory Course in Modern Particle Physics", John Wiley and Sons, Toronto (1984).

[3] G. 't Hooft, Nucl. Phys. B33 (1971) 173.

Ibid., B35 (1971) 167.

G. 't Hooft and M. Veltman, ibid., B44 (1972) 189.

Ch. Llewellyn-Smith, Phys. Lett. B46 (1973) 233.

J. Cornwall, D. Levin, and G. Tiktopoulos, Phys. Rev. Lett. 30 (1973) 1268.

[4] M. Gell-Mann, Phys. Lett. 8 (1964) 214.

G. Zweig, CERN Report No. TH401 (1964).

[5] W.O. Greenberg, Phys. Rev. Lett. 13 (1964) 598.

[6] D. J. Gross, Proc. of the Third International Symposium on the History of Particle Physics, SLAC (1992).

[7] R.W. McAllister and R. Hofstadter, Phys. Rev. 102 (1956) 851.

[8] L. H. Ryder, "Quantum Field Theory", Cambridge University Press, Cambridge (1987).

[9] W.F.K. Panofsky and E. Allton, Phys. Rev. 110 (1958) 1155.

W. Bartel, et al., Phys. Lett. B28 (1968) 148.

[10] E.D. Bloom, et al., Phys. Rev. Lett. 23 (1969) 930.

M. Breidenbach et al., Phys. Rev. Lett. 23 (1969) 935.

[11] J.D. Bjorken, Phys. Rev. 179 (1969) 1547.

[12] J. D. Bjorken and E.A. Paschos, Phys. Rev. 185 (1969) 1975.

R.P. Feynman, "Photon-Hadron Interactions", Addison Wesley, Reading, Mass. (1972).

[13] R.L. Jaffe, Los Alamos School on Relativistic Dynamics and Quark-Nuclear Physics, ed. M.B. Jackson and A. Picklesimer, John Wiley and Sons, New York (1985).

[14] C.G. Callan and D.J. Gross, Phys. Rev. Lett. 22 (1968) 156.

[15] G. Miller et al., Phys. Rev. D5 (1972) 528.

T. Eichten et al., Phys. Lett. B46 (1973) 274.

[16] C.G. Callan and D.J. Gross, Phys. Rev. D8 (1973) 4383.

[17] S. Coleman and D.J. Gross, Phys. Rev. Lett. 31 (1973) 851.

[18] D.J. Gross and F. Wilczek, Phys. Rev. Lett. 30 (1973) 1343.

H.D. Politzer, ibid., 1346.

[19] Anna Hasenfratz and Peter Hasenfratz, Ann. Rev. Nucl. Part. Sci. 35 (1985) 559.

[20] TASSO collab., R. Brandelik et al., Phys. Lett. 86B (1979) 243.

MARK J collab., D.P. Barber et al., Phys. Rev. Lett. 43 (1979) 830.
PLUTO collab., Ch. Berger et al., Phys. Lett. 86B (1979) 418
JADE collab., W. Bartel et al., Phys. Lett. 91B (1980) 142.
[21] G. Altarelli, Phys. Rep. 81C (1982) 1.
[22] J.G.H. de Groot et al., Zeit. Phys. C1 (1979) 143.
[23] G. Altarelli and G. Parisi, Nucl. Phys. B126 (1977) 298.
[24] OPAL collab., M.Z. Akrawy et al., Z. Phys. C47 (1990) 505.
L3 collab., B. Adeva et al., ibid. C55 (1992) 39.
ALEPH collab., D. Buskulic et al., ibid. 209.
W. deBoer and H. Fürstenau, Proc. of MC91 Workshop, NIKHEF (1991) 616.
[25] EMC collab., J.J. Aubert et al., Phys. Lett . B95 (1980) 306.
Ibid., B100 (1981) 433.
Ibid., Phys. Lett. B119 (1982) 233.
[26] E665 collab., M.R. Adams et al., Phys. Rev. Lett. 69 (1992) 1026.
[27] EMC collab., M. Arneodo et al., Z. Phys. C36 (1987) 527.
[28] ZEUS collab., M. Derrick et al., Phys. Lett. B306 (1993) 158.
[29] D. Graudenz and N. Magnussen, Proc. of Physics at HERA, vol. 1, DESY (1992) 261.
[30] R. Peccei and R. Rückl, Nucl. Phys. B162 (1980) 125.
[31] G. Ingelman, Proc. of Workshop on Physics at HERA, vol. 3, DESY (1992) 1366.
[32] N. Magnussen et al., Proc. of Workshop on Physics at HERA, vol. 3, DESY (1992) 1167.
[33] M. Bengtsson and T. Sjöstrand, Z. Phys. C37 (1988) 465.
[34] Yu. L. Dokshitzer, D.I. Dyakanov, and S.I. Troyan, Phys. Rep. 58 (1980) 270.
[35] T. Sjöstrand, Phys. Lett. B157 (1985) 321.
M. Bengtsson, T. Sjöstrand, M. van Zijl, Z. Phys. C32 (1986) 67.
[36] M. Bengtsson and T. Sjöstrand, Phys. Lett. 185B (1987) 435.
Ibid., Nucl. Phys. B289 (1987) 810.
[37] A.H. Mueller, Phys. Lett. 104B (1981) 161.
A. Bassetto, M. Ciafaloni, G. Marchesini, Phys. Rep. 100 (1983) 201.
[38] M. Bengtsson, G. Ingelman, and T. Sjöstrand, Nucl. Phys. B301 (1988) 554.
[39] G. Marchesini et al., Comp. Phys. Comm. 67 (1992) 465.
[40] M. Ciafaloni, Nucl. Phys. B296 (1988) 49.
[41] G. Marchesini, B.R. Webber, Nucl. Phys. B310 (1988) 461.
[42] G. Marchesini and B.R. Webber, Nucl. Phys. B238 (1984) 1.
[43] T. Sjöstrand, Comp. Phys. Comm. 39 (1986) 347.
Ibid., 43 (1987) 367.
[44] G. Gustafson, U. Pettersson, Nucl. Phys. B306 (1988) 746.
[45] Ya.I. Azimov, Yu.L. Dokshitzer, V.A. Khoze, and S.I. Troyan, Phys. Lett. B165 (1985) 147.

Yu. L. Dokshitzer, V.A. Khoze, A.H. Mueller, and S.I. Troyan, "Basics of Perturbative QCD", Editions Frontières, Paris (1991).
[46] G. Gustafson, Phys. Lett. B175 (1986)453.
[47] U. Pettersson, Lund preprint, LUTP 88-5 (1988).
[48] B. Andersson, G. Gustafson, L. Lönnblad, U. Petterson, Z. Phys. C43 (1989) 625.
[49] L. Lönnblad, Lund preprint, LUTP 89-10 (1989).
L. Lönnblad, Comp. Phys. Comm. 71 (1992) 15.
[50] T. Sjöstrand, Proc. of the Cargèse Summer Institute on Z^0 Physics, Cargèse, 1990.
[51] B. Andersson, G. Gustafson, G. Ingelman, T. Sjöstrand, Phys. Rep. 97 (1983) 33.
[52] T. Sjöstrand, Comp. Phys. Comm. 39 (1986) 347.
[53] B.R. Webber, Nucl. Phys. B238 (1984) 492.
[54] G. Marchesini, L. Trentadue, and G. Veneziano, Nucl. Phys. B181 (1981) 335.
[55] A. Kwiatkowski, H. Spiesberger, and H.-J. Möhring, Proc. of Workshop on Physics at HERA, vol. 3, DESY (1992) 1294.
[56] G. Schuler and H. Spiesberger, Proc. of Workshop on Physics at HERA, vol. 3, DESY (1992) 1419.
[57] B. Anderson et al., Z. Phys. C13 (1982) 361.
[58] UA5 collab., G.J. Alner et al., Nucl. Phys. B291 (1987) 445.
[59] "HERA, A Proposal for a Large Electron-Proton Colliding Beam Facility at DESY", DESY-HERA 81-10, 1981.
[60] Proc. of XVth International Conference on High Energy Accelerators, Hamburg (July, 1992).
Proc. of 1991 IEEE Particle Accelerator Conference, San Francisco, (May, 1991).
[61] ZEUS collab., "The ZEUS Detector - Status Report 1993", Ed. Uwe Holm, DESY, Hamburg, 1993.
ZEUS collab., "The ZEUS Detector Technical Proposal", DESY, Hamburg, 1986.
[62] P. Bruni et al. , "The Magnetic Field of the ZEUS Detector", ZEUS Note 91-127.
[63] F. Corriveau, Nucl. Instr. Meth. A326 (1993) 470.
[64] "The TOSCA Reference Manual", Vector Fields Limited, 24 Bankside, Kidlington, Oxford, OX5 1JE, England.
[65] Richard C. Fernow, "Introduction to Experimental Particle Physics", Cambridge University Press, New York (1986).
[66] W.R. Leo, "Techniques for Nuclear and Particle Physics Experiments", Springer-Verlag, Berlin (1987).
[67] Review of Particle Properties, Phys. Rev. D45 (1992).
[68] Review of Particle Properties, Phys. Rev. D (1980).
[69] C. Alvisi et al., Nucl. Instr. Meth. A305 (1991) 30.

[70] C.B. Brooks et al., Nucl. Instr. Meth. A283 (1989) 477.
[71] G. Blair et al., ZEUS-Note 92-122, Jan. 12, 1993.
[72] Richard Wigmans, Ann. Rev. Nucl. Part. Sci. 41 (1991) 133.
[73] Richard Wigmans, Nucl. Instr. Meth. A259 (1987) 389.
[74] C. Fabjan, "Experimental Techniques in High Energy Physics", ed. T. Ferbel, Addison-Wesley, Don Mills (1987).
[75] T.A. Gabriel, Nucl. Instr. Meth. A150 (1978) 145.
T.A Gabriel, Proc. Workshop on Compensated Calorimetry, Pasedena (1985).
[76] H. Abramowicz, et al., Nucl. Instr. Meth. A180 (1981) 429.
[77] G. d'Agostini et al., Nucl. Instr. Meth. A274 (1989) 134.
[78] U. Behrens et al., Nucl. Instr. Meth. A289 (1990) 115.
[79] J. Krüger, Habilitationsschrift, DESY F35-92-02 (1992).
[80] T. Akesson et al., Nucl. Instr. Meth. A241 (1985) 17.
[81] T. Kamon et al., Nucl. Instr. Meth. A213 (1983) 261.
[82] A. Andresen et al., Nucl. Instr. Meth. A309 (1991) 101.
A. Bernstein et al., to be submitted to Nucl. Instr. Meth.
[83] U. Behrens et al., "Calibration of the Forward and Rear ZEUS Calorimeter using Cosmic Ray Muons", DESY 93-121, to be published in Nucl. Instr. Meth. (1993).
[84] ZEUS collab., ZEUS-Note 91-044 (1991).
ZEUS collab., ZEUS-Note 91-042 (1991).
[85] H. Abramowicz et al., Nucl. Instr. Meth. A313 (1992) 126.
[86] G. Abbiendi et al., Nucl. Instr. Meth. A333 (1993) 342.
[87] G. Wolf, "First Results from HERA", DESY 92-190 (1992).
[88] H. Uijterwaal, Ph.D. thesis, Universiteit van Amsterdam, Amsterdam (1992).
[89] U. Behrens, L. Hagge, W.O. Vogel, Nucl. Instr. Meth. A332 (1993) 253.
[90] S.M. Fisher and P. Palazzi, "The ADAMO Data System", Programmer's Manual Version 3.2, RAL-preprint, 1992.
[91] I.H. Park, Proc. of the Real-Time 93 Conference, Vancouver, (1993).
[92] D.G. Cussans et al., Nucl. Instr. Meth. A315 (1992) 397.
N. Harnew et al., Nucl. Instr. Meth. A279 (1989) 290.
[93] A. Caldwell et al., Nucl. Instr. Meth. A321 (1992) 356.
[94] L. Hervás, "The Pipelined Readout for the ZEUS Calorimeter", Ph.D. thesis, Universidad Autónoma de Madrid, 1990.
[95] R. Brun et al., CERN DD/EE/84-1.
[96] G. Hartner, ZEUS note 88-049 (1988).
[97] Proc. of 14^{th} Workshop of the INFN Eloisatron Project on Data Structures of Particle Physics Experiments, Erice (Nov. 1990).

E. Tscheslog, ZEUS-Note 91-37 (1991).
R. Glaeser, ZEUS-Note 91-103, (1991).
[98] P. de Jong, Ph.D. thesis, Universiteit van Amsterdam, Amsterdam (1993).
P. de Jong, ZEUS-Note 92-019 (1992).
[99] P. Billoir and S. Qian, Nucl. Instr. Meth. A311 (1992) 139.
[100] D. Bailey et al., Proc. of the Conference on Computing in High Energy Physics, Annecy (1992).
[101] ANSI/IEEE, The VMEbus Specification Revision C, ANSI/IEEE Std. 1014 or IEC 821 (1985).
[102] H. Boterenbrood, et al., "A Two-Transputer VME-Module for Data Acquisition and Online Event Selection in ZEUS", to be published in Nucl. Inst. Meth. (1993).
H. Boterenbrood, et al. to be submitted to Nucl. Instr. Meth.
[103] ACP Group, "Branch Bus Specification", Fermilab (1987).
T. Nash, Comp. Phys. Comm. 57 (1989) 47.
[104] ACP Group, "VBBC Manual", Fermilab (1988).
[105] ACP Group, "BVI Manual", Fermilab (1987).
[106] ACP Group, "Bus Switch Manual", Fermilab (1988).
[107] Gerry Kane, "MIPS RISC Architecture", Prentice Hall, Toronto (1989).
[108] Douglas Comer, "Internetworking with TCP/IP: Principles, Protocols, and Architecture", Prentice Hall International, London (1988).
[109] Tom DeMarco, "Structured Analysis and System Specification", Prentice Hall, Toronto (1979).
Edward Yourdon and Larry L. Constantine, "Structured Design", Prentice Hall, Toronto (1979).
Stephen J. Mellor and Paul T. Ward, "Structured Development for Real-Time Systems", Yourdon Press, New Jersey (1986).
[110] TEAMWORK, CADRE Technologies Inc., Providence, R.I., U.S.A.
[111] ACP Group, "Co-operative Processes User's Manual", Fermilab (1989).
[112] ZEUS collab., "The ZEUS Detector - Status Report 1989", Ed. Eduardo Ros, DESY, 1989.
[113] S. Bhadra, M. Crombie, D. Kirkby, R.S. Orr, Comp. Phys. Comm. 57 (1989) 321.
[114] J. Feltesse, Proc. of the HERA Workshop, vol.1, DESY (1987) 33.
[115] F. Jacquet and A. Blondel, Proc. of the study of an ep facility for Europe, Ed. U. Amaldi, DESY 79/48 (1979) 391.
[116] S. Bentvelsen, Jos Engelen, and Paul Kooijman, Proc. of the Workshop on Physics at HERA, vol. 1, DESY (1992) 23.
[117] K. Goulianos, Phys. Rep. 101 (1983) 169.
[118] ZEUS collab., M. Derrick et al., Phys. Lett. B316 (1993) 412.
[119] ZEUS collab., M. Derrick et al., Phys. Rev. Lett. B303 (1993) 183.

[120] A.D. Martin, R.G. Roberts, and W.J. Sterling, Phys. Rev. D47 (1993) 867.
[121] ZEUS collab., M. Derrick et al., Phys. Lett. B315 (1993) 481.
[122] A. Donnachie and P.V. Landshoff, Phys. Lett. B191 (1987) 309.
[123] J. Morfin and W.K. Tung, Z. Phys. C52 (1991) 13.
[124] N. Brook, private communication.
[125] H.-U Bengtsson and T. Sjöstrand, Comp. Phys. Comm. 46 (1987) 43.
T. Sjöstrand, Proc. of the Workshop on Physics at HERA, vol. 3, DESY (1992) 1405.
[126] H1 collab., T. Ahmed et al., Phys. Lett. B298 (1993) 469.
[127] G. Ingelman, private communication.